CONSTRUCTION OF TERAHERTZ SPECTROMETERS AND THEIR USE IN CHARACTERIZATION OF CONDUCTIVITIES AND MODULATION BEHAVIORS OF GRAPHENE LAYERS

A THESIS SUBMITTED TO
THE GRADUATE SCHOOL OF NATURAL AND APPLIED SCIENCES
OF
MIDDLE EAST TECHNICAL UNIVERSITY

BY

EMİNE KAYA

IN PARTIAL FULFILLMENT OF THE REQUIREMENTS
FOR
THE DEGREE OF DOCTOR OF PHILOSOPHY
IN
CHEMISTRY

SEPTEMBER 2017

Approval of the thesis:

CONSTRUCTION OF TERAHERTZ SPECTROMETERS AND THEIR USE IN CHARACTERIZATION OF CONDUCTIVITIES AND MODULATION BEHAVIORS OF GRAPHENE LAYERS

submitted by **EMİNE KAYA** in partial fulfillment of the requirements for the degree of **Doctor of Philosophy in Chemistry Department, Middle East Technical University** by,

Prof. Dr. Gülbin Dural Ünver
Dean, Graduate School of **Natural and Applied Sciences** _____

Prof. Dr. Cihangir Tanyeli
Head of Department, **Chemistry** _____

Assoc. Prof. Dr. Okan Esentürk
Supervisor, **Chemistry Dept., METU** _____

Examining Committee Members:

Prof. Dr. Halime Gül Yağlıoğlu
Physics Engineering Dept., Ankara University _____

Assoc. Prof. Dr. Okan Esentürk
Chemistry Dept., METU _____

Prof. Dr. Hakan Altan
Physics Dept., METU _____

Prof. Dr. Ali Çırpan
Chemistry Dept., METU _____

Asst. Prof. Dr. Bülend Ortaç
UNAM., Bilkent University _____

Date: 08.09.2017

I hereby declare that all information in this document has been obtained and presented in accordance with academic rules and ethical conduct. I also declare that, as required by these rules and conduct, I have fully cited and referenced all material and results that are not original to this work.

Name, Last Name: EMİNE KAYA

Signature :

ABSTRACT

CONSTRUCTION OF TERAHERTZ SPECTROMETERS AND THEIR USE IN CHARACTERIZATION OF CONDUCTIVITIES AND MODULATION BEHAVIORS OF GRAPHENE LAYERS

Kaya, Emine
PhD., Department of Chemistry
Supervisor: Assoc. Prof. Dr. Okan Esentürk

September 2017, 156 pages

Aim of this thesis was to construct two new terahertz spectrometers, THz Time Domain Spectroscopy (THz-TDS) and Time Resolved THz Spectroscopy (TRTS) for characterization of the static and dynamic properties of novel materials. After successful construction and signal optimization, system characterizations of both systems were completed with well-known samples. Possible use of ionic liquid doped graphene devices on PVC and PE substrates were characterized by THz-TDS. Devices operated at low voltages and provided nearly 100 % modulation between 0.2 THz and 1.5 THz at ca. 3.5 V. High modulation depth over such a broad spectrum and simple device structure make these modulators promising candidates in THz and related technologies. THz sheet conductivities of large-area CVD grown graphene samples were extracted with THz-TDS measurements. Comparison of results with literature showed that THz-TDS is a noncontact and reliable technique that allows characterization of frequency dependent sheet conductivity of graphene. Carrier relaxation dynamics of graphene samples were investigated with TRTS. A decrease in photo induced conductivity is observed with single layer graphene sample with 800 nm excitation due to its highly doped nature. Thickness dependent THz dynamics of multi layer graphene samples with 800 nm showed that samples had similar initial

responses which can be explained as hot carrier cooling via carrier-carrier scattering and carrier-phonon scattering. Existence of interlayer charge transfers were suggested with observation of slower decay times of thicker samples due to slower recombinations. 400 nm pump studies of samples resulted in comparably shorter decay times due to initial hot carrier cooling and fast recombination rates of charges stemming from existence of easier interlayer transfer of charges.

Keywords: Terahertz radiation, Terahertz spectrometers, Terahertz modulator application, Graphene

ÖZ

TERAHERTZ SPEKTROMETRE KURULUMU VE GRAPHENE TABAKALARININ İLETKENLİK VE MODÜLASYON DAVRANIŞLARININ KARAKTERİZASYONU

Kaya, Emine
Doktora, Kimya Bölümü
Tez Yöneticisi: Doç. Dr. Okan Esentürk

Eylül 2017, 156 sayfa

Bu tezin amacı iki yeni THz spektrometre, THz-TDS and TRTS, kurulumu ile orjinal malzemelerin statik ve dinamik karakterizasyonunu gerçekleştirmektir. Sistemlerin kurulumu ve sinyal optimizasyon aşaması başarı ile gerçekleştirildikten sonra, iyi bilinen malzemeler ile system karakterizasyonları yapılmıştır. PVC ve PE üzerine transfer edilen ve iyonik sıvı ile katkılandırılan farklı kalınlıklara sahip çok katmanlı grafen cihazlar ile THz modulatör çalışmaları yapılmıştır. Çok tabakalı grafen kapasitörler ile 0.2 - 1.5 THz bant aralığında, 3.5 V voltaj uygulandığında yaklaşık olarak % 100 modülasyon sağlamıştır. Geniş bir spektrumda yüksek modülasyon miktarı, basit cihaz yapısı ve uygulanan düşük voltajlar bu modülatörleri THz ve benzer teknolojiler için umut vadeden adaylar yapmaktadır. THz-TDS ölçümleri ile geniş alanlı CVD yöntemi ile büyütülmüş grafen örneklerin tabaka THz iletkenlik karakterizasyonları yapılmıştır. Sonuçlar literatür ile kıyaslandığında THz-TDS sisteminin grafenin frekansa bağlı tabaka iletkenliğinin hesaplanabilmesini sağlayan temazsız ölçüm yapılabilen ve güvenilir bir teknik olduğu görülmüştür. TRTS kullanılarak grafen örneklerinin THz dinamikleri araştırılmıştır. Tek tabakalı grafen örneği 800 nm pompanın etkisi ile, yüksek katkılı doğası nedeniyle, azalan iletkenlik davranışı göstermiştir. 800 nm pompa sonrası kalınlığa bağlı dinamik davranışlar

incelenerek, ilk zamanlardaki davranış benzerliği yük-yük ve yük phonon etkileşimi ile açıklanmıştır. Kalın örneklerde gözlemlenen daha yavaş bozunma zamanları, katmanlar arası yük transferinin varlığını ve bunun sonucu olarak yüklerin birleşmesinin daha uzun sürdüğünü göstermektedir. 400 nm pump sonuçları yüksek enerjili yüklerin çok daha kolay tabakalar arası geçiş yapmasına bağlı olarak daha hızlı soğumaları ve birleşmeleri nedeniyle daha kısa bozunma zamanları göstermektedir.

Anahtar kelimeler: Terahertz, Terahertz spektrometreleri, Terahertz uygulamaları, Grafen

To My Family

ACKNOWLEDGMENTS

I would like to express my sincere gratitude to my supervisor Assoc. Prof. Dr. Okan Esentürk for his guidance, support, encouragement, patience, advice and criticism throughout this study.

I would like to thank to Prof. Dr. Hakan Altan for his help in the construction of our systems and his valuable suggestions.

I would like to thank to Asst. Prof. Dr. Bülend Ortaç for welcoming us to the femtosecond laboratory of UNAM and his kind support.

I would like to thank to Assoc. Prof. Dr. Coşkun Kocabaş for providing samples.

I would like to express my gratitude to my thesis examination committee members Prof. Dr. Gül Yağlıoğlu and Prof. Dr. Ali Çırpan.

I would like to thank to Enis Arık for his experimental helps beside his friendships.

I would like thank to all former and present Laser Spectroscopy Research Group members for their cooperation and their friendships.

I would like to acknowledge TUBITAK (111T393) and METU-BAP for the financial support.

I would like to thank to my dear friend Gönül Hızalan Özsoy for her invaluable friendship and support during my thesis writing process.

Words fail to express my eternal gratitude to my family for believing in me and giving me endless support.

TABLE OF CONTENTS

ABSTRACT v
ÖZ vii
ACKNOWLEDGMENTS x
TABLE OF CONTENTS xii
LIST OF TABLES xv
LIST OF FIGURES xvi
LIST OF ABBREVIATIONS xxii

CHAPTERS

1. INTRODUCTION 1

1.1 THz Light 1
1.2 THz Generation Techniques 2
1.3 THz Detection Techniques 4
1.4 THz Spectroscopy Systems 6
1.4.1 Terahertz Time Domain Spectroscopy 6
1.4.2 Time Resolved Terahertz Spectroscopy 8
1.5 THz Applications 9
1.6 Aim and Organization of this Thesis 10

2. CONSTRUCTION OF THz SPECTROMETERS 13

2.1 Laser System 13
2.2 THz-TDS Set-Ups 16
2.2.1 Data Collection and Analysis 23
2.2.2 Determination of Optical Constants 27
2.2.3 System Characterization 28
2.3 TRTS 29
2.3.1 Data Collection and Analysis 34
2.3.2 System Characterization 37

2.4 Signal Optimization 39
2.5 Conclusion 45

3. GRAPHENE THz MODULATORS 47

3.1 Introduction 47
3.1.1 Band Structure and Electronic Properties of Graphene 48
3.1.2 Graphene Applications 50
3.1.3 Introduction to Graphene THz Modulators 51
3.2 Experimental 52
3.2.1 Sample Preparation and Characterization 53
3.2.2 Device Fabrication 54
3.2.3 THz Measurements of SLG Modulators 56
3.2.4 THz Measurements of MLG Modulators 57
3.3 Results and Discussion 58
3.4 Conclusion 69

4. TERAHERTZ CONDUCTIVITY MEASUREMENTS OF SLG AND MLG 71

4.1 Introduction 71
4.2 Models for THz Conductivity 72
4.2.1 Drude Model 73
4.2.2 Drude-Smith Model 74
4.3 Sample Preparation 76
4.4 THz Measurements of SLG and MLG Samples 76
4.5 Complex Refractive Indices of Reference Substrates 78
4.6 Complex Conductivity of CVD SLG on Quartz and PVC 79
4.7 Complex Conductivity of CVD MLG on Quartz 86
4.8 Conclusion 90

5. TERAHERTZ CHARGE CARRIER DYNAMICS OF CVD GROWN SLG AND MLG 93

5.1 Introduction 93
5.1.1 Literature of SLG THz Dynamics 95

5.1.2 Literature of MLG THz Dynamics 98
5.2 Sample Preparation 101
5.3 Time Resolved THz Spectroscopy Measurements 102
5.4 THz Dynamics of SLG 103
5.5 THz Dynamics of MLG 109
5.5.1 THz Dynamics of MLG with 800 nm Optical Pump 110
5.5.2 THz Dynamics of MLG with 400 nm Optical Pump 117
5.5.3 Comparison of 800 nm and 400 nm Pump-THz Probe Dynamics 119
5.6 THz dynamics of MLG samples on PE and PVC Substrates 121
5.7 Conclusion 128

6. CONCLUSION 131

REFERENCES 135

VITA 153

LIST OF TABLES

TABLES

Table 2. 1. Summary of the specifications of the laser system. 16
Table 2. 2. Components of TRTS system. 31
Table 3. 1. Comparison of THz-TDS and Four Probe experimental results. 64
Table 3. 2. Effect of doping on conductivity. 67
Table 4. 1. Derived transport properties of SLG on quartz. 81
Table 4. 2. Derived transport properties of SLG on PVC. 84
Table 4. 3. Derived DS and Drude scattering rates $\boldsymbol{\Gamma}$ of MLG samples. 89
Table 5. 1. % Conductivity difference between 27 and 100 layers of graphene at specific delay times. 117
Table 5. 2. Extracted decay times of the pump-induced THz response by fitting with single exponential function. 121
Table 5. 3. Extracted decay times of the pump-induced THz response by fitting with single exponential decay function. 123
Table 5. 4. Time dependent conductivity comparison of 800 and 400 nm optical pump studies for PE MLG 32. 124
Table 5. 5. Extracted decay times of the pump-induced THz response by fitting with single exponential decay function. 126
Table 5. 6. Time dependent conductivity comparison of 800 and 400 nm optical pump studies for PVC MLG 30. 127

LIST OF FIGURES

FIGURES

Figure 1.1. Terahertz region of electromagnetic spectrum. 1
Figure 1.2. PCA for generation of ultrashort THz pulses. 3
Figure 1.3. Principle of electro-optic sampling.[17] 5
Figure 2.1. Tsunami femtosecond laser. 14
Figure 2.2. The Spitfire laser amplifier. 15
Figure 2.3. Components of the Spitfire laser amplifier. 15
Figure 2.4. THz-TDS system with PCA. 17
Figure 2.5. BATOP Antenna Design. 18
Figure 2.6. THz signal in time domain (left) and its corresponding bandwidth in frequency domain (right). 20
Figure 2.7. THz-TDS set-up with PCA. 21
Figure 2.8. THz-TDS set-up with ZnTe crystal. 22
Figure 2.9. ZnTe crystal and optical chopper. 23
Figure 2.10. Front panel of Labview Software. 24
Figure 2.11. Extraction of THz time domain profile. 25
Figure 2.12. The THz pulse shape in time-domain. 25
Figure 2.13. (a) Absorption coefficient, (b) Refractive index of benzene from THz-TDS measurements. 29
Figure 2.14. TRTS set-up. 30
Figure 2.15. Timing relation between THz probe, sampling and optical pump pulse. 34
Figure 2.16. Time evolution of the relative change in transmission of THz peak value. 35
Figure 2.17. The differential transmission $-\Delta T/T_0$ of the peak THz field as a function of the 800 nm optical pump/ THz probe delay time, for 16 and 52 $\mu J/cm^2$, inset shows the decay behavior of long lived carriers. 39
Figure 2.18. TRTS system enclosed with a plexiglass box. 40

Figure 2.19. Improvement in the SNR of measured THz time domain profile with decreased humidity level. 40
Figure 2.20. Comparison of large area balanced photodetectors, New Focus-2307 and Thorlabs-PDB210A/M. 41
Figure 2.21. (a) Time domain, (b) Frequency domain comparison of Mylar and TPX as beam combiner. 42
Figure 2.22. The time domain data collected with a modulation setting of 250 and 500 Hz. 43
Figure 2.23. THz bandwidth of ZnTe crystal (a) 1 mm, (b) 0.5 mm. 44
Figure 2.24. Change in (a) THz profile (b) Bandwidth, with compressor settings. 45
Figure 3.1. Graphene forms the basis of all graphitic materials: fullerenes, nanotubes and bulk graphite.[60] 47
Figure 3.2. The band structures and energy gaps of insulator, semiconductor, metal and graphene. The claret red colors indicate the Fermi levels in different materials. 49
Figure 3.3. (a) Optical transmittance spectra of the MLG electrodes at different temperatures, (b) Variation of the sheet resistance (blue curve) and optical absorption (red curve) of MLG electrodes with the layer number.[106] 53
Figure 3.4. (a) Transfer printing of large area multilayer graphene on flexible PVC substrates by lamination process. Multilayer graphene electrodes were synthesized on metal foils (copper or nickel), then 75 mm thick PVC film was laminated on graphene coated side, (b) Etching the metal foils yields flexible multilayer graphene electrodes on the PVC support.[106] 54
Figure 3.5. (a) A schematic of the SLG or MLG structure consisting of graphene, electrolyte medium, and gold electrode. Drawings showing (b) No doping case at zero applied voltage and (c) Intercalation of ions through the graphene layers by gating. 55
Figure 3.6 (a) SLG Modulator, (b) Position of sample in the THz-TDS System. 56
Figure 3.7. Voltage dependent THz time domain profiles of SLG. 57
Figure 3.8. Voltage dependent THz time domain profiles for (a) MLG850, (b) MLG900, (c) MLG1000 and (d) MLG1000PE. 58
Figure 3.9. (a) Voltage dependent THz field near peak amplitude of SLG. (Inset: Example of time domain THz profile), (b) Corresponding frequency domain

amplitudes, (c)THz transmittance of SLG Modulator at all applied voltages, d) Modulation with voltage at THz peak amplitude. 59
Figure 3.10. (a) Voltage dependent THz field near peak amplitude of MLG850. (Inset: Example of time domain THz profile) (b) Corresponding frequency domain amplitudes. 60
Figure 3.11. Frequency domain amplitudes from 0.2 THz to 1.5 THz frequency range for (a) MLG900, (b) MLG1000, (c) MLG1000PE 61
Figure 3.12. THz transmittance of (a) MLG850, (b) MLG900, (c) MLG1000 and (d) MLG1000PE at all applied voltages relative to 0 V. 62
Figure 3.13. (a) Modulation with voltage at THz peak amplitude (MLG850 black square; MLG900 red circle; MLG1000 green triangle; MLG1000PE blue pentagon). (Inset: Voltage dependent sheet resistance of MLG850 measured by four probe. ... 63
Figure 3.14. Transmittance of MLG850 device at all applied voltages relative to 0 V for three selected frequencies of 0.4, 0.9 and 1.4 THz. 63
Figure 3.15. THz sheet conductivity of devices at all applied voltages. (a) MLG850, (b) MLG900, (c) MLG1000 (d) MLG1000PE 66
Figure 3.16. THz sheet conductivities of MLG devices at 0.8 THz for selected voltages of 1.5 V, 2.8 V, and 3.4 V. 66
Figure 3.17. Insertion loss of PVC, PE, and the MLG devices grown at 850°C, 900°C and 1000°C 68
Figure 3.18. Modulation vs insertion loss of MLG devices at 0.8 THz for selected voltages of 1.5 V, 2.8 V, and 3.4 V. 68
Figure 4.1. Iris sample holder. 76
Figure 4.2. Measured THz electric-field waveforms of (a) air, quartz substrate and the substrate with SLG, (b) air, PVC substrate and the substrate with SLG. 77
Figure 4.3. Measured THz electric-field waveforms of quartz substrate and the substrate with different MLG samples 78
Figure 4.4. Complex refractive index $n_{sub}(\omega)$ of (a) quartz, (b) PVC. 79
Figure 4.5. (a) Measured average THz electric-field waveforms transmitted through the quartz substrate and the substrate covered with SLG. (b) The amplitudes of Fourier transforms of the corresponding time-domain signals. 79

Figure 4.6. (a) Complex sheet conductivity of the graphene layer, extracted from the relative transmission. The conductivity spectra are normalized by the quantum of conductance $G_0=2e^2/h$, (b) A fit of the real conductivity to Drude model.....81
Figure 4.7. (a) Measured average THz electric-field waveforms transmitted through the PVC substrate and the substrate covered with a SLG. (b) The amplitudes of Fourier transforms of the corresponding time-domain signals. 83
Figure 4.8. (a) Complex sheet conductivity of the graphene layer, extracted from the relative transmission. The conductivity spectra are normalized by the quantum of conductance $G_0=2e^2/h$, (b) A fit of the real conductivity to DS model.....84
Figure 4.9. (a) Change in average THz profile based on layer thickness, (b) THz electric field amplitude in the frequency domain by FFT. 86
Figure 4.10. %THz transmittance change with layer number at peak point of THz signal at 1THz. 87
Figure 4.11. (a) Frequency dependent conductivity behavior of SLG and MLG samples, (b) Conductivity values of samples at 1 THz. 87
Figure 4.12. (a) Drude-Smith, and (b) Drude Model fits of frequency dependent conductivity. 88
Figure 5.1. Measured THz time domain pulses transmitted through the SLG sample without (blue, stars) and with (orange, circles) the presence of optical pump pulse preceding the peak of the terahertz pulse by ~3.5 ps. 104
Figure 5.2. Variation in the differential THz signal at pump arrival time. 105
Figure 5.3. (a) Measured differential THz probe transmission $\Delta T/T$ as a function of the probe delay for SLG is given at seven different applied fluencies of optical pump pulse. (b) Maxima of the $\Delta T/T_0$ from part (a) as a function of applied fluence. 106
Figure 5.4. (a) Experimental differential THz transmission, $\Delta T/T_0$, as a function of pump – probe delay recorded at a fluence of 400 $\mu J/cm^2$. (b) Evolution of the real part of photo induced THz conductivity as function of delay time between the 800 nm pump and the THz probe. 107
Figure 5.5. Decay times of the pump-induced THz response, extracted from Figure 5.3. (a) by fitting with single exponential function. 108
Figure 5.6. Measured THz time domain pulses transmitted through the 27-MLG sample without (blue, stars) and with (orange, circles) the presence of optical pump pulse preceding the peak of the terahertz pulse by ~3.5 ps. 110

Figure 5.7. (a) Measured differential THz probe transmission -ΔT/T as a function of the pump probe delay time for 27-MLG is given at seven different applied fluencies of 800 nm optical pump pulse, (b) Maxima of the $\Delta T/T_0$ from part (a) as a function of applied fluence shown on log scale (c) The same data as in (b) shown on a linear scale. 111
Figure 5.8. Decay times of the pump-induced THz response, extracted from Figure 5.7. (a) by fitting with single exponential function..... 112
Figure 5.9. (a) The differential transmission $-\Delta T/T_0$ of the peak THz field as a function of the pump/probe delay time for various thicknesses at a fluence of 410 $\mu J/cm^2$ (b) Normalized version of part (a)..... 113
Figure 5.10. (a) Maxima of the time traces of $\Delta T/T_0$ from Fig. 5.9. (a) as a function of layer thickness, (d) Decay times of the pump-induced THz response, extracted from Fig. 5.9. (a) by fitting with single exponential function. 114
Figure 5.11. (a) Long scan results for MLG-27 and MLG -100 (b) Normalized version of part (a). 115
Figure 5.12. (a) Evolution of the real part of photoinduced THz conductivity as a function of delay time between the 800 nm pump and the THz probe, (b) Time dependent change in $\Delta\sigma$ with layer number. 116
Figure 5.13. (a) The differential transmission $-\Delta T/T_0$ of the peak THz field as a function of the pump/probe delay time, for various thicknesses, (b) Normalized version of part (a), (c) Maxima of the time traces of $\Delta T/T_0$ from part (a) as a function of layer thickness, (d) Decay times of the pump-induced THz response, extracted from part (a) by fitting with single exponential function..... 118
Figure 5.14. (a) Comparison of the differential transmission $-\Delta T/T_0$ of the peak THz field as a function of the 400 nm and 800 nm pump/probe delay time, for 27 layer MLG, (b) Normalized version of part (a). 120
Figure 5.15. (a) The differential transmission $-\Delta T/T_0$ of the peak THz field as a function of the 800 nm optical pump/probe delay time, for 100 and 400 $\mu J/cm^2$, (b) Normalized version of part (a), (c) Comparison of the photon number normalized differential transmission $-\Delta T/T_0$ of the peak THz field as a function of the 400 nm and 800 nm pump/probe delay time for PE MLG-32, (d) Evolution of the real part of photo

induced THz conductivities as function of delay time between 800 nm pump -THz probe and 400 nm pump -THz probe. 122
Figure 5.16. (a) Comparison of the photon number normalized differential transmission $-\Delta T/T_0$ of the peak THz field as a function of the 400 nm and 800 nm pump/probe delay time for PVC MLG-30, (b) Normalized version of part (a).....125
Figure 5.17. Evolution of the real part of photo induced THz conductivities as function of delay time between 800 nm pump -THz probe and 400 nm pump -THz probe.....127

LIST OF ABBREVIATIONS

THz	Terahertz
THz-TDS	THz Time Domain Spectroscopy
TRTS	Time Resolved Terahertz Spectroscopy
Ti:Sa	Titanium Sapphire
ps	Picosecond
fs	Femtosecond
PCA	Photoconductive Antenna
OR	Optical Rectification
ZnTe	Zinc Telluride
GaAs	Gallium Arsenide
EO	Electro Optic
EOS	Electro Optic Sampling
CB	Conduction Band
VB	Valence Band
Si	Silicon
SiC	Silicon Carbide
SNR	Signal-to-noise ratio
SLG	Single Layer Graphene
MLG	Multi Layer Graphene
CVD	Chemical Vapor Deposition

CHAPTER 1

INTRODUCTION

1.1 THz Light

Terahertz (THz) region (0.1 THz to 10 THz) is placed between IR and microwave region of electromagnetic spectrum (Fig. 1.1). 1 THz equals to 1 ps, and 33.3 cm^{-1} (wavenumbers), and 0.004 eV photon energy, and 300 µm wavelength and 47 K in temperature. Until three decades ago, this region has been recognized as THz gap due to lack of proper sources and detection equipment that could access this specific frequency range both at the photonics (high-frequency) and electronics (low frequency) side of the spectrum.[1]

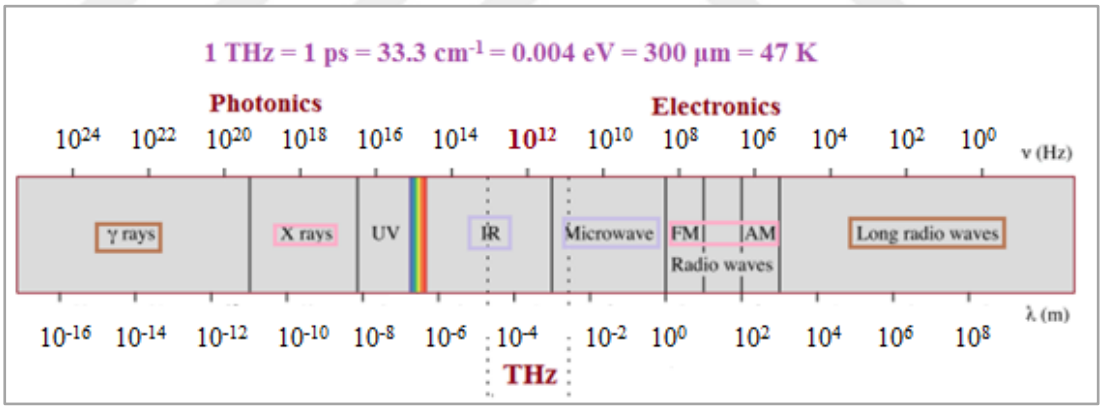

Figure 1.1. Terahertz region of electromagnetic spectrum.

Nature of THz light has not allowed for development of THz sources and detectors that are taken for granted in visible and near IR part of the spectrum. Due to low energy of THz waves, commonly used light sources such as lasers cannot be employed since they require electronic transition of atoms or molecules. Moreover,

high frequency of THz light makes it difficult for scaling electronics to produce sources and detector that can facilitate extremely short carrier life time and simultaneously high-carrier mobility. Even so, with advancement in stable, sub-picosecond pulse duration and high energy laser sources, THz region has become more reachable and THz research has expanded rapidly.

1.2 THz Generation Techniques

THz region, especially 0.1 THz and 2 THz band is difficult to generate by means of conventional electronic and optical methods. While lower frequencies of less than 0.5 THz, microwave region of electromagnetic spectrum, can be produced by the fast transport of electrons in semiconductors, frequencies above 1 THz can only be generated by direct conversion of electrical power to optical power. However, the generation source requires to be cooled down to helium temperature which is a significant drawback for practical modern THz instrumentation.[2] Much higher frequencies, optical side of the electromagnetic spectrum, can be generated with usage of semiconductors via interband diode lasers. [3] In this technique, light is generated via the radiative recombination of electron-hole pair through the band gap of active material. Due to lack of proper semiconductors that can be used in far IR region, this concept cannot be employed.

THz technology has advanced remarkably but for further improvements in exploring nonlinear phenomena in various materials, intense THz sources are required. [4] Bright, intense, tunable and pulsed (~3 to 10 ps) THz radiation can be obtained with recently developed systems such as synchrotrons and free electron lasers.[5] However, these systems are very expensive and require utilization of advanced facilities. Due to complications in fabricating solid-state THz sources, intense attention has been focused on all-optical techniques for producing THz light. These techniques employ visible/near-infrared, femtosecond pulsed lasers. Two of them will be mentioned which are Photoconductive antenna (PCAs) and Optical rectification.

Photoconductive antennas (PCAs) were first reported by Auston and coworkers in 1984 for production of THz light from ultrafast laser pulses.[6] PCAs are one of the well proved and frequently used THz generators due to their relative simplicity, high performance and low cost.[7] A PCA for generation of ultrashort THz pulses is illustrated in Fig. 1.2. PC emitter is a semiconductor material and among these, GaAs, Si and InP are widely used.[8] Two metal electrodes supply the bias to the photoconductive gap and an antenna structure is constructed.

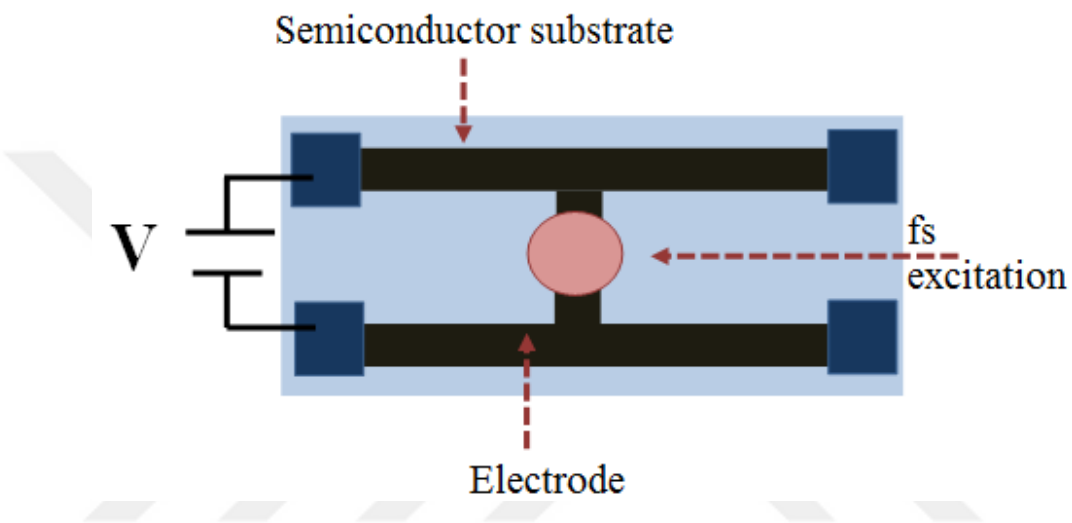

Figure 1.2. PCA for generation of ultrashort THz pulses.

PCA works with absorption of visible or near-infrared ultrafast laser pulse (of 100 – 200 fs pulse duration or less) depending on the band gap of the material of choice. With absorption of photons, electrons are transferred to conduction band from valance band where they are accelerated by external DC electric bias. Resulting transient current gives rise to emission of transient electromagnetic radiation. The carrier life times of specific semiconductor material control generated pulse duration. When picosecond and sub-picosecond carrier life times are employed, outcome falls into the THz region.[9] In PCA method, spectrum of generated THz beam strongly depends on geometry of antenna, substrate material, geometry of the active area, and the pump laser pulse.[10] Length and width of the dipoles affect peak frequency and intensity of emitted THz drastically. Furthermore, efficiency of generated THz can be increased

by increasing the aspect ratio of the dipole.[11] Optimization studies for designing structures with very short carrier lifetime and simultaneously high-carrier mobility are still being conducted.

Optical Rectification (OR), another commonly used intense THz generation method, is a second order nonlinear process which uses non- centrosymmetric crystals such as Zinc Telluride (ZnTe). Generally, OR refers to production of quasi-DC polarization as a result of interaction of intense optical beam with nonlinear medium. It depends on difference frequency generation which is a result of mixing broad spectrum femtosecond laser light at frequencies ω_1 and ω_2 to produce radiation at the much lower frequency of ω_1-ω_2. In case of femtosecond laser pulses, depending on the frequency components of pump, time dependent polarization change in the nonlinear crystal creates THz frequency range. Several parameters affect the efficiency of created THz light. First of all, used nonlinear crystal should be transparent at all employed pump frequencies with high damage threshold since OR requires usage of intense femtosecond pulses. Other physical properties of crystal such as absorption, diffraction and phase matching condition should be considered cautiously. Especially, matching optical group velocity and the THz phase velocity is significant for produced THz waves to add up constructively and form an increasing electric field.[8] OR process is much easier than PCAs since it does not require external high voltage power sources. Moreover, OR gives broader bandwidth with quite high pulse energies along with high electric fields.[12,13]

1.3 THz Detection Techniques

Detection of the THz pulses can be done with PCA and Electro Optic Sampling (EOS), which is the inverse process of OR. These coherent time-gated methods are insensitive to thermal backgrounds and can be very beneficial under high temperature experiment conditions. [14]

Structure of PCA used for THz detection is identical to the emitter structure. Semiconductor substrate is synchronously gated by an optical pulse, forming

electron-hole pairs. Unlike the emission case where detector antenna is not biased with an external electric field, here the intensity of THz electric field results in current flow through the antenna.

Free space EOS is a coherent pulse detection technique which has been used widely. [15] EOS is based on copropogation of a linearly polarized optical sampling pulse and THz through a nonlinear detection crystal. THz electric field causes a change of refractive index along one axis of the EO crystal. This makes crystal slightly birefringent through Pockel's effect and polarization of optical pulse becomes elliptical depending on the intensity of THz electric field. A quarter-wave plate sets the intensity difference on the balanced detector to zero when there is no THz electric field present. Then optical pulse is separated into two optical orthogonal components and sent to a balanced photodetector. Detector captures a sample of time varying THz pulse at each sampling pulse and difference in polarization gives the time dependent THz amplitude information. With EOS technique both phase and amplitude of THz pulses can be detected with accuracy. Efficiency of EOS technique depends on many parameters such as: absorption and dispersion inside the crystal, phase-mismatch, and geometrical overlapping between THz and optical sampling pulse.[16]

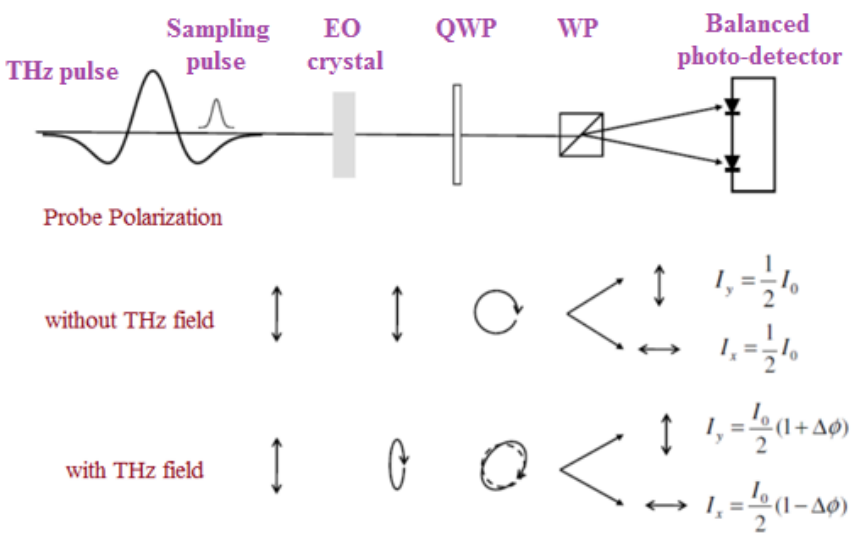

Figure 1.3. Principle of electro-optic sampling.[17]

1.4 THz Spectroscopy Systems

With the improvements in THz range during the past three decades, THz spectroscopy has become a mature field, and technique is employed worldwide in hundreds of research laboratories. Further enhancement of THz spectroscopy will find extensive applications in industry. Nowadays, there are studies which are being focused on improvement of THz spectroscopy by making it faster, smaller, more stable, and less expensive. Basic information on THz time domain and time resolved THz spectroscopy systems will be given in the following sections.

1.4.1 Terahertz Time Domain Spectroscopy

Fourier transform spectroscopy (FTIR) was the most applied technique in far IR before exploration of Terahertz Time Domain Spectroscopy (THz-TDS). FTIR with its very broad bandwidth is a widely used technique especially in analyzing molecular resonances.[18] In this technique, sample is irradiated with broadband sources such as SiC globar. With the help of an interferometer, measurement is carried out and signal is detected via direct detectors such as helium cooled bolometer. Fourier transform of the signal gives spectral information and absorption coefficient of analyzed material directly. However, this technique suffers from limited spectral resolution in THz range.[14] Moreover, one important disadvantage is the loss of phase data which makes it difficult to extract refractive index. It can only be derived with a process of the Kramers-Kronig relationship.[19]

THz-TDS technique was first built in the 1980s at AT&T Bell Labs and the IBM T.J.Watson Research Center.[20] In 1990, Grischkowsky and coworkers indicated that this spectroscopy technique could be implemented in the lower THz frequencies efficiently.[21] It uses broadband, short pulses of THz radiation, which are produced with femtosecond laser based techniques. With the advent of mode-locked titanium sapphire femtosecond lasers, which can provide more stable pulses with higher energies, THz-TDS systems were also improved. A THz system is basically consists

of a femtosecond laser, a THz emitter and detector, optical elements that couple and propagate THz from source to detector, samples, a chopper, delay stages, a lock-in amplifier, and a data acquisition system. The mode-locked laser which is often a Ti:Sapphire laser, produces a train of femtosecond optical pulses with a duration of less than 100 femtosecond. Laser pulse is divided into two arms; one arm is employed in the generation of THz from an emitter nonlinear crystal or photoconductor antenna. Second arm functions as probe arm. Mechanical stage adjusts time delay between THz generation and detection optical arms to rebuild the THz waveform in the time domain. Mechanical stages are controlled with a computer which records data from the lock-in amplifier. Modulation required for lock-in amplifier is obtained from an optical chopper, which is generally placed right after THz emitter, for better signal to noise ratio (SNR). For efficient coupling between emitter and detector, optic elements such as lenses play a significant role. Teflon, Silicon or TPX lenses are often the choice of material and they are attached to the emitter and detector. Generally, parabolic mirrors are preferred in the collimation, and focus of THz light onto sample and collection after sample in free space.

With data acquisition system, not only intensity but transmitted THz electric field itself is measured coherently. By this way both amplitude and phase data can be obtained. Fourier transform of time domain reference and sample data allows extraction of static optical properties such as absorption coefficient, complex refractive index with a precision of 0.1 %, and complex permittivity which is the basis of THz-TDS.[22,23] In order to be able to transform time domain waveform into frequency dependent parameters accurately, cautious processing and modelling of the transmission and reflection of the THz radiation through the sample are vital.[10]

Time resolved, coherent nature of THz-TDS and its capability in characterization of static properties of samples with high SNR makes it quite attractive in a wide variety of application areas. One of the main application areas is material characterization such as semiconductors,[21,24–26] conducting polymers,[27] and high temperature superconductors [28]. THz-TDS is also commonly preferred in areas such as molecular spectroscopy, biology, and quality control.[29]

1.4.2 Time Resolved Terahertz Spectroscopy

Although THz-TDS is an extensively employed time domain technique with distinguished advantages such as coherent detection, determination of both absorption coefficient and refractive index with broad bandwidth, it does not provide time resolved dynamical information. However, Time Resolved THz Spectroscopy (TRTS), which is an extension of THz-TDS, is an ideally suited technique for nonequilibrium measurements. In this technique, an optical pump arm is used as a third arm which can be derived from the same laser. Once the sample is exposed to a femtosecond optical pulse, charge carriers are created. Then, the following evolution of charge carriers in time can be examined with the help of delay between optical pump pulse and THz pulse. THz pulse and optical pump spatially overlap at the sample at different pump probe times providing direct access to the time scales of the evolution, and mechanisms of carrier cooling, trapping, and recombination, in addition to the dynamics of quasiparticles such as excitons. [30]

TRTS is a unique measurement technique for photo induced conductivity with sub-picosecond time resolution at low electric fields (kV/cm).[31] This time resolution, one of the most powerful characteristics of the system, brings new insights for exploring the early dynamics of samples after photoexcitation. While all optical pump probe techniques provide very high time resolution, they can only sense the occupation of the probed states and do not provide any fingerprint information of the charge transport mechanisms.[32] It is possible to get information about the transport mechanism with time of flight or time resolved microwave conductivity methods, but only nanosecond resolution can be achieved.[33] Transient Stark Spectroscopy can provide picosecond time resolution and sensitivity to the transport properties. Nonetheless, high electric field (MV/cm) requirement, which affects the charge mobility, makes it less desirable.[34]

TRTS has been extensively employed to investigate the physical properties of semiconductor nanostructured materials, such as nanowires[35,36] and nanoparticles[37] in recent years. An important benefit of TRTS is that it can differentiate free and

localized carriers, excitons and surface plasmon resonances, all of which have different signatures of photoconductivity. Due to dimensions of nanomaterials, fabrication of Ohmic contacts can be quite challenging. Also contact resistances may affect electrical measurements.[38] Therefore, contact free nature of this technique makes it extensively desirable. TRTS technique allows determination of the complete THz probe wave as a function of pump probe delay time.[39] Therefore, provided that optical pulse creates a sufficiently strong differential change on THz signal, not only one-dimensional (1D) but also two dimensional (2D) scans can be done for extracting far IR complex conductivity.

1.5 THz Applications

After 1980s, with the development of laser based THz-TDS,[21] THz technology has exploded to the extent that it is now possible to carry out a diverse range of real world applications ranging from nondestructive imaging, spectroscopy, and short distance high-capacity wireless communications[40] to basic science.[17]

Due to its unique nature, THz light has some remarkable properties. It can penetrate through most non-metallic and non-polar materials, plastics, glasses, woods, ceramics, paper, and cloth, which are opaque to visible light.[41] This technique has a better penetration depth compared to NIR and visible, and provides better spatial resolution resulting in better imaging compared to microwave.[42] Also due to its imaging capability, THz is a complementary technique to X- ray imaging without the problems of ionizing due to its low energy. [42] Therefore, THz does not possesses any hazards for living organisms as X-rays do. With its nondestructive and noncontact properties, THz imaging, has potential for practical applications such as inspection of biological samples, pharmaceuticals, biomedicine, art conservation, security screening of passengers and container screening [43]. THz waves are absorbed by water strongly. However, its penetration to human tissue is not much and it is safe for biological applications such as skin cancer, breast tumors, and cervical cancer.[44]

THz light involves a wealth of spectral information and it can provide excellent spectroscopy. Numerous organic molecules have strong absorptions and dispersions due to dipole allowed rotational and vibrational transitions.[10,41] Since these transitions are specific to molecules, fingerprint information can be obtained. The location and amplitude of absorption peaks utilize identification of molecules, and by this way chemical composition analysis can be performed. THz spectroscopy is especially quite functional in the detection of common explosives and drugs of abuse since they have unique THz fingerprints.[45] Furthermore, structure and function of biomolecules such as biomolecular hydration, binding, conformational change, and oxidation state change can be analyzed with THz spectroscopy.[46] THz waves are sensitive to collective motions of big molecules such as polymers which interact with each other strongly.[47] This inter molecular interactions causes broader resonances rather than sharp rotational peaks, which can be detected by THz-TDS. Also, other complex properties of polymers such as skeletal vibrations, liquid-lattice modes, intermolecular vibrations in the crystalline phase, or hydrogen bonds can be identified.[47]

THz waves have been the choice for characterizing transient, ultra-fast photo conductivity and charge carrier dynamics of variable materials. Understanding charge carrier dynamics is significant for designing wide variety of potential electronic and optoelectronic devices. Also, THz waves help in the investigation of the behavior of carriers in order to obtain optimized materials for applications such as organic solar cells [48,49] .

1.6 Aim and Organization of this Thesis

Aim of this thesis was to construct two new home-built terahertz spectrometer systems, THz-TDS and TRTS. First system, THz-TDS, is based on linear spectroscopy and determines the optical properties such as complex refractive index, absorption coefficient, and complex permittivity of materials in the THz region. Second optical setup system, TRTS, is a time resolved spectrometer and it measures time dependent photo induced conductivity and charge carrier dynamics of the

materials with sub picosecond resolution. In addition to being a fairly new technique, TRTS systems are very few in Turkey emphasizing the importance of building such a system. With TRTS, photo induced conductivity of novel materials can be measured directly without the need of electrical contacts, which can affect the overall performance of the device and interfere with the potential intrinsic efficiency of the material under investigation. Since TRTS technique requires output of an amplifier laser that has high power, very short pulse-width with moderate repetition rates, both systems were built at ultrafast laser spectroscopy laboratory at UNAM, Bilkent University which has the Spitfire amplifier laser.

The thesis contains 6 chapters. In the first chapter, basic concepts regarding THz are introduced. Chapter 2 presents design, construction, characterization and optimization of THz-TDS and TRTS along with the theoretical aspects. Chapter 3 gives information about graphene and demonstrates the application of THz-TDS in the characterization of SLG and MLG THz modulators. Chapter 4 focuses on utilization of THz-TDS in the characterization of complex sheet conductivities of several SLG and MLG samples. Chapter 5 is based on investigation of THz charge carrier dynamics of graphene samples with different optical pump colors and fluencies on different substrates at room temperature. Finally, chapter 6 summarizes the important aspects and results of the study.

CHAPTER 2

CONSTRUCTION OF THz SPECTROMETERS

Construction of two THz spectrometers, both working in the transmission mode, constitutes the main part of this thesis. Transmission geometry is preferred since it allows for an easier and controlled alignment and data analysis. However, in case of highly opaque and absorbing samples, reflection geometry can be beneficial. All the experimental work carried out during this thesis studies was conducted at Femtosecond Laser Laboratory at UNAM-Bilkent University.

The following parts present the construction of both spectrometer systems starting with Section 2.1, which introduces the main component of spectrometers, laser system. 2.2 gives design and construction details of THz-TDS set-up. Section 2.2.1 explains data collection and analysis of THz-TDS system, while 2.2.2 clarifies the determination of optical constants. THz-TDS part is completed with 2.2.3, which demonstrates the system characterization. TRTS part starts with section 2.3 and 2.3.1 covers data collection and analysis, while 2.3.2 describes system characterization. After completion and characterization of the systems, signal optimization studies are shown in section 2.4. Finally, Section 2.5 gives a brief summary of the Chapter 2.

2.1 Laser System

The most important component of high resolution spectroscopy systems is the femtosecond lasers. Stability of the laser system both in power and pointing direction determines the accuracy and validity of used technique. Mode-locked Titanium:Sapphire (Ti:Sa) lasers are the most widely used, commercially available, and tunable lasers. In these lasers, octahedrally coordinated Ti^{3+} ions dope lasing medium of sapphire (Al_2O_3) crystal. The popularity of Ti:Sa lasers come from their

solid state active medium, which allows for long operation time and compactness. Also high thermal conductivity, extraordinary chemical inertness, and mechanical resistance of sapphire makes it a very valuable lasing medium. Finally, they can provide broad spectrums extending the wavelength range over 400 nm between 670 and 1050 nm.[50]

Femtosecond laser amplifier system consists of 5 different laser systems which are Millennia, Tsunami, Empower, Spitfire, and Optical Parametric Amplifier.

Millennia is a continuous laser radiating at 532 nm with a tunable power output up to 5 W optical power. It is used as pump for mode-locked femtosecond oscillator called Tsunami. Tsunami can emit light from 690 to 1080 nm with pulse durations from 80 ps to 50 fs at a repetition rate of ~80 MHz. Pulse energy is ~12.5 nJ with peak power of ~125 kW (Fig. 2.1). Millennia pumps the Ti:Sa crystal inside the cavity of the oscillator and femtosecond operation is achieved with passive mode-locking of the emission. Average power between 500-800 mW with a ~100 fs pulse duration at 800 nm wavelength is used in our experimental studies. Each of these parameters has to be controlled and satisfied daily before directing the output to the regenerative amplifier, called Spitfire, as seed beam.

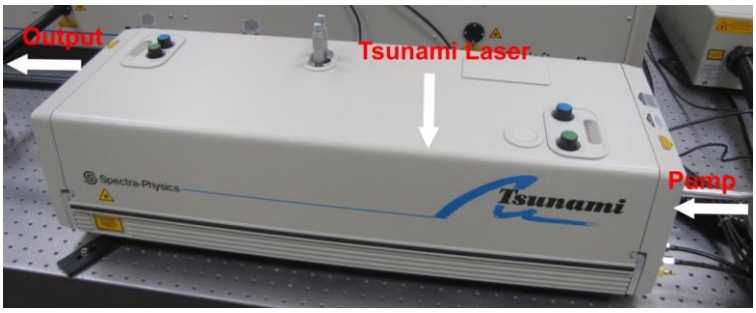

Figure 2.1. Tsunami femtosecond laser.

Empower with an average power of 15 W, and with a repetition rate of 1 kHz at 527 nm functions as pump source for amplifier laser, Spitfire. Spitfire is the Ti: Sa amplifier laser which produces an average of 3 W power with 3 mJ energy for each

individual pulse. It works at 800 nm wavelength with ~150 fs pulse duration and 1 kHz repetition rate, (Fig. 2.2). The chirped pulse amplification process is employed for the amplification in order to prevent optical damage due to high peak light intensity.[51] The incoming seed pulse is stretched in time with usage of diffraction gratings. After amplification of stretched seed light in the resonant cavity by stimulated emission in pumped Ti:Sa crystal, light is compressed to femtosecond duration again with the same process (Components of the Spitfire Fig. 2.3).

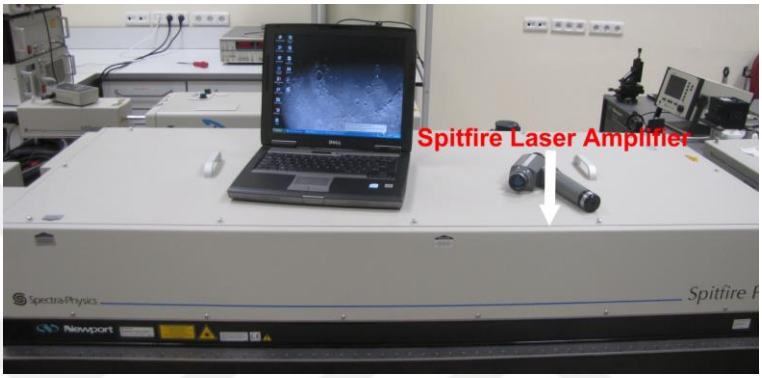

Figure 2.2. The Spitfire laser amplifier.

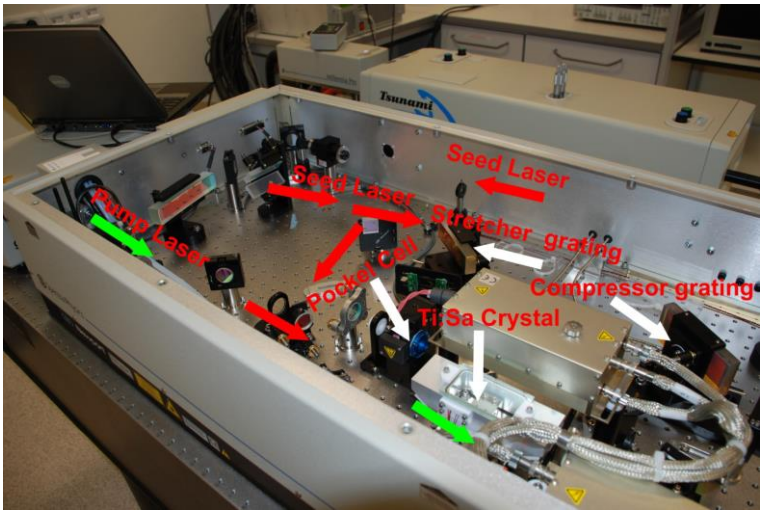

Figure 2.3. Components of the Spitfire laser amplifier.

The amplification process is separated into two parts. First part is the regenerative femtosecond amplifier where the amplification process reach saturation with several roundtrips of seed pulse in the active medium. Secondly, booster part where seed only passes once and the pulse energy is nearly doubled. High voltage switched Pockell cells control the injection and release of only one seeding oscillator pulse into the regenerative amplifier cavity within amplification period. In Table 2.1 the specifications of the laser system are given. The energy of the seed pulse is increased approximately by a factor of 10^6.

Table 2. 1. Summary of the specifications of the laser system.

Laser Type	**Oscillator**	**Amplifier**
Model	Tsunami	Spitfire
Center Wavelength	800 nm	800 nm
Bandwidth	13 nm	10 nm
Pulse Duration	~100 fs	~150 fs
Pulse Energy	~12.5 nJ	~3 mJ
Repetition Rate	80 MHz	1 kHz

The last system is the optical parametric amplifier (OPA). OPA can produce fs pulses in a range of 300 nm to 10 μm wavelength with an average power level of 5 to 125 mW. Production of such a wavelength range is especially important for pump-probe studies. However, in our experiments we could not use OPA efficiently. Instead, 400 nm light was generated directly, through frequency doubling, by using the nonlinear crystal inside of the OPA.

2.2 THz-TDS Set-Ups

The construction of our system was started with a simplified version of the final design. Original design was based on a nonlinear emitter crystal for generation. Initially, the system was constructed with antenna, which requires lower energy. Getting some experience on working with oscillator laser, optics and light alignment

was beneficial before moving onto amplifier laser which has a quiet high energy output.

Figure 2.4 presents the antenna generation THz-TDS set-up. The output of Ti:Sa oscillator, 800 nm, 80 MHz with an average power of 600 mW, was divided into two with a 95/5 wedge beam splitter. The transmitted light (98%) was used in the generation arm while reflected part (2%) was directed to ZnTe crystal for EOS. Aligning the light with a wedge beam splitter is important since wedge geometry decreases reflections coming from the second surface. By this way, optical performance is not affected from any etalon effect.

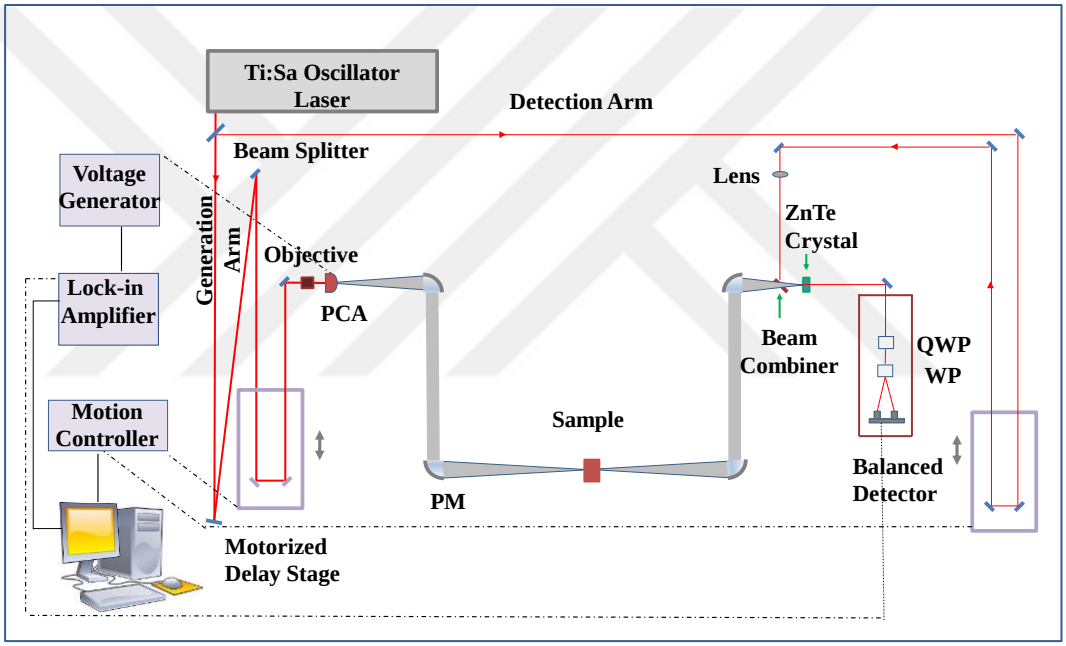

Figure 2.4. THz-TDS system with PCA.

Light was focused onto generation source, Butterfly antenna PCA -44 -06 -10 -800 -x manufactured by Batop, with a 40x objective (f=0.05mm). Main specifications of PCA are shown in the Fig. 2.5 taken from BATOP website.

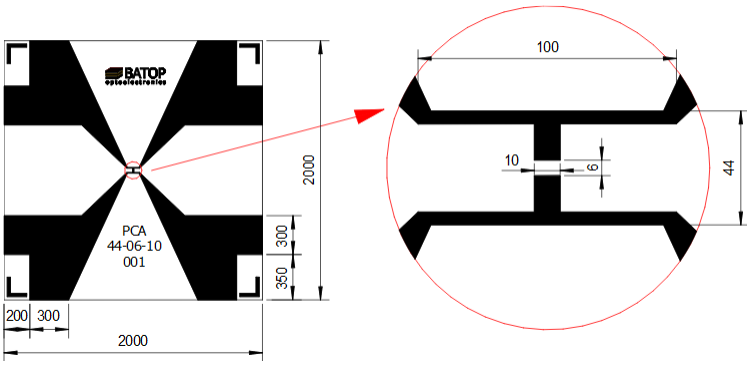

Figure 2.5. BATOP Antenna Design.

GaAs antenna gap is 6 µm with a 10 µm length. Focusing light into this tiny distance is crucial for effective generation. Therefore, PCA was placed on a XYZ stage to be able to arrange its position meticulously. Laser power was arranged as 60 mW to make sure not to damage the antenna. PCA was connected to a function generator that provided 10.92 V (AC) with 1 kHz repetition rate. Generation quality were checked initially by measuring the drop in resistance of antenna with a voltmeter. The lowest resistance measured was 150 kΩ corresponding to the maximum amount of produced THz. Off axis parabolic mirrors (OAPM) were employed in the transfer of generated THz beam to the detection crystal. Firstly, system was installed with two OAPMs then quickly switched to four OAPM design. With four OAPM, it is possible to collimate and focus THz onto sample which is especially important for non-uniform samples. Furthermore, four parabolic mirror system gives flexibility since length of collimation parts can be arranged depending on the design.

Set up included two motorized mechanical translational stages with 10 and 15 cm lengths. The spectral resolution gets better with a longer delay time. A long scan range is especially important to follow the dynamics up to 1 ns, which requires a mechanical stage with a travel distance of 15 cm. In order to record THz pulses, detection stage was scanned. By this way, sensitive alignment of PCA is not affected by any probable change due to movement of mechanical stage. Movement of stage was controlled by a motion controller, which was connected to the computer through Labview software

program. THz beam was focused on detection crystal, 1 mm thick ZnTe, and was overlapped with detection beam which passes through mechanical stage and focused onto crystal with the help of a lens (f=20 cm) and a mylar beam combiner. Mylar is a type of polyester material and highly transmissive to THz while it reflects a little amount of 800 nm light. Generation and detection optical beam paths must be equal in length precisely in order to overlap effectively. This is a quiet difficult process since THz light cannot be seen or measured by any means of optical or electronic device. Furthermore, after mylar beam combiner, sampling light had a very low power which can only be seen through an IR camera. Therefore, matching THz beam which has a pulse duration of approximately 1.5 ps with sampling light which has a pulse duration of 150 fs is very challenging. This requires that there should be no more difference than 0.45 mm, corresponding to 1.5 ps, in optical paths of detection and generation arms. This can only be corrected and achieved with the employment of mechanical stages.

A standard EOS was employed for detection as described in section 1.3. After sampling light passed through detection crystal, it was directed onto quarter wave plate with a gold mirror. After that Wollaston prism separated sampling light into its polarizations and directed to the balanced detector. Change in polarization of sampling light depending on electric field of THz beam was recorded relative to the pump sampling delay time. It was important to set quarter wave plate to the correct angle that would enable detector to read zero signal in the absence of THz beam. The signal detected by balanced detector was directed to the lock-in amplifier. Modulation needed for lock-in amplifier to reduce the noise level came from the function generator. By building narrow frequency filter to transmit only the frequency of pump modulation, Lock-in improves the SNR of the system.

In order to find the THz signal, generation and detection arms were equalized carefully so that THz pulse and sampling light were overlapped at the detection crystal simultaneously. In order to be sure of distance equality, measurements were repeated several times. After alignment was completed, generation and detection crystals were removed. A photodiode was placed into the position of detection crystal, and timing

of pulses coming from both arms onto photodiode was checked with the help of the oscilloscope. After observation of the exact matching of pulses in time, crystals were located into their old places. By iteratively changing the angle of crystals through rotation mounts, amplitude of signal was increased. Formation of green light on generation crystal was the sign of THz generation.

One of the initial time dependent THz pulse profile and its corresponding power spectrum is given in Fig. 2.6. The obtained profile of the THz signal was not good. This might mainly stem from the alignment of parabolic mirrors. But, since our purpose was only to get experience, we did not optimize the signal and continued with the crystal THz generation. Figure 2.7 presents the picture of the final antenna set-up.

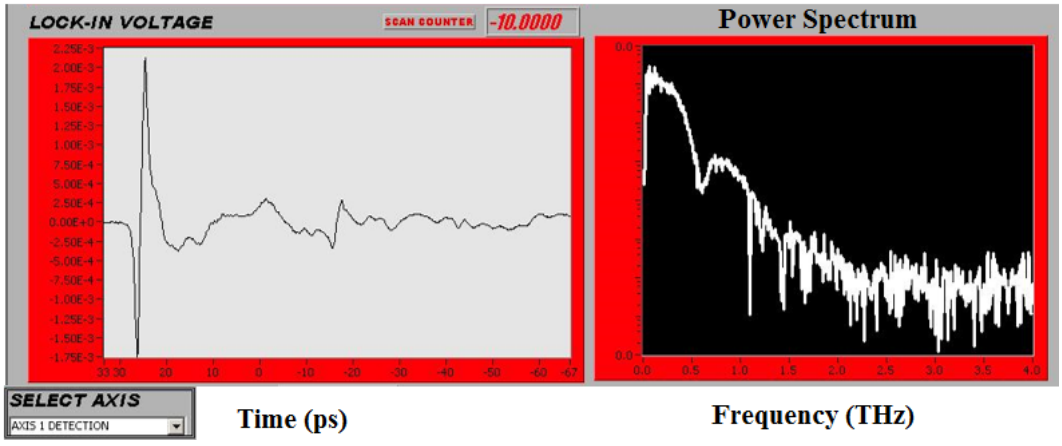

Figure 2.6. THz signal in time domain (left) and its corresponding bandwidth in frequency domain (right).

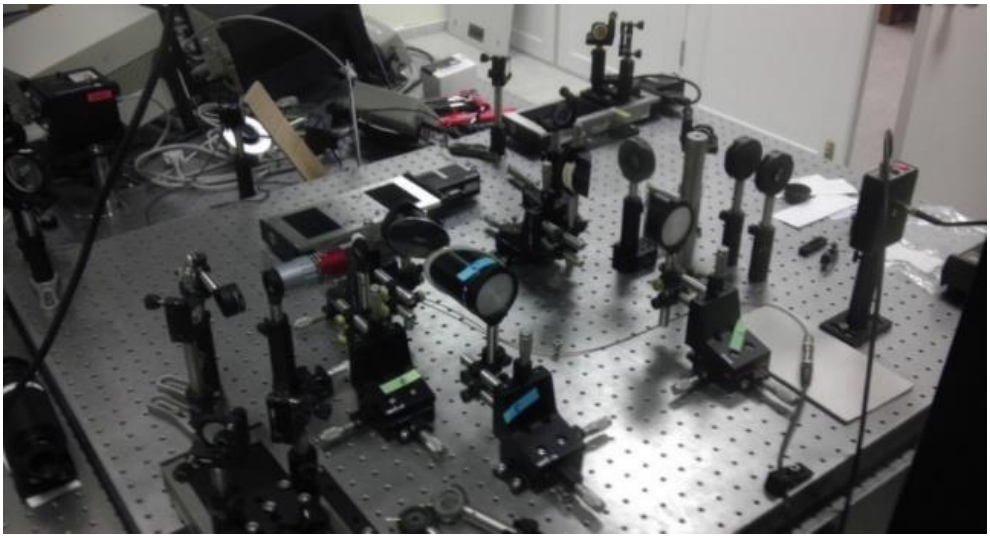

Figure 2.7. THz-TDS set-up with PCA.

The final THz-TDS set-up with crystal generation is given in Fig. 2.8. The system required less than 1 W to operate; therefore, output power of the amplifier was divided with a 70:30 beam splitter to reduce the laser power before directing the light into THz-TDS system. The beam size was approximately 8 mm with a center wavelength of 800 nm. Only 5 % of the power (~15-20 mW) was sent to the detection arm. A 110 ZnTe was used to generate THz light as described in Section 1.2.

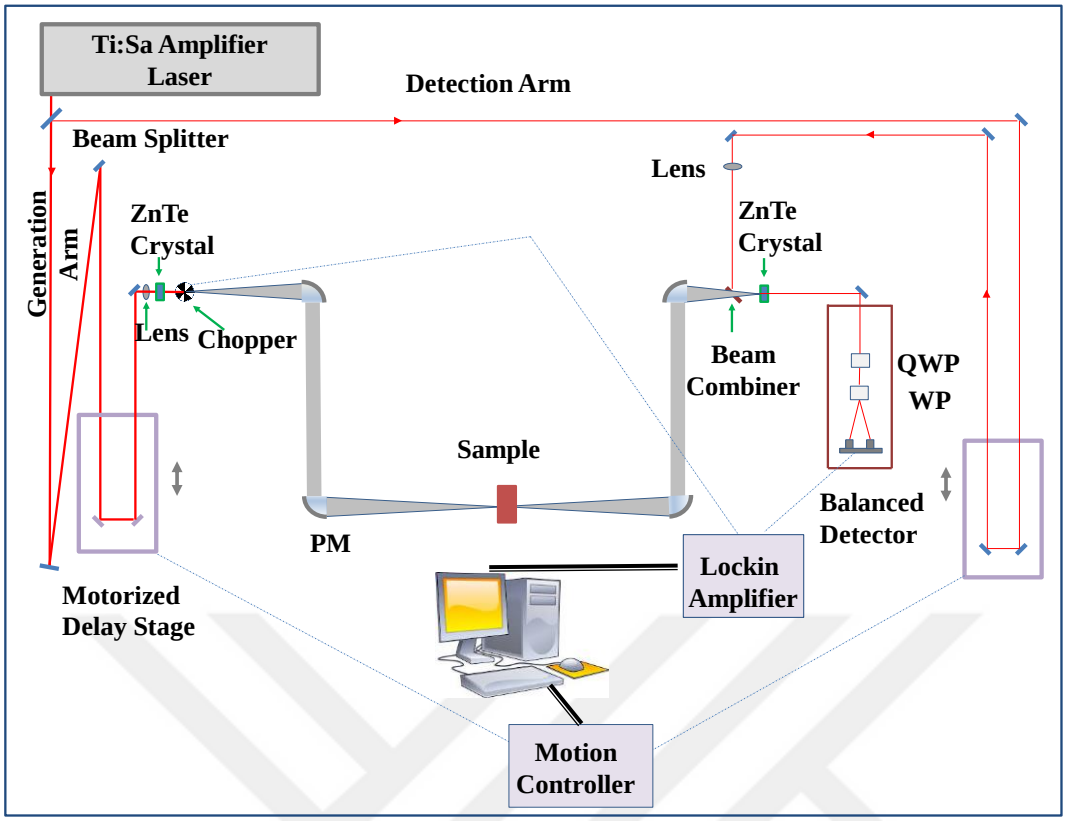

Figure 2.8. THz-TDS set-up with ZnTe crystal.

Higher intensity output of amplifier laser compared to oscillator is preferred in crystal rather than PCAs since the THz generation is a nonlinear process. As it is experimentally observed, OR process is strongly geometry dependent. Therefore, ZnTe is placed onto a rotation mount (Fig.2.9) and when it is rotated around its surface normal, perpendicular to the propagation direction of the laser beam, emitted THz radiation increases or decreases. This phenomenon is known as 'azimuthal angle dependence'.[13] Different than PCA based system, this time an optical chopper was placed right after ZnTe to provide reference signal (Fig.2.9). Chopper functions together with lock-in in the making of reference signal, and they are connected to a data acquisition system to measure the signal. Expected bandwidths is similar in both generation methods, between 0.2-3 THz.

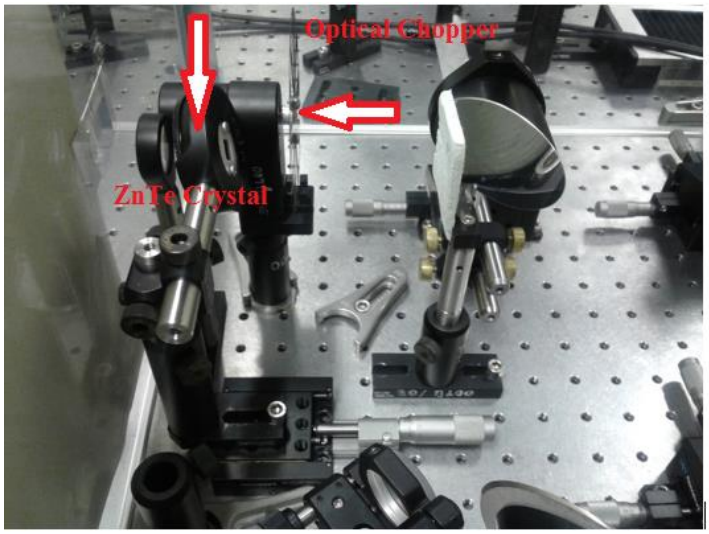

Figure 2.9. ZnTe crystal and optical chopper.

2.2.1 Data Collection and Analysis

The THz pulses are generated with OR process in a 1 mm thick (110) ZnTe crystal and detected via electro-optic sampling in an 0.5 mm thick (110) ZnTe crystal. Time domain profiles are collected using a data acquisition program. The code also controls movement of stages. Figure 2.10 presents the front panel of Labview program. It gives both collected voltage vs time signal and its frequency dependent power response. Through front panel, stage position, scan length (start and finish of scan), step size and wait time can be arranged.

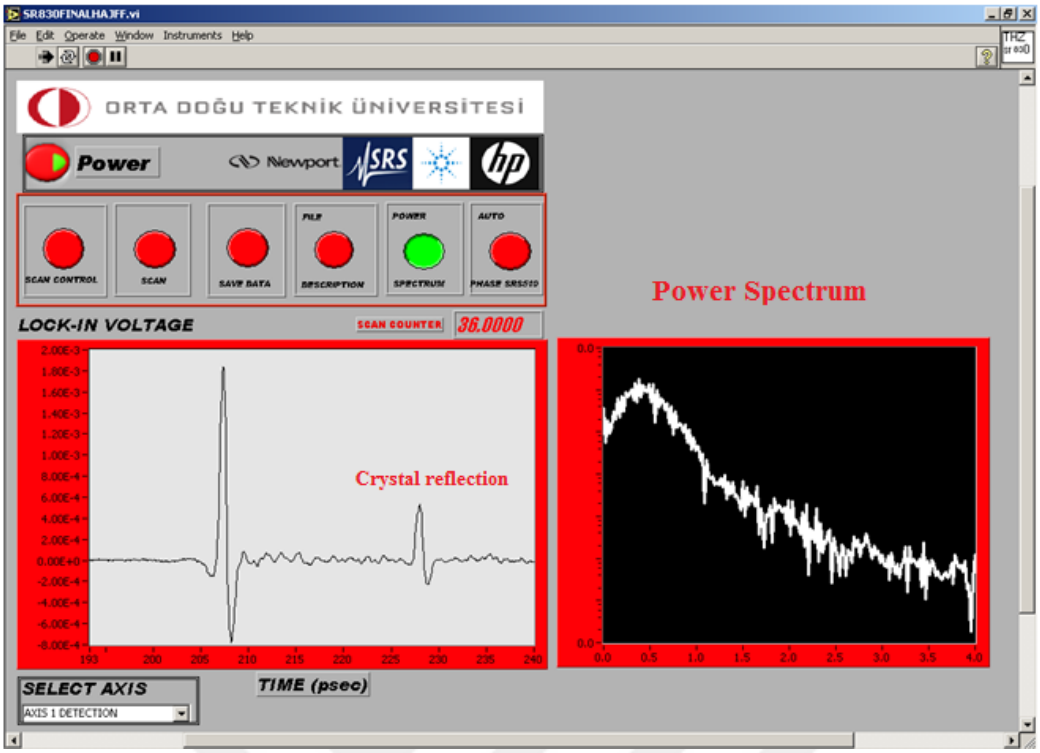

Figure 2.10. Front panel of Labview Software.

In order to collect time domain data, step scan method is used which includes three separate steps. Firstly, mechanical stage is moved through control of the software for a fixed distance. Then it waits for data collection for an optimized time interval and finally reads the output of lock-in as voltage. The delay stage scans all scan length by this way from initial set point to final end point. With this data collection mode, THz wave is scanned by femtosecond laser as given in Fig.2.11, and at each stage movement, one sample point of the signal E(t) is recorded in time-domain with time window of $t = n\Delta t$ ($n = 1\ 2\ 3,...,N$). As a result, THz time domain profile is obtained. Resolution of the obtained THz profile depends on the step size of the mechanical stage and total scanning length.

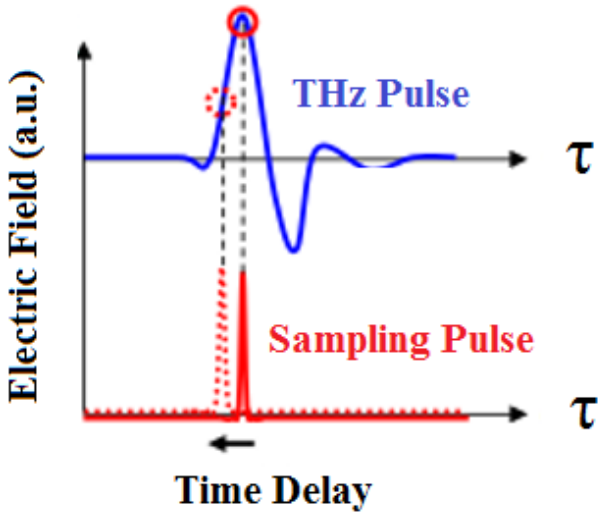

Figure 2.11. Extraction of THz time domain profile.

Optimized step scan and wait time for our measurements were determined as 10 µm and 500 milliseconds. Figure 2.12 illustrates a part of collected THz time domain profile, which has a single-cycle like nature.

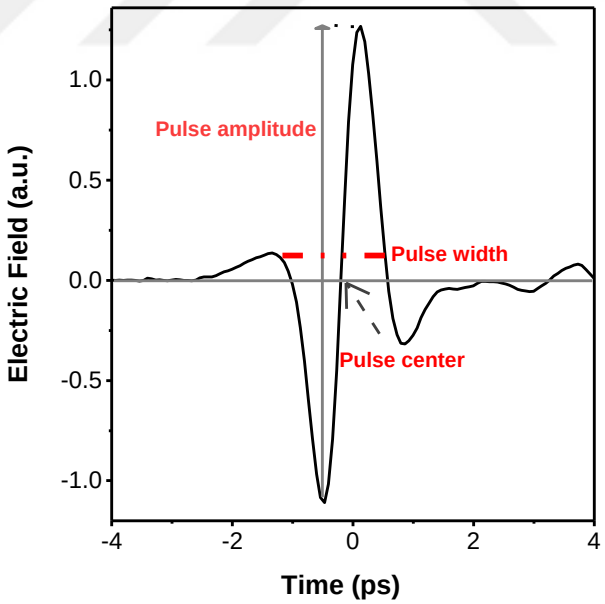

Figure 2.12. The THz pulse shape in time-domain.

THz pulse has three important specifications; pulse center, pulse amplitude, and pulse width, which determine the experimental characteristics such as the dynamic range, bandwidth, SNR, and frequency resolution.

A summary of the main steps in a THz-TDS measurement are given below:

- Switching on the ultrafast laser system and checking the power and spectrum of the fs laser, after an approximately1 hour warm-up depending on the day or right before each set of measurements.
- Checking the alignment of the optical components through reference irises to make sure there is no change in the system,
- Opening dry air inlet to fill the controlled atmosphere environment around the THz set-up (to minimize the water effect in the measured THz spectra),
- Measuring the 1st reference signal which is THz air space signal,
- Measuring 2 nd reference signal which is the THz signal of substrate,
- Measuring the THz signal of sample,
- Measuring air again to compare it to the 1 st reference and test the reliability of the system.

After measurements are completed, data are saved and then transferred to a data processing software. In order to calculate the optical and dielectric constants of the sample, transient electric field of the reference and sample in time domain are truncated with a signal processor that enables time-frequency transform, such as Fast Fourier Transform (FFT).[52] Accuracy of extracted parameters depend on many factors such as noise of the system[53] and signal processing methods. Therefore, output of the software program should be checked at each step. Also during the measurements, it must be assured that sample and reference have same the experimental conditions such as, the step size and scan length. Any reflection is removed from the data in order to prevent possible noise effects introduced by the oscillations. Zero padding is done in order to increase pseudo resolution, if necessary. FFT gives amplitude and phase data in the accessible frequency range.

2.2.2 Determination of Optical Constants

In order to extract meaningful frequency dependent optical properties of sample under investigation, both measurement process and signal analysis are required to be done carefully. Analysis of error sources, such as laser intensity fluctuation and drift in optomechanical components, which may have an impact on obtained THz pulse, is necessary to evaluate the differences that might be observed between experimental and theoretical results. Furthermore, precision in the extraction of parameters is also required. For extraction of optical parameters, time domain THz profiles of sample and reference are collected consecutively. In order to increase SNR by reducing random noise of the obtained signals, repeated measurements are generally preferred. The averaging of signals is done in time domain rather than in frequency domain since it has no effect on decreasing the noise floor.[54] By this way dynamic range, the ratio between the highest and smallest detected signal so the maximum quantifiable signal, can be improved. After reliable time domain measurements of reference and sample are collected, in order to extract optical parameters, FFT transformations are performed to obtain both amplitude and phase data.

By using the ratio of power (square of amplitude) spectrums of sample, P and reference P_0, absorption coefficient of sample can be calculated as given in equation 2.1. Here, d refers to the thickness of the sample.

$$\alpha=\left(-\frac{1}{d}\,ln\frac{P}{P_0}\right) \qquad \textbf{(2.1)}$$

Frequency dependent refractive index of sample can be extracted from the phase difference between sample and reference, $\Delta\phi$ as given in equation 2.2. Here, C is the speed of light, ω is the angular frequency ($\omega=2\pi f$) and n_{ref} is the refractive index of reference.

$$n = n_{ref} + \frac{C}{\omega d}(\Delta\phi) \qquad \textbf{(2.2)}$$

Complex refractive index can be expressed as equation 2.3. where k is the frequency dependent extinction coefficient, $k(\omega) = \frac{c\alpha}{2\omega}$.

$$\hat{n} = n + ik \qquad \textbf{(2.3)}$$

The complex dielectric constant can be expressed as, $\hat{\varepsilon} = \hat{n}^2$ and its real and imaginary parts are given in equations 2.4 and 2.5.

$$\varepsilon'(\omega) = n^2(\omega) - k^2(\omega) \qquad \textbf{(2.4)}$$

$$\varepsilon''(\omega) = 2nk \qquad \textbf{(2.5)}$$

Finally, complex conductivity $\hat{\sigma}$ can be calculated and its real and imaginary parts are given in equations 2.6 and 2.7. Here, ε_0 is the vacuum permittivity and ε_∞ corresponds to dielectric constant at high frequency limit.

$$\sigma_{real} = 2\omega\varepsilon_0 nk \qquad \textbf{(2.6)}$$

$$\sigma_{imaginary} = \omega\varepsilon_0(k^2 - n^2 + \varepsilon_\infty) \qquad \textbf{(2.7)}$$

2.2.3 System Characterization

Although the randomness of the signal can cause some error in the extracted optical constants, imperfections in the set-up also affect the results strongly. These imperfections may be related to the precision of optical alignment, unsynchronized stage movement with data acquisition system. In order to be sure that all of system components function correctly, we chose a solvent from literature, benzene, with known absorption coefficient and refractive index in the THz range.[55] All

measurements were performed at room temperature. After air reference measurement, for optimization of observed THz signal, carefully cleaned empty quartz liquid cell (1 cm) was located at the focus of THz beam as reference measurement. Then, liquid cell was filled with benzene and measured at same conditions. After repeated measurements of reference and sample in the time-domain, by scanning the generation stage to obtain time-delay between the THz and the optical sample pulse, FFT process was performed in order to obtain corresponding amplitude and phase information of both sample and reference. Extracted values of absorption coefficient and refractive index of benzene are shown in Fig. 2.13 (a) -(b).

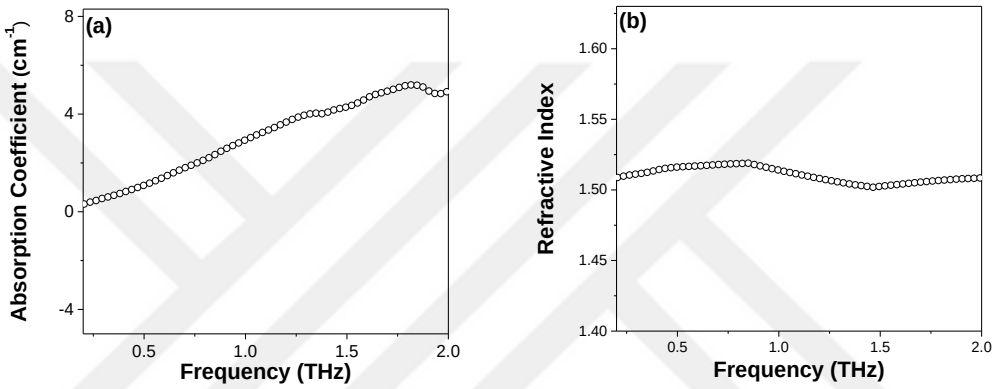

Figure 2.13. (a) Absorption coefficient, (b) Refractive index of benzene from THz-TDS measurements.

Consistency between compared values proved that the THz-TDS system was successfully built.

2.3 TRTS

After completion of THz-TDS set-up, pump arm was designed and integrated to complete the construction of TRTS set-up. Figure 2.14 illustrates the final design of our system.

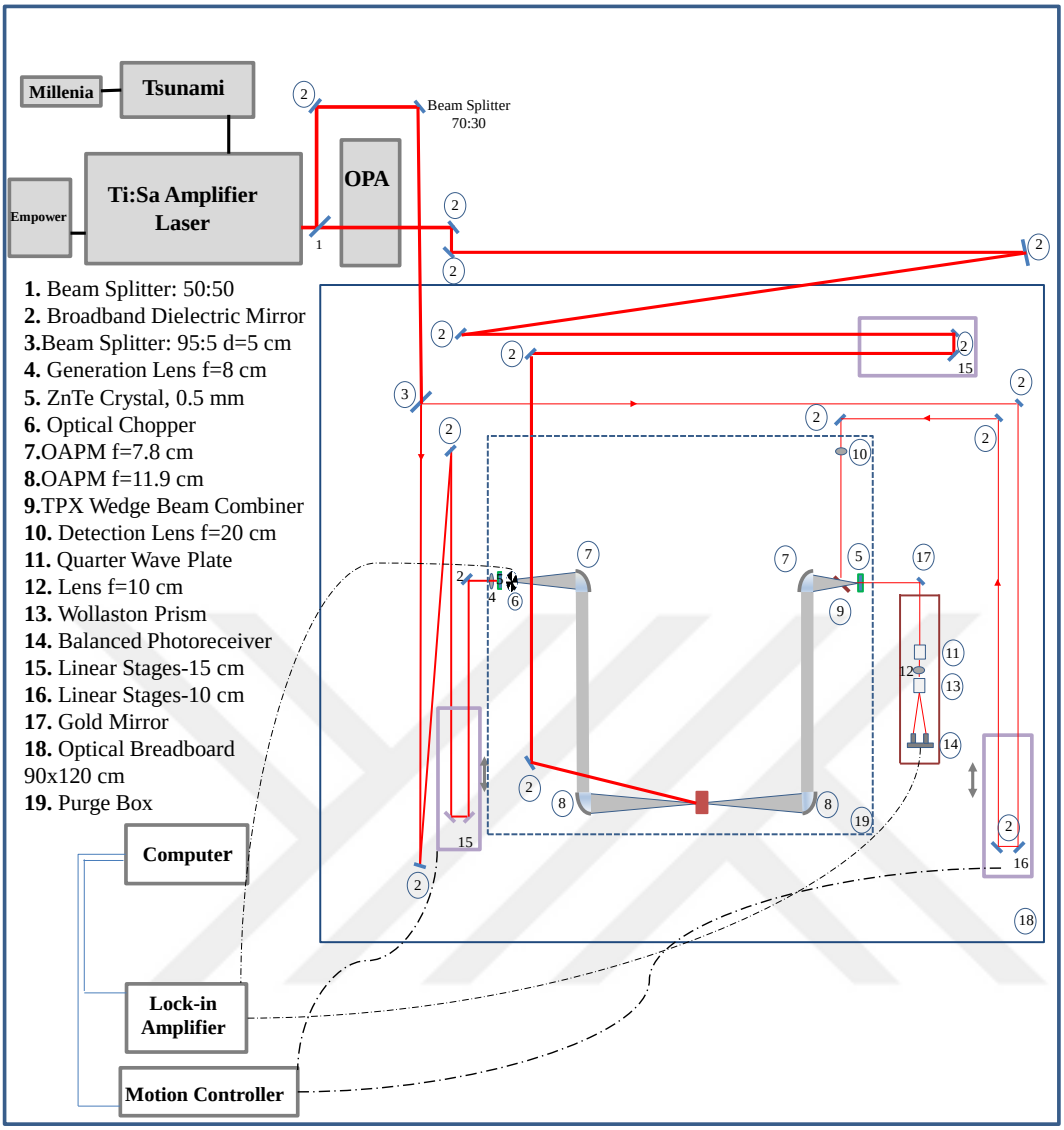

Figure 2.14. TRTS set-up.

The system was designed with addition of minimum amount of optics to minimize reflection losses as much as possible. After completion of the alignment, distances were equalized with the help of an oscilloscope. Firstly, generation crystal was removed and then a photodiode was placed at sample position, which detected lights coming from both generation and optical pump arm. By this way, pump stage was positioned in a way that would provide the scan of the maximum time length after t=0 to obtain decay dynamics almost until nanosecond time lengths.

System components are given in Table 2.2 in detail.

Table 2. 2. Components of TRTS system.

Item	Manufacturer	Model	Specifications
Millenia	Spectra Physics		Continuous laser, 532 nm, Up to 5 W optical power
Tsunami	Spectra Physics		80 fs-50 ps pulse duration, 80 nm pulse width, 80 MHz repetition rate, 800 nm central wavelength, 500 mW output power
Empower	Spectra Physics		10 ns pulse duration, 527 nm, Up to 20 W optical power
Spitfire	Newport		150 fs pulse duration 1 kHz repetition rate, 800 nm central wavelength, 2 W output power
Beam Splitter	Thorlabs	BST11	Ø1" 70:30 (R:T) UVFS Plate Beamsplitter, Coating: 700 - 1100 nm, t = 5 mm

Table 2.2 Continued

TPX Wedge Beam Combiner	Tydex	WW-TPX-D25.4-T2	TPX Plano-plano and Wedged* Windows-wedge is 6 mrad
Dielectric Mirrors	Thorlabs	BB1-E03	Ø1" Broadband Dielectric Mirror, 750-1100 nm
Gold Coated Mirrors	Melles Griot	PG-PM-2506M-C	
Parabolic Mirrors	Edmund optics	NT-47109	FL= 78 mm Off Axis
Parabolic Mirrors	CVI Melles Griot	POA-63.5-59.7	FL= 119 mm Off Axis
ZnTe Crystal	MTI Corp.		<110> orientation and 500 µm thickness
Lens	Thorlabs	AC254-200-B	Ø25.4 mm, f=200.0 mm, Near IR Achromat, ARC: 650 - 1050 nm
Lens	Thorlabs	AC254-080-B-ML	f=80 mm, Ø1" Achromatic Doublet, SM1-Threaded Mount, ARC: 650-1050 nm
Lens	Thorlabs	AL1210-B	Ø12.5 mm, f=10 mm, NA=0.545, S-LAH64

Table 2.2 Continued

Motorized Delay Stages	Newport	UTS100pp	
Motorized Delay Stage	Newport	UTS150pp	
Motion Controller	Newport	ESP301	
Quarter Wave Plate	Thorlabs	WPQ10M-808	Ø1" Zero-Order Quarter-Wave Plate
Wollaston Prism	CVI Laser	WLST-15.0-CA	WLST - WP Polarizer
Large Area Balanced Photoreceiver	New Focus	2307	400-1070 nm- large 8 mm diameter Silicon photodiode
Chopper	Thorlabs	MC2000	Optical Chopper System with MC1F10 10-slot (36°) Chopper Blade

Since TRTS is used to study variations in sample's complex permittivity upon photoexcitation, specifications of the applied optical pump pulse are very important. In pump probe studies, generally an amplified Ti:Sa laser operating at 1 kHz is used due to its lower repetition rates and higher pulse energies compared to a Ti:Sa oscillator. Lower repetition rate, 1 ms for 1 kHz, provides sample with relaxing back to its ground state before arrival of next pump pulse. This time is only 12 ns for an 80 MHz oscillator laser. High pulse energy output of amplified laser is effective in achieving large fluencies, which can create observable differential changes for photoconductivity measurements. This will allow for characterization of material's frequency dependent complex conductivity that is a fundamental knowledge for its

application in electronic and optoelectronic devices. Strength of THz electric field is also important and it is expected to be around 50 kV/cm as reported from a similar set-up [8]. Since THz pulses function as probe beam, higher electric field values are not needed but can be achieved with a higher intensity of the generating optical pulse.[56]

2.3.1 Data Collection and Analysis

TRTS system consists of three independent pulses, which are THz probe pulse, sampling pulse, and optical pump pulse, with their individual spatial positions. Timing between them are given in Fig.2.15.

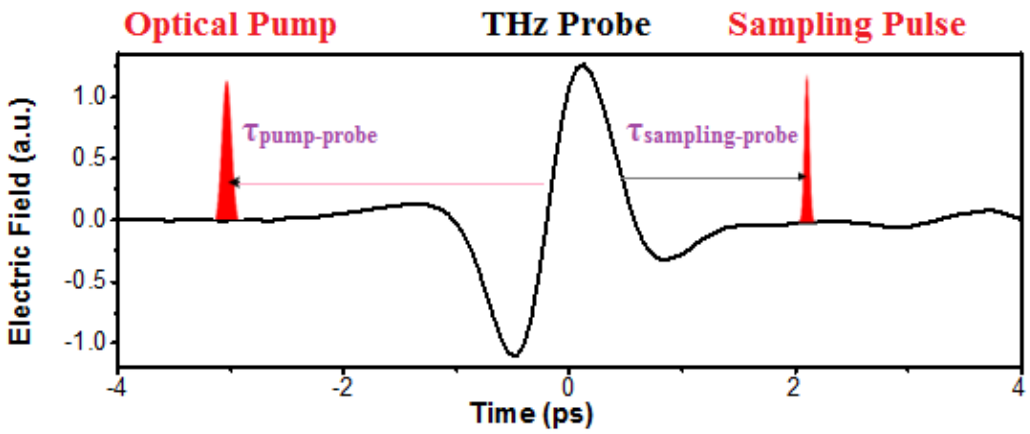

Figure 2.15. Timing relation between THz probe, sampling and optical pump pulse.

TRTS system requires employment of two different delay lines. Interaction of THz probe pulse with the optical pump pulse at the sample position, $\tau_{pump\text{-}probe}$ and interaction of THz probe pulse with the sampling pulse at the detection crystal $\tau_{sampling\text{-}probe}$. Therefore, experimentally obtained THz probe pulse is a function of both $\tau_{pump\text{-}probe}$ and $\tau_{sampling\text{-}probe}$ delay times. Gathering information about the THz dynamics of sample under investigation requires scanning either one or both delay lines depending on the searched information. Generally, one of the delay line is fixed at a specific position and the other is scanned to measure the THz probe signal in a more practical

manner. This leads to implementation of two separate experimental techniques which are one dimensional, 1D and two dimensional 2D.

In 1D experimental technique, sampling-probe delay stage is fixed at a specific point, generally at the peak of THz pulse to observe the maximum signal. Then pump-probe delay stage is scanned to change arrival of the pump pulse relative to THz. With this technique, the differential variation in terahertz field transmission ($\Delta T/T_0$) is measured at a specific point of THz probe pulse. Figure 2.16 shows the time evolution of relative change in transmission of THz peak value obtained by scanning optical pump arm.

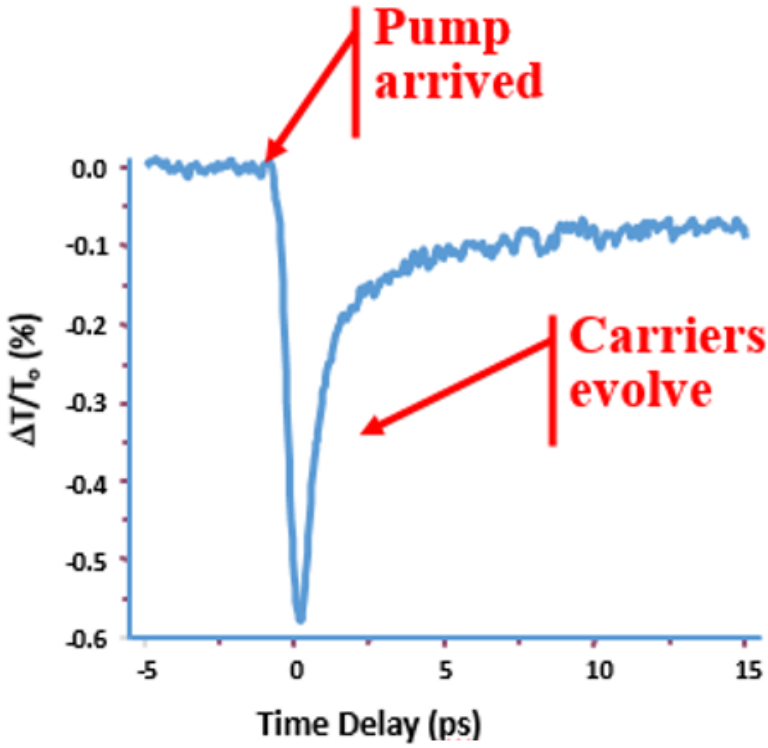

Figure 2.16. Time evolution of the relative change in transmission of THz peak value.

$\Delta T(t) = T(t) - T_0$, $T(t)$ is the time-dependent transmission of THz peak value with pump, and T_0 is the THz peak transmission without pump. If the THz signal is ahead of the pump pulse in time delay line, the time delay τ is negative, then the THz peak value is unchanged, resulting in the zero value of $\Delta T(t)/T_0$. When the THz pulse

begins to encounter the pump pulse, $\Delta T(t)/T_0$ changes remarkably because of the photogenerated carriers in the material. Subsequently, $\Delta T(t)/T_0$ recovers gradually as a result of carrier recombination. It is only possible to get averaged dynamic information about the sample based on the frequency content of the THz pulse. However, 1D experimental technique is not adequate all the time. Employing 2D experiments is especially significant for the cases in which optical pump can induce changes both in amplitude and phase of THz probe pulse meaning photo induction causes a change in refractive index.

In 2D experimental technique, full THz probe pulse is scanned rather than monitoring the peak amplitude. Therefore, pump-probe delay line is fixed at specific times while sampling-probe delay line is scanned for all of these delays. From the measured time domain profiles, frequency domain data is obtained via FFT transformations.

After collection of experimental data, analysis step is performed. For extraction of meaningful results, correct evaluation of data is required. Result of 1D experiments, differential change in the transmission of THz probe pulse at a specific point such as the one given in Fig. 2.15, can be related to the photoinduced THz conductivity of the sample with the equation 2.8, Tinkham formula.

$$\Delta T/T_0 \approx -\frac{Z_0}{n_s+n_{air}}\Delta\sigma \qquad \textbf{(2.8)}$$

This form of the equation is applicable to very thin samples such as 2D materials with confined electron wavefunction in one direction. Here, $\Delta\sigma$ is the photoinduced change in the complex sheet conductivity of the sample, n_s and n_{air} are the THz refractive indices of the substrate and the air, and Z_0 is the impedance of free space. When a thin film material with a finite thickness d and unconfined electron wave function is investigated, photoinduced conductivity is expressed as:

$$\Delta T/T_0 \approx -\frac{Z_0 d}{n_s+n_{air}}\Delta\sigma \qquad \textbf{(2.9)}$$

The overall magnitude of $\Delta T/T_0$ is also proportional to the product of the carrier density, N, and mobility, μ.

$$\Delta T/T_0 \approx \sigma \approx \mu N \qquad \textbf{(2.10)}$$

With the second experimental approach, the frequency-dependent THz response is obtained at a particular pump delay. By this way, transport properties of sample can be modelled which leads to extraction of N and μ separately.

2.3.2 System Characterization

Characterization of TRTS system is necessary to make sure all the physical aspects such as alignment, stage movement, and data acquisition system work properly. Therefore, a very well-known semiconductor material GaAs was chosen to benchmark the system before moving on to exploration of novel materials. GaAs samples were prepared with epitaxial growth technique at 600˚C to 1 μm effective layer thickness on top of a 650 μm SI-GaAs wafer. As optical pump beam, 800 nm light was chosen and experiments were done at room temperature with two different pump fluencies of 16 and 52 μJ cm^{-2}. Pump probe experiments were performed by placing the GaAs sample at the focal point of parabolic mirrors. For obtaining homogeneous measurements, THz and pump beam spot sizes were arranged approximately the same, 7 mm. Experimental parameters are given in Table 2.3.

Table 2.3. Experimental parameters of GaAs optical pump THz probe measurements.

Experimental Parameters	
Experimental Technique	1D
Temperature / Humidity	21 ^{o}C / ~5%
Pump Color	800nm, 1 KHz
Power	~16 mW, ~52 mW
d_pump	7 mm
d_THz	7 mm
Tsunami	675 mW
Spitfire	1.3 W
Lock-in Wait Time	500 ms
Lock in Time Constant	300 ms
Chopper Frequency	500 Hz
Step Size	200 micrometer

Figure 2.17 indicates the differential change in THz transmission with relative pump probe delay time at 16 and 52 μJ cm^{-2} pump fluencies. The initial sharp decrease in the transmission signal stems from the creation of electron-hole pairs that absorb THz light strongly. A subsequent increase in the transmission after the photoexcitation is observed within roughly 1 nanosecond. Decay dynamics depends on the slow recombination of charges that almost lasts on nanosecond scales.

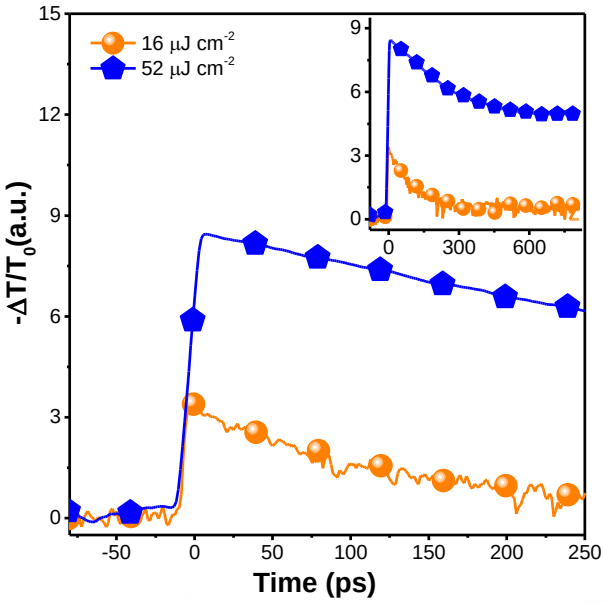

Figure 2.17. The differential transmission $-\Delta T/T_0$ of the peak THz field as a function of the 800 nm optical pump/ THz probe delay time, for 16 and 52 μJ/cm^2, inset shows the decay behavior of long lived carriers.

As illustrated in the inset, the observed relaxation dynamics cannot be explained by a single exponential function which would be the case if recombination process stemmed from only the bulk material. Instead, at initial times, high population of carriers near the surface allows for effective surface recombination as a dominant relaxation process. At long delay times, diffusion of carriers into the bulk of GaAs material turns bulk recombination into the dominant relaxation process. This situation accounts for the double-exponential nature of observed decay dynamics. Results of our pump probe study with observed decay times and dynamics are consistent with literature [57] proving our setup can be employed successfully in the characterization of materials with unknown properties.

2.4 Signal Optimization

After completion of THz-TDS and TRTS systems, optimization studies were required to achieve better SNR. Some basic optimization studies are given in this section.

Firstly, system was enclosed with a plexiglas box for purging with dry air to be able to decrease humidity level (Fig. 2.18).

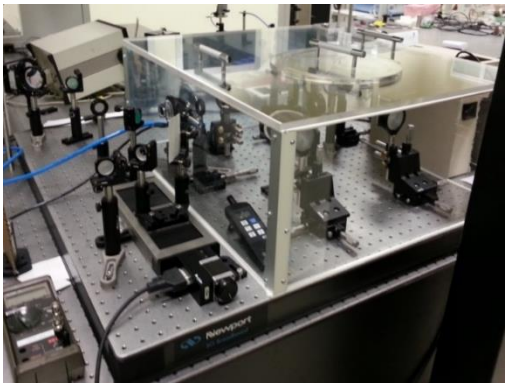

Figure 2.18. TRTS system enclosed with a plexiglass box.

This is necessary because of intense rotational transitions of water vapor in the THz band [58] which cause deep absorption features in the power spectrum, and significant loss in signal amplitude and bandwidth. Signal improvement can be seen in Fig. 2.19 with decreased humidity level.

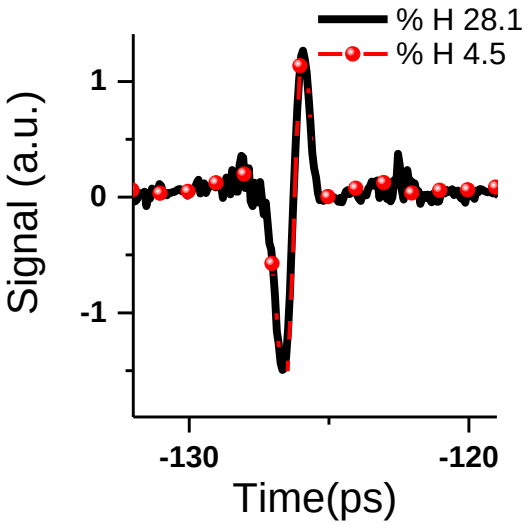

Figure 2.19. Improvement in the SNR of measured THz time domain profile with decreased humidity level.

One of the major components of our systems is the Si based balanced photo detector which is a part of the THz detection technique. Two different large area balanced photodetectors were employed in signal acquisition process; New Focus-2307 and Thorlabs-PDB210A/M.

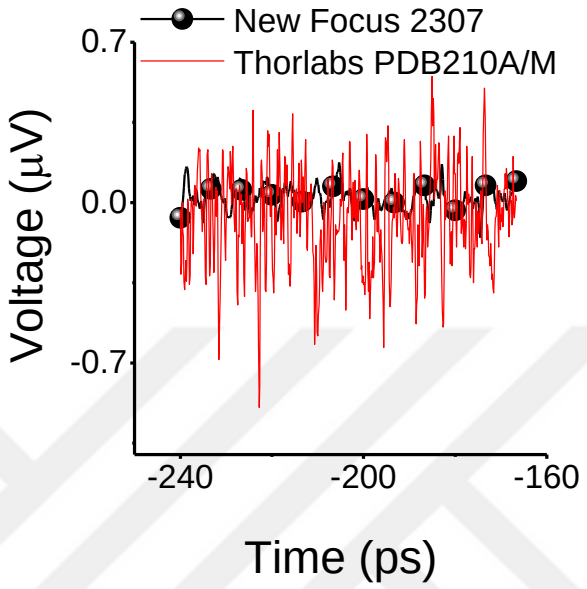

Figure 2.20. Comparison of large area balanced photodetectors, New Focus-2307 and Thorlabs-PDB210A/M.

Figure 2.20 presents decrease in noise level with the use of New Focus-2307. Detection part was also enclosed with a box in order to reduce the noise effect that might come from room light.

Precise alignment of light is required for obtaining optimized THz signal with high SNR. Moreover, misalignment signal losses generally exhibit frequency dependent behavior, and errors in mirror position and orientation especially affect higher frequencies. Therefore, alignment is checked constantly with reference irises that are placed at specific points of the system. Parabolic mirrors guide the THz light and transmit it onto detection crystal. In order to get THz signal with an optimized, good quality profile and maximize the overlap between THz and sampling beam on detection crystal, correct alignment of the parabolic mirrors is especially required.

The maximized THz light that has correct overlap with sampling beam at the detector crystal increases observed THz electric field, its bandwidth and also dynamic range.[54] In our system alignment of 4th parabolic mirror, which focuses the THz light onto detection crystal, is precisely controlled in order to optimize the signal.

An important part of the system is the detection beam combiner. It is required to transmit most of the THz and reflect a little amount of sampling light onto detector crystal. Figure 2.21 compares the results of two separate materials functioning as beam combiner, mylar (type of polyester) and TPX (polymethylpentene). Mylar is generally preferred because of its highly transmissive nature at THz frequencies. However, handling is difficult since it is very thin, in the µm range, so it is affected from air flow leading to increase in noise. On the other side, TPX gives better results in terms of both increased electric field amplitude (Fig. 2.21 (a)) of THz signal and also transmission of higher THz frequencies (Fig. 2.21 (b)).

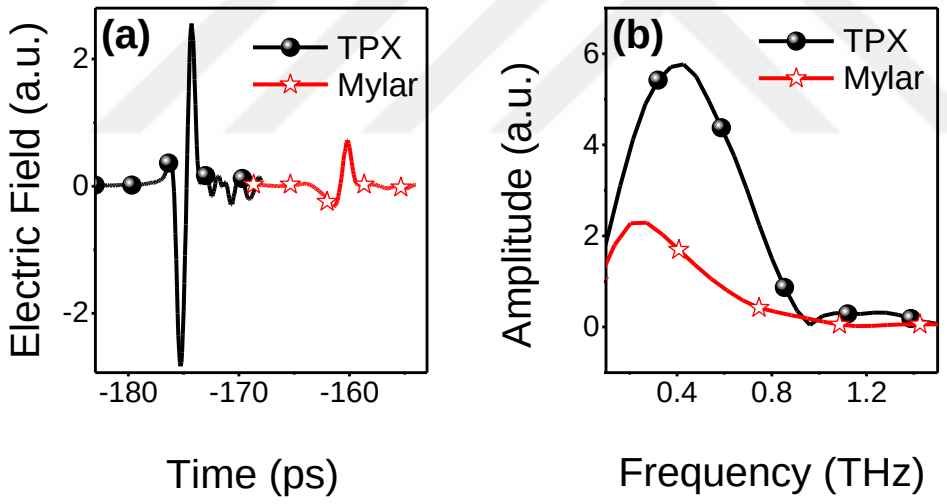

Figure 2.21. (a) Time domain, (b) Frequency domain comparison of Mylar and TPX as beam combiner.

Finally, wedge TPX beam combiner was preferred since it was not possible to separate reflected beam coming from back surface of plate TPX. With wedge TPX, spatial overlap of sampling light and its reflection on detection crystal was prevented.

Parameters of lock-in amplifier also play a part in optimizing observed THz signal. In the measurements, Stanford Research SR830 model is employed which has a sensitivity range between 2nV and 1V with a frequency response up to 100 kHz. Time constant of lock-in, which is optimized as 300 ms in our measurements, is significant to provide high SNR and bandwidth. if time constant is too long or stage velocity is too fast, high frequencies are not detectable resulting in a limited THz bandwidth.[59]

Lock-in is able to measure the THz signal with the modulation comes from the optical chopper. Therefore, frequency and phase of the chopper has a high impact on the detected signal. Generally, multiple of 50 Hz, which is described as electromagnetic pollution, is not preferred to reduce the line noise effect on the obtained signal. Another important aspect is to choose a frequency for chopper which is as different as possible from the reference signal, 1 kHz, to decrease the noise effect.

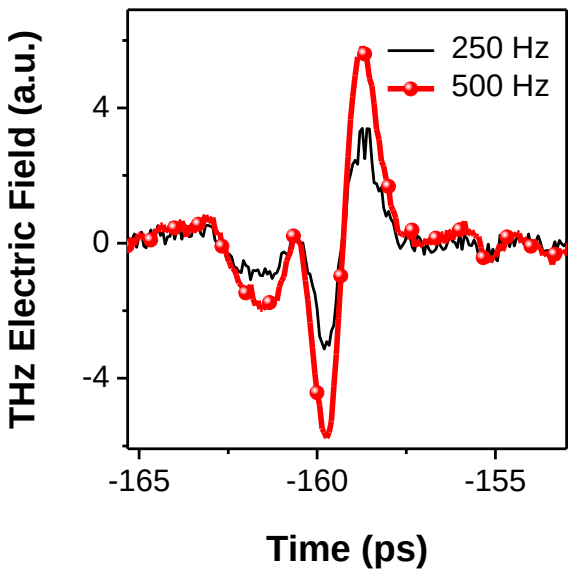

Figure 2.22. The time domain data collected with a modulation setting of 250 and 500 Hz.

Chopping frequency is limited by the disc radius and the size of the beam. Therefore, in order to be able to obtain smaller beam size for effective chopping, we placed our chopper after generation crystal close to the focal point of generation lens. Then, we checked the performance of the chopper with an oscilloscope to ensure the clarity of chopped signal. However, due to size of the beam, chopper was not able to clearly block the beam with 250 Hz, which is also indicated by Fig. 2. 22. Therefore, we decided on 500 Hz as chopper frequency.

Optimization of nonlinear crystal used in the detection of THz beam is also crucial. Broad bandwidth can be provided with a crystal that is sufficiently transparent to THz, and has small velocity mismatch with optical frequencies. In our systems, ZnTe was chosen due to its high performance, and two separate crystals with 0.5 mm and 1 mm thickness values were compared. As Figure 2.23 (a) and (b) show, the thinner crystal allows for an increased THz bandwidth but with lower sensitivity of amplitude of observed signal measured as 1.1 mV. On the other hand, even though 1 mm crystal provides a peak electric field of 1.86 mV, it has a narrower bandwidth at high frequencies. Therefore, we continued our studies with 0.5 mm crystal.

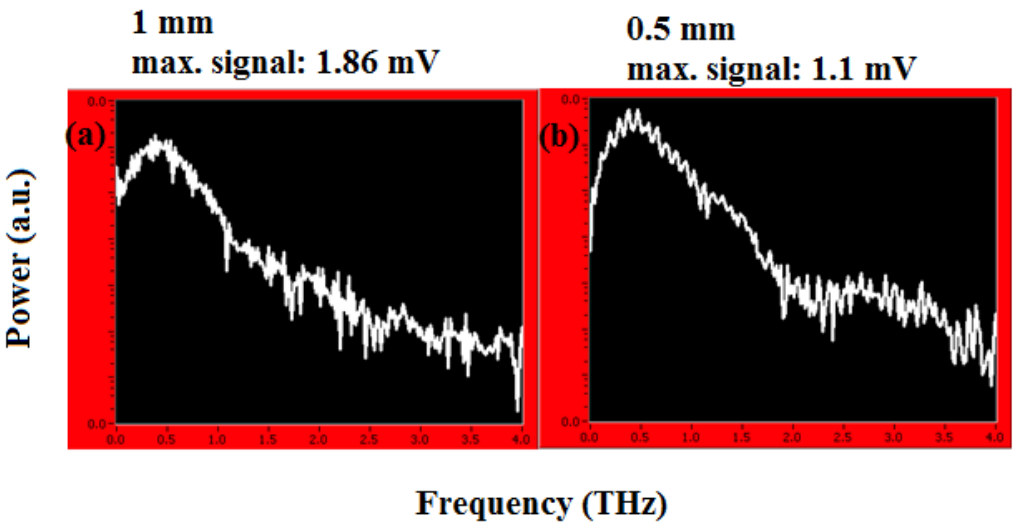

Figure 2.23. THz bandwidth of ZnTe crystal (a) 1 mm, (b) 0.5 mm.

Observed qualities of THz profile mostly depend on the stability and duration of laser pulses. Spitfire amplifier laser produces 1 kHz pulses with approximately 150 fs duration. Duration of the pulses can be optimized with the usage of software program that can control the compressor.

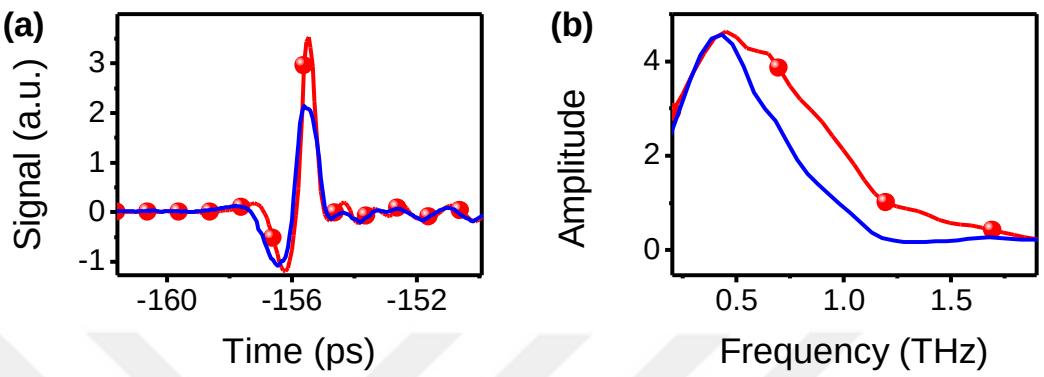

Figure 2.24. Change in **(**a) THz profile (b) Bandwidth, with compressor settings.

When the pulses are narrower, amplitude of THz profile is improved in the time domain (Fig. 2.24 (a)). Moreover, its corresponding frequency data indicate the enhanced bandwidth (Fig. 2.23 (b)).

2.5 Conclusion

In this chapter, construction of two THz spectrometer systems which are THz-TDS and TRTS has been discussed. Studies were started with building THz-TDS system with antenna generation in order to get experience on working with lasers. After that system was built with crystal generation and detection technique. Data collection and analysis were discussed in detail and optical constant calculations were explained. The THz-TDS system was characterized successfully with comparison of literature values of benzene absorption coefficient and refractive index to experimental results. The studies continued with construction of TRTS, with the addition of third arm as optical pump arm. Optical pump source was again Spitfire amplifier laser. After that, data collection and analysis were discussed. Two measurement techniques of TRTS

were mentioned, 1D and 2D. With 1D experiments, dynamic time evolution of the photoinduced THz conductivity of the sample can be extracted since the change of the differential transmission of THz probe signal is directly related to it. Furthermore, 2D measurements allow for extraction of frequency dependent far IR complex conductivity with the application of conductivity models.

Finally, optimization studies were explained. Since achievable frequency resolution depends on the SNR of the system, its improvement is significant for extracting meaningful results from the collected data. Therefore, careful alignment, performance of the mechanical components and laser stability must be assured to balance the inherent aspects of the system performance and achieve a better dynamic range.

CHAPTER 3

GRAPHENE THz MODULATORS

3.1 Introduction

Carbon is a very significant molecule for organic chemistry. With its flexible bond structure, carbon enables unlimited amount of different structures with a large scale of physical properties which are greatly affected by dimensionality of structures. Graphene is a two dimensional (2D) allotrope of tightly packed carbon atoms in a honeycomb lattice and it is the basis of 0 dimensional fullerenes, 1 dimensional nanotubes, and 3 dimensional graphite (Fig. 3.1).[60]

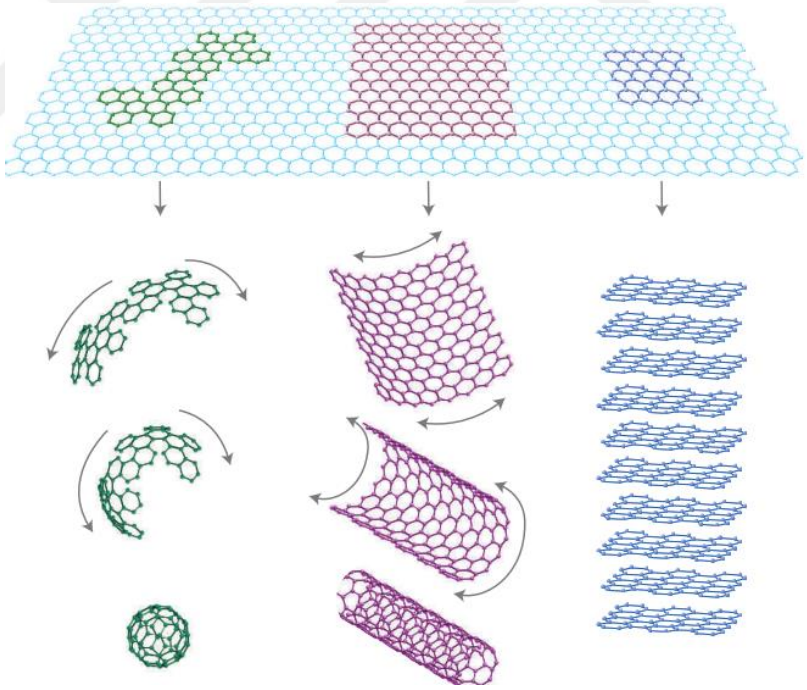

Figure 3.1. Graphene forms the basis of all graphitic materials: fullerenes, nanotubes and bulk graphite.[60]

Since its discovery in 2004, graphene, the simplest complex material[61], has attracted intense attention in many fundamental areas due to its remarkable electronic and mechanical properties.[62] Consequently, in 2010, Andre Geim and Konstantin Novoselov were awarded with Nobel prize for their "ground breaking experiments regarding the two-dimensional material, graphene.[63]

Although, graphene is the basic building block of all allotropes and most likely is even produced when someone presses a pencil against a paper, its isolation took hundreds of years.[64] Until its discovery, it was believed that planar graphene could only exist theoretically and could not be free due to thermal instability of 2D materials in ambient conditions.[60] This claim was derived from experimental observations that revealed melting point decrease with decreasing film thickness. As a result, thin films especially with a thickness of dozens of atomic layers became unstable at room temperature.[65] For this reason, 2D atomic monolayers were only thought to be part of larger 3D structures. This thought was disregarded in 2004 when it was proved that a stable form of graphene film was isolated under ambient conditions by its observation with an ordinary optical microscope.[66]

3.1.1 Band Structure and Electronic Properties of Graphene

Band gap describes the energy difference between valance and conduction band, and it is one of the major components in defining material's properties. Fermi level indicates the middle point of band gap energy.

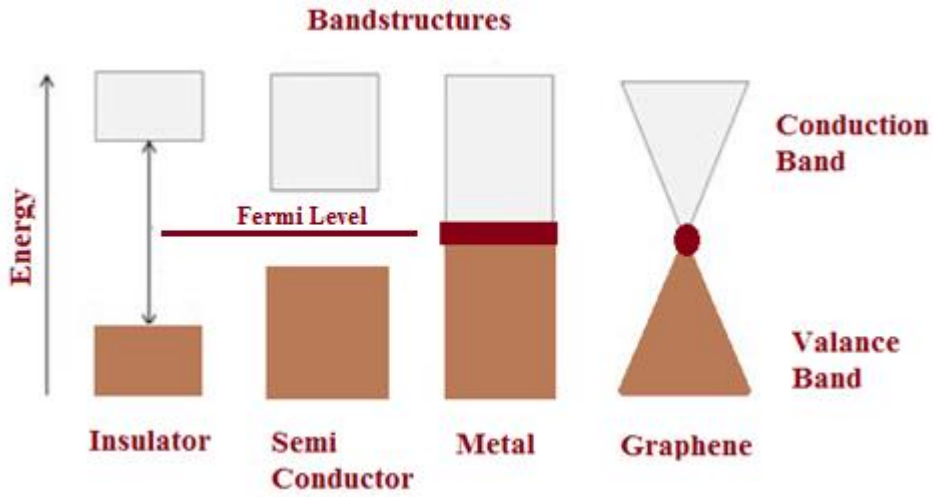

Figure 3.2. The band structures and energy gaps of insulator, semiconductor, metal and graphene. The claret red colors indicate the Fermi levels in different materials.

As Figure 3. 2 indicates, materials with high band gap energies are characterized as insulators, while materials with smaller band gaps are semiconductors. On the other side, metals (conductors) do not have band gaps (overlapping Fermi level with both band).

Graphene is a typical 2D material with Dirac cones.[67] It is characterized as zero-gap semiconductor, or zero-overlap semimetal with identical hole and electron mobility. Graphene's gapless nature and symmetrical band structure come from Dirac cones, which provide it with novel physical and electronic properties. This band structure provides an environment for carriers to behave such as they were massless, Dirac fermions. The unique nature of these carriers results in a ballistic transport at room temperature [60], and only be described with a relativistic approach rather than classical Schrödinger equation[68]. Therefore, graphene acts as a bridge between condensed matter physics and quantum field theory. Furthermore, another incredible property of graphene is its ideal conductivity with no scattering process, which is in the order of e^2/h. This finite, frequency independent conductivity reflects ideality of graphene crystals.[68]

3.1.2 Graphene Applications

Graphene has extraordinary physical properties such as room-temperature quantum Hall effect and micrometer long mean free path.[69,70] Its massless carriers, Dirac fermions, give rise to an extremely high carrier mobility exceeding 200000 $cm^2/V \cdot s$ [71] making graphene a unique material in applications of high speed electronics. Moreover, 2D nature of graphene enables it to be produced easily by existing thin film technologies. As a result, it can be made compatible with current Si technologies[72] creating a new photonic platform for further development of optoelectronic devices such as light-emitting diode (LED) and high quantum capacitors.[73] Graphene's fairly low (ca. %2.3) absorption of visible and IR radiation[74] makes it utilizable in the application of photodetectors, broadband infrared electro-optical modulators[75]. Furthermore, graphene is a great transparent conductor, alternative to semiconductors and ITO with its superior electronic properties, flexibility and abundancy.[76]

Graphene is a high potential candidate for post silicon electronics due to its both nano dimensions and high electrical conductivity compared to Si. It is expected to facilitate transistor downscaling with increase in switching speeds. However, implementation of graphene in transistor technology with efficient on/off current is hindered by its zero band gap energy. Although there are several attempts for creating band gap in graphene, they are not feasible yet.[77] Consequently, there is still a long way for graphene to replace Si in electronics.

Exploration of graphene carrier dynamics has shown that electronic structure of graphene is more sensitive to the THz region of the electromagnetic spectrum rather than IR and optical range.[78] Carrier scattering rates in graphene is in the order of several THz. Therefore, THz optical conductivity and electronic conductivity of graphene are equivalent. THz beams allow characterization of carrier dynamics near the Fermi level.[79,80] Therefore, graphene is recognized as a potentially active material for photosensitive THz devices in the application of active filters, switches, and modulators. These optical devices are urgently needed by THz technology in order to

advance a diverse range of applications such as nondestructive imaging,[81,82] spectroscopy,[83] biomedical diagnosis,[84] ultrahigh wireless communication,[40] and security.[43]

3.1.3 Introduction to Graphene THz Modulators

Conventional THz modulators that are based on semiconductor materials[85] and hetero-structure containing 2D electron gas[86] showed low modulation depths. Metal gates used in the structures can limit the working range of carrier density and Fermi energy tuning.[87] Compared to those, single layer graphene based THz modulators have higher carrier mobility with an electrically tunable carrier density and offer very low insertion loss (0.2-0.5dB).[88,89] However, theoretically expected high modulation depth and broadband performance is difficult to achieve due to its strong dependence on quality of graphene [89] and unforeseen component effects of the devices such as substrate effects [90]. In order to improve THz modulation by single layer graphene different methods such as integrating graphene with photonic cavities [91] and metamaterials [92,93] have been reported. In their study Kakenov et al. have demonstrated a flexible active THz surface constructed with a large-area single graphene layer, a metallic reflective electrode, and an electrolytic medium in between that provides complete modulation in the THz reflectivity at 2.8 THz. [91] 50% amplitude modulation at low voltages is reported by Gao et al using a gated single-layer graphene modulator with metallic ring aperture.[94] However, the modulation is limited to a quite narrow bandwidth.

Increased modulation depth can be obtained by use of multilayer graphene (MLG) alone or MLG with ionic liquids.[81,95–99] Shen et al. presented a metamaterial based modulator with a multilayer stack of alternating patterned graphene sheets with 75% modulation depth.[93] However, the narrowband operational range and polarization dependent response of metamaterial based modulator may limit their future applications.[100] In their study, Baek et al. has shown improvement in THz modulation with production of high quality MLG.[97] In that study the optical sheet conductivity increase has also been demonstrated as the layer number increase from 1 to 12. The

dielectric substrates can cause change in the fermi level of a single layer graphene due to band gap opening and this situation could mislead optical results.[101] Whereas in MLG, optical response is dominated by the layers that do not interact with substrate. In their study Wu et al. investigated a graphene/ionic liquid/graphene device where ionic liquid forms interfaces with the graphene electrodes.[96] As the layer number of the graphene electrodes increased an increased modulation is observed, which is explained by elimination of boundary defects during multilayer formation. Kakenov et al. presented another ionic liquid based THz amplitude modulator.[102] Due to efficient mutual gating of graphene electrodes and ionic liquid, more than 50 % modulation depth was obtained. Furthermore, Liu et al. used ionic liquid in their THz modulator device and achieved a modulation depth of 22 %.[103] In this study, high flexibility of THz modulator has been demonstrated by the great flexibility of graphene, ionic gel and also the host material, polyethylene terephthalate.

A compromise between modulation depth, polarization dependence, ease of fabrication, design flexibility, large area production, and operational bandwidth exist in most of the studies reported in literature. This chapter presents large area MLG devices on flexible substrates that do not compromise on the modulation performance. The study experimentally demonstrates an excellent performance on THz amplitude modulation by devices made from ionic liquid doped MLG structures on Polyvinyl chloride (PVC) and Polyethylene (PE) substrates. The modulation depths were investigated at a broadband frequency range from 0.2 to 1.5 THz with application of very low voltages ranging between 0 V and 3.4 V. To our knowledge, this is one of the highest modulation depth achieved at a broad THz range and such low gate voltages. This performance is achieved due to unique structure of MLG THz modulators, which enhances the gating effect of ionic liquid tremendously.

3.2 Experimental

Experimental studies for SLG and MLG modulators were done by using THz-TDS system, which was described in Chapter 2.

3.2.1 Sample Preparation and Characterization

Samples were prepared by using chemical vapor deposition (CVD) method. CVD is a commonly used technique in the production of high quality, large scale films with good electrical and optical properties. Moreover, production of films with large area is especially important, since spot size of THz is generally bigger than three millimeters.[104] Single layer graphene (SLG) samples were grown on the cupper foils and multilayer graphene (MLG) samples were grown on the nickel foils. It is difficult to synthesize more than twenty layers with cupper foils. Therefore, nickel foils are both preferred for higher layer number and also samples with less defects.[105]

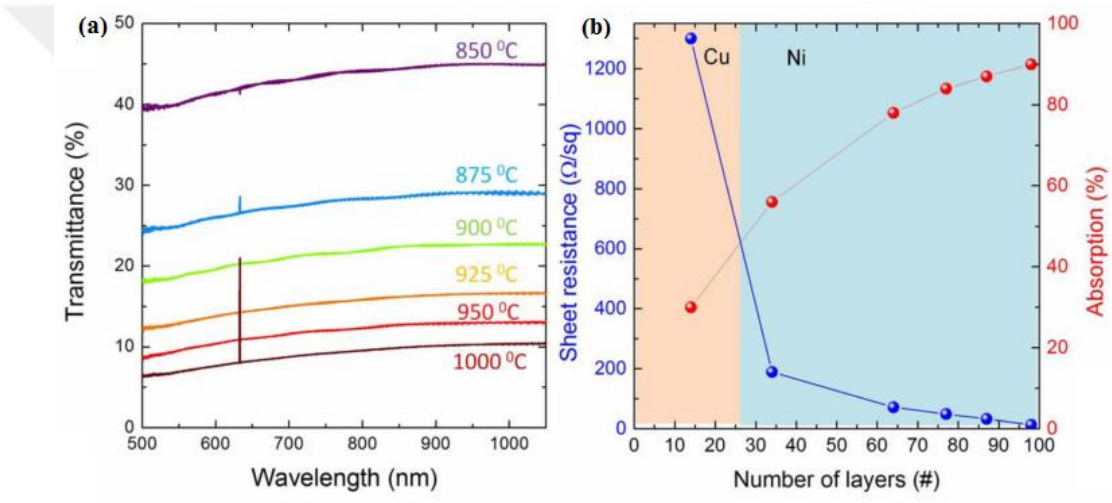

Figure 3.3. (a) Optical transmittance spectra of the MLG electrodes at different temperatures, (b) Variation of the sheet resistance (blue curve) and optical absorption (red curve) of MLG electrodes with the layer number.[106]

The growth process takes place in quartz chamber at the presence of argon, hydrogen and methane gases. The temperature in the chamber and growth time determine the layer number of synthesized graphene samples. Our MLG samples were grown at 850 °C, 900 °C and 1000 °C corresponding to nearly 30, 60 and 100 layers, respectively. The layer numbers are estimated from optical transmittance spectra and sheet resistance measurements.[106] Change in optical transmittance with increasing layer

number at different temperatures can be seen in Fig.3.3 (a). Variation of the sheet resistance (blue curve) and optical absorption (red curve) of MLG electrodes with the layer number is given in Fig. 3.3 (b).

After the growth, SLG and MLG samples with 30, 60 and 100 layers were moved on PVC and labelled as MLG850, MLG900 and MLG1000 and 100 layers on PE as MLG1000PE by lamination (Fig. 3.4 (a)), and nickel or cupper was removed with iron chloride ($FeCl_3.6H_2O$) solution (Fig. 3.4 (b)).

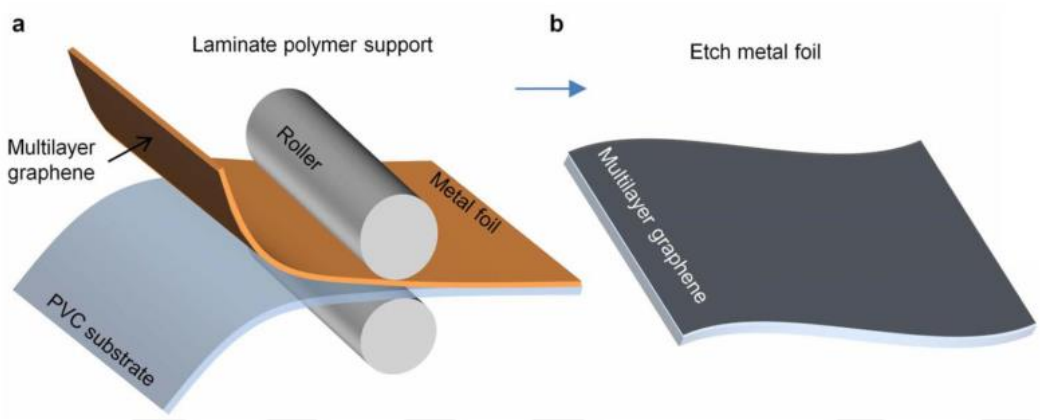

Figure 3.4. (a) Transfer printing of large area multilayer graphene on flexible PVC substrates by lamination process, (b) Etching the metal foils yields flexible multilayer graphene electrodes on the PVC support.[106]

3.2.2 Device Fabrication

Inset of Figure 3.5 (a) demonstrates fabricated SLG and MLG structure. The device consists of SLG or MLG and gold electrodes sandwiching ionic liquid [DEME][Tf2N] (Diethylmethyl(2-methoxyethyl)ammoniumbis(trifluoromethyl sulfonyl)imide) in between. Electrochemical window and high THz transmittance value of the employed ionic liquid are key factors to accomplish an effective

modulation. [DEME][Tf2N] demonstrates a remarkable performance, which has an electrochemical window between -3.0 to 3.5 V.

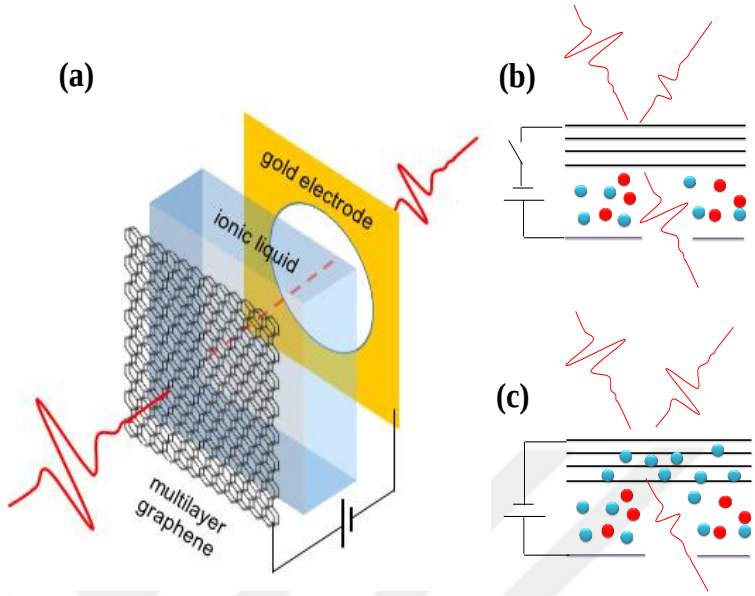

Figure 3.5. (a) A schematic of the SLG or MLG structure consisting of graphene, electrolyte medium, and gold electrode. Drawings showing (b) No doping case at zero applied voltage and (c) Intercalation of ions through the graphene layers by gating.

The whole structure is supported by the polymer substrate (not shown for clarity) on SLG or MLG electrode side, and the gold electrode has a circular opening of 5 mm through which THz transmittance was measured. At zero bias, the transmittance through MLG devices are maximum (Fig. 3.5 (b)) suggesting very low doping level, if any. Upon application of bias voltage, the ions of the same polarity intercalate [106,107] through layers of graphene by inducing charge carriers in layers of graphene resulting in attenuation of THz transmission (Fig. 3.5 (c)). Intercalation process is achieved due to weak inter layer coupling and very strong intra layer bonding between graphene layers. [98]

3.2.3 THz Measurements of SLG Modulators

After construction of SLG modulator (Figure 3.6 (a)), they were characterized with THz-TDS. Our home-made THz-TDS system have an effective bandwidth of 0.2 to 1.2 THz with SLG modulator. A 500 µm <110> ZnTe crystal is used to generate coherent THz radiation via optical rectification. Through the Pockell's effect, phase of the detection pulse is retarded by the oscillating electric field of the THz radiation. Change in the polarization is monitored by quarter wave plate and Wollaston prism. Voltage from the balanced photodetector is synchronously detected using a lock-in amplifier. Specifications of the system is given in Chapter 2.2.

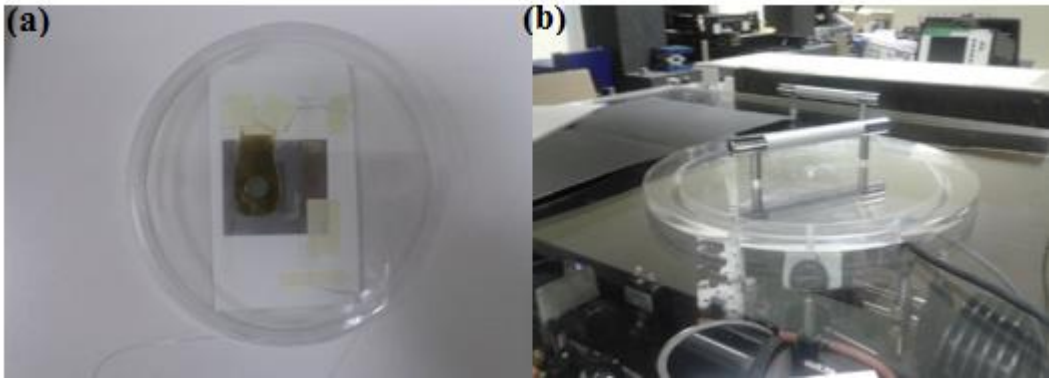

Figure 3.6 (a) SLG Modulator, (b) Position of sample in the THz-TDS System.

SLG modulator was positioned on an iris as sample holder and placed at the focal point of parabolic mirrors where THz spot size was approximately 5 mm (Fig. 3.6 (b)). Sample size was arranged as 5 mm also for a homogenous measurement. Tens of measurements were done with different devices to evaluate the repeatability and reliability of results. Measurements were done in a temperature and humidity controlled environment (20 ± 0.5 °C, 1 % Humidity). Scan length was restricted to 10 ps in order not to include crystal reflection (echo pulse) in the measured time window. Step size was chosen as 10 µm for high resolution.

A DC voltage was applied with a Keithley 2400 power source through Au and graphene electrodes. Voltage was gradually increased from 0 to 3.2 V. Measurements were taken at 0, 0.5, 1, 2, 2.6, 3 and 3.2 V. After 3.2 V, current values increased drastically indicating that device was damaged. System stability was controlled with air THz profile reference measurements which were taken before and after modulator measurements. Voltage dependent THz time domain profiles of SLG are given in Fig. 3.7.

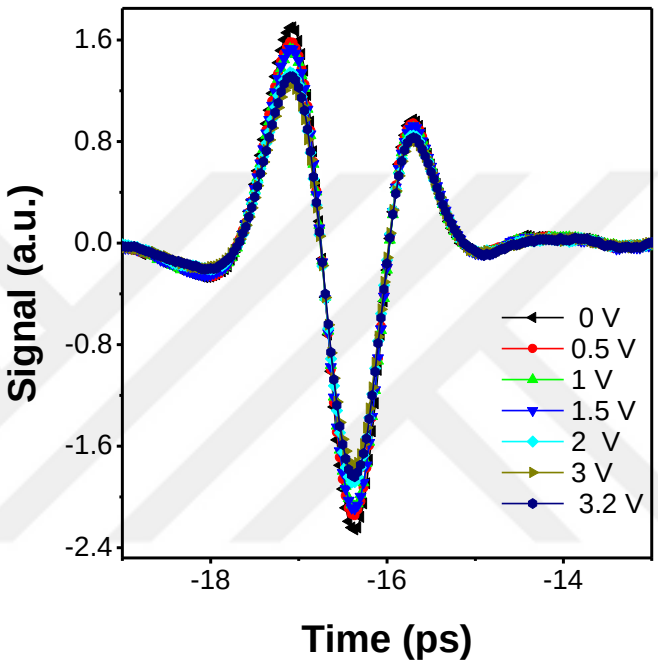

Figure 3.7. Voltage dependent THz time domain profiles of SLG.

3.2.4 THz Measurements of MLG Modulators

After construction of MLG850, MLG900, MLG1000 and MLG1000PE modulator devices, they were characterized with THz-TDS under same experimental conditions of SLG modulators. THz-TDS system have an effective bandwidth of 0.2 to 1.5 THz with MLG modulators. In order to ensure reliability of thickness dependent modulation behavior, several measurements were taken with new devices under same

conditions. As voltage values: 0, 0.5, 1, 1.5, 2, 2.6, 3, 3.2, and 3.4 were chosen. Voltage dependent THz time domain profiles of modulators are given in Fig. 3.8.

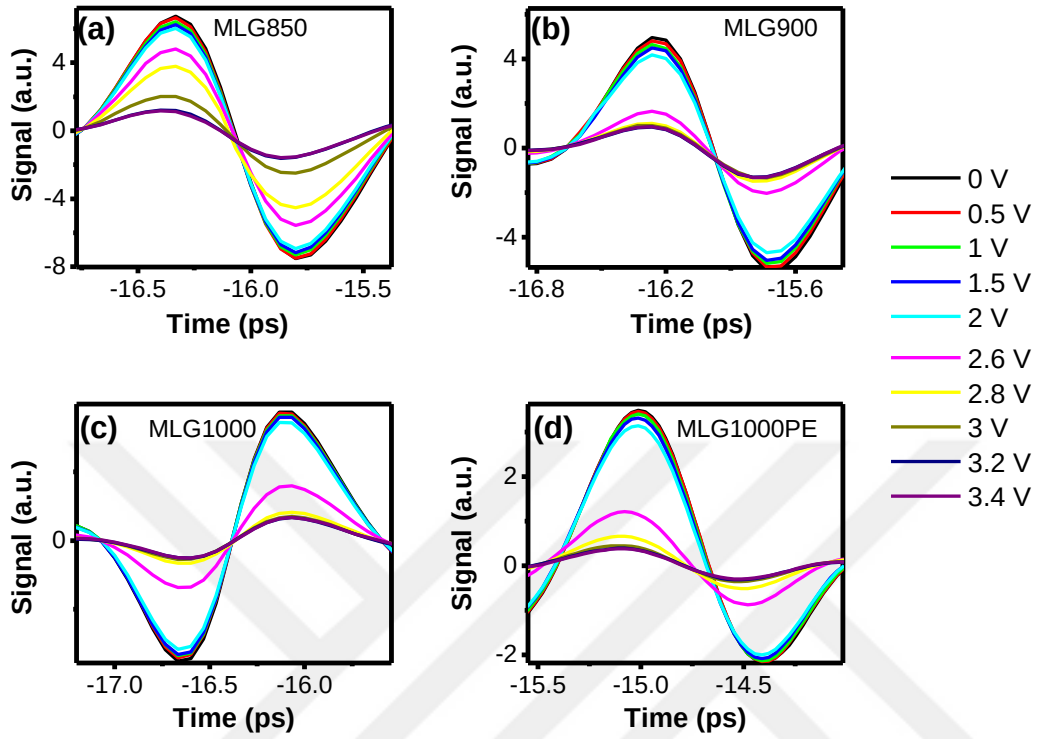

Figure 3.8. Voltage dependent THz time domain profiles for (a) MLG850, (b) MLG900, (c) MLG1000 and (d) MLG1000PE.

3.3 Results and Discussion

Figure 3.9 (a) presents change in terahertz waveforms around the peak amplitude for SLG with the applied gate voltage. The inset of Fig. 3.9 (a) presents a full profile at 0 V as an example. Corresponding frequency domain data of the device is given in Fig. 3.9 (b). No observed change in phase might be because of graphene's robust nature under electrolyte gating[96] and having a thickness much less than the THz wavelength.

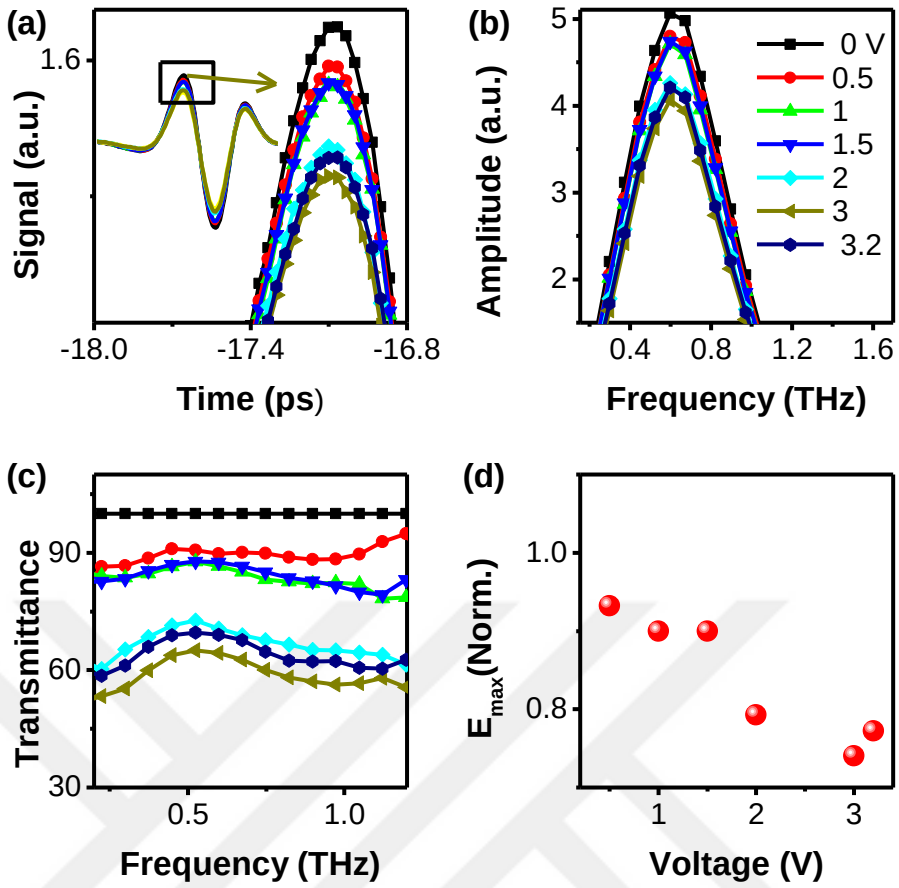

Figure 3.9. (a) Voltage dependent THz field near peak amplitude of SLG. (Inset: Example of time domain THz profile), (b) Corresponding frequency domain amplitudes, (c)THz transmittance of SLG Modulator at all applied voltages, d) Modulation with voltage at THz peak amplitude.

In Figure 3.9 (c) THz transmission of SLG modulator is given between 0.2 THz and 1.2 THz. Up to 1.5 V less than 20 % modulation was observed and nearly 30 % modulation was achieved at around 2 V. Almost 50 % modulation was observed at voltages beyond 3 V, and 3.2 V was the damage threshold for our device. This is a quite promising result for a SLG modulator. Figure 3.9 (d) shows change in THz peak amplitude of SLG device as bias voltage was varied from 0 V to 3.2 V. The maximum transmission was at 0 V while the minimum was reached around 3 V. As the gate voltage increased almost linear decrease in amplitude was observed up to ca. 1.5 V.

After that, a sharp nonlinear decrease with the voltage was observed. Approximately 2 V appeared to be turning point where the decrease slowed down. The observed change in THz amplitude is provided with voltage controlled change in mobile carrier density.

Figure 3.10 (a) presents change in terahertz waveforms around the peak amplitude for MLG850 as the applied gate voltage is increased. The inset of Fig. 3.10 (a) presents a full profile at 0 V as an example. Corresponding frequency domain data of the device is given in Fig. 3.10 (b). No observed change in phase might be because of graphene's robust nature under electrolyte gating[96] and having a thickness much less than the THz wavelength.

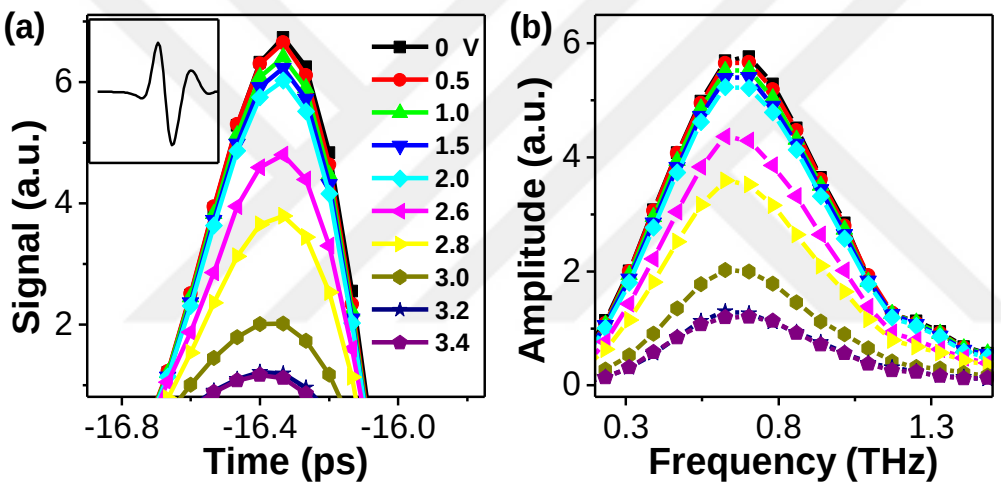

Figure 3.10. (a) Voltage dependent THz field near peak amplitude of MLG850. (Inset: Example of time domain THz profile) (b) Corresponding frequency domain amplitudes.

Figure 3. 11 illustrates frequency domain data for other devices, which again had no indication of phase shift.

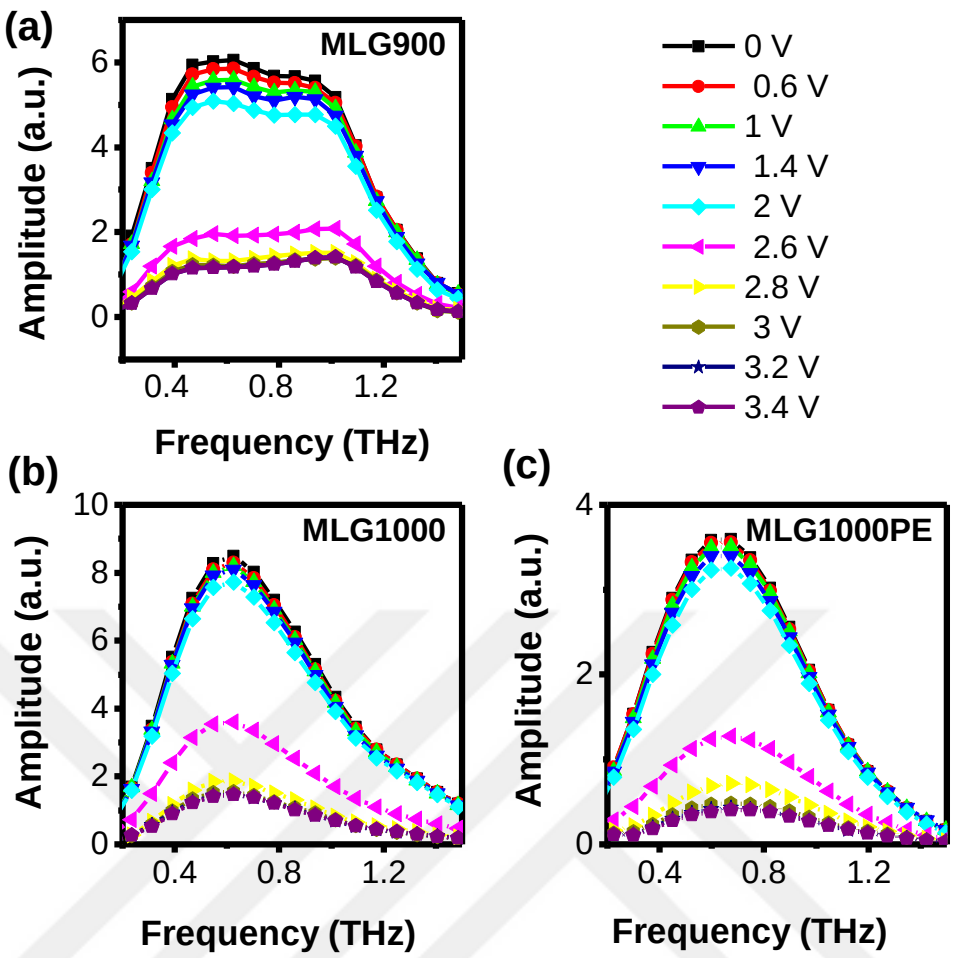

Figure 3.11. Frequency domain amplitudes from 0.2 THz to 1.5 THz frequency range for (a) MLG900, (b) MLG1000, (c) MLG1000PE

In Figure 3.12 (a) THz transmission of MLG850 is given between 0.2 THz and 1.5 THz. Up to 1.5 V less than 20 % modulation was observed. A modulation between 20 and 30% at ca. 2 V can be achieved depending on the MLG thickness (Fig. 3.12 (a-d)). While the thinnest layer showed the lowest modulation at 2.6 V as approximately 50%, the remaining MLG devices had more than 80% modulation already. Almost full power modulation had been achieved with all MLG devices at voltages beyond 3 V. The modulation depth is significantly improved compared to single[78] and multilayer[97] devices over a very broad range. Among all devices MLG850 provided a more controllable modulation.

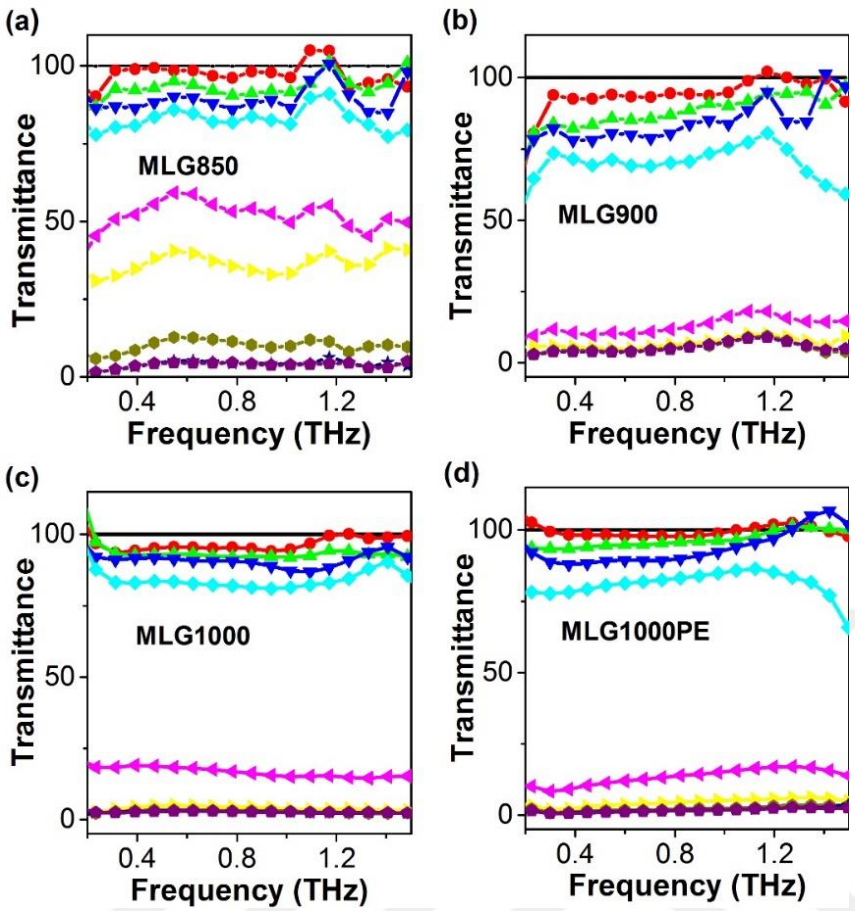

Figure 3.12. THz transmittance of (a) MLG850, (b) MLG900, (c) MLG1000 and (d) MLG1000PE at all applied voltages relative to 0 V.

Figure 3.13 (a) shows change in THz peak amplitude of all four devices as bias voltage was varied from 0 V to 3.4 V. The maximum transmission was at 0 V while the minimum is reached beyond 3 V. As the gate voltage increased almost linear decrease in amplitude was observed up to ca. 2 V. After that, a sharp nonlinear decrease with the voltage was observed. Approximately 2.5 V appeared to be the turning point where the decrease slowed down. The observed change in THz amplitude is provided with voltage controlled change in mobile carrier density. The voltage dependent behavior of the MLG devices is very similar to each other except the thinnest device which requires slightly higher voltage (ca. 0.5 V).

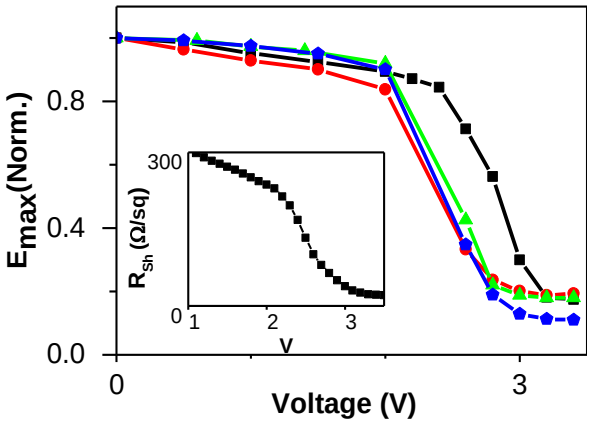

Figure 3.13. (a) Modulation with voltage at THz peak amplitude (MLG850 black square; MLG900 red circle; MLG1000 green triangle; MLG1000PE blue pentagon). (Inset: Voltage dependent sheet resistance of MLG850 measured by four probe.

Four probe measurement of voltage dependent sheet resistance behavior of MLG850 is given in inset of Fig.3.13 (a) and shows a very similar behavior. The observed modulation with the set voltage appears to be independent of the THz frequency (Fig. 3.14) and, thus, limited by the instrument response.

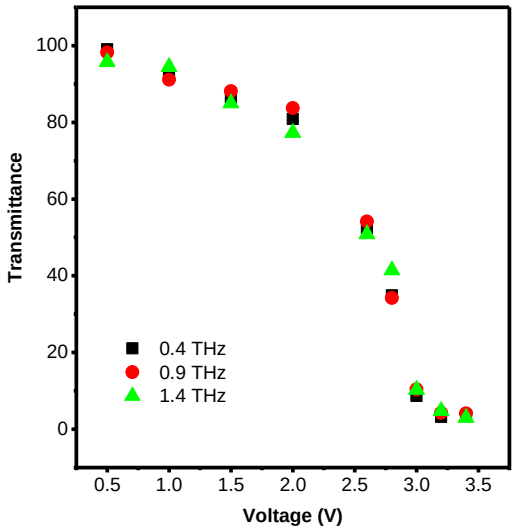

Figure 3.14. Transmittance of MLG850 device at all applied voltages relative to 0 V for three selected frequencies of 0.4, 0.9 and 1.4 THz.

Optical conductivity of graphene appears to follow its electrical conductivity at the THz frequencies and, thus, follows the Drude model.[80,108] All the changes observed in conductivity is expected to be due to a change in carrier density and/or change in scattering time[109]. Therefore, THz sheet conductivities (σ_{sh}) of MLG devices is proportional to the amplitude ratio of reference (PVC or PE) substrate to MLG sample as given in equation 3.1.[110]

$$\boldsymbol{\sigma_{sh} = (n+1)\left(\frac{A_{subsrate}}{A_{MLG}} - 1\right)/Z_0} \qquad \textbf{(3.1)}$$

Here, Z_0 is free-space impedance, and n is substrate refractive index. The sheet conductivities of MLG850 are given in Fig. 3.15 (a). At the Dirac point all devices show featureless sheet conductivities.

DC conductivities of devices MLG850, MLG900, MLG1000 and MLG1000PE are derived to be 4.4 mS, 7.5 mS, 17.8 mS and 10.3 mS, respectively. Device with PE substrate appears to be lower than PVC counterpart. Conductivity difference is most likely due to quality of the graphene[110] since it will affect scattering time of the carriers. The DC conductivities determined from extrapolation of THz ones are close to the ones determined from four probe measurements (3.3 mS for MLG850, 5.8 mS for MLG900, 31.2 mS for MLG1000) and are consistent with the ones reported for the similar devices[97,110,111].

Table 3. 1. Comparison of THz-TDS and Four Probe experimental results.

	THz-TDS (mS)	**Four Probe (mS)**
MLG850	4.4	3.3
MLG900	7.5	5.8
MLG1000	17.8	31.2

Observed difference between THz-TDS and Four Probe measurements can mainly stem from presence of contacts in the latter. It is difficult to implement probe contact

measurements particularly when sample is a thin film that can be damaged at the contact location.[112] In four probe, conductivity is measured at micrometer scale due to dimensions of mechanical probes which can be accepted as DC transport. Whereas THz-TDS provides non-contact AC transport in nanometer scale.[113]

Estimated carrier densities are ca. 1.5×10^{12} cm^{-2} for MLG850, ca. 4.5×10^{12} cm^{-2} for MLG900, and ca. 1.3×10^{14} cm^{-2} for MLG1000 using experimental sheet resistance values and an average value of 200 fs[114] for scattering time. Sheet conductivities (σ_{sh}) at applied voltages are calculated using equation 3.2, which is derived from equation 1.[115]

$$\boldsymbol{\sigma_{sh} = \frac{n+1}{Z_0}\left[\frac{A_0}{A_{gate}}\left(1 + \sigma_{sh,0}\frac{Z_0}{n+1}\right) - 1\right]} \qquad \textbf{(3.2)}$$

where A_0 and A_{gate} is transmitted THz field amplitude of MLG device at 0 V and gate voltage, respectively. The results are given in Fig. 3.15 for all devices.

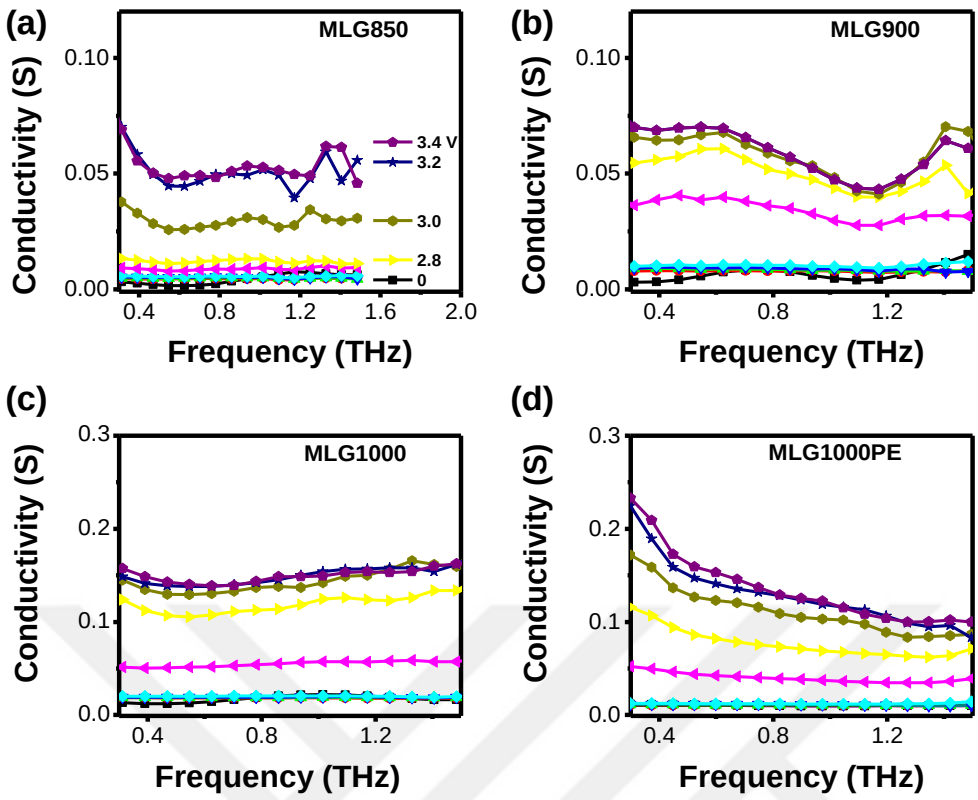

Figure 3.15. THz sheet conductivity of devices at all applied voltages. (a) MLG850, (b) MLG900, (c) MLG1000 (d) MLG1000PE.

Figure 3.16 presents conductivities at representative voltages of 1.5 V, 2.8 V and 3.4 V at 0.8 THz.

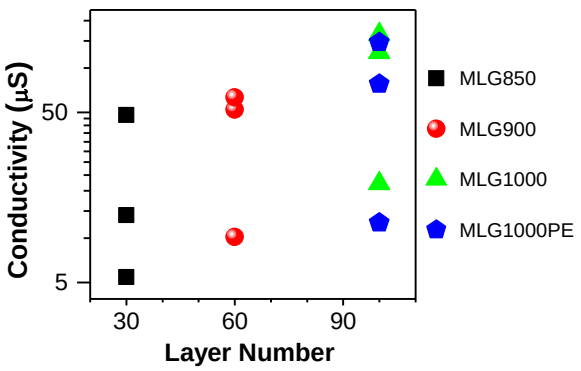

Figure 3.16. THz sheet conductivities of MLG devices at 0.8 THz for selected voltages of 1.5 V, 2.8 V, and 3.4 V.

The conductivities increase significantly with doping at 3.4 V relative to 0 V [$(\sigma_{3.4V}-\sigma_{0V})/\sigma_{0V}$] amounting to ca. 1000% for MLG850, 715% for MLG900, 705% for MLG1000, and 1150% for MLG1000PE (Table 3.2). A similar observation is explained by an increase in hole carrier concentration.[109]

Table 3. 2. Effect of doping on conductivity.

	Doping Effect %
MLG850	1000
MLG900	715
MLG1000	705
MLG1000PE	1150

Besides doping effect, graphene thickness can also affect the conductivity drastically. When the thinnest (ca. 30 layers) and the thickest (ca. 100 layers) devices are compared at 0 V [$\Delta\sigma=(\sigma_{1000\,^{\circ}C}-\sigma_{850\,^{\circ}C})/\sigma_{850\,^{\circ}C}$] an enhancement of ca. 300% was observed. The difference is still significant but less pronounced as 197% at 3.4 V for the same devices. Similarly, an increase of 73% in the sheet conductivity was noted as the graphene layer number increased from 1 to 12 in the study by Baek et al. In addition, Wu et al has also shown an increased sheet conductivity with increase in layer number.[116] Increase in layer number should not significantly affect the THz conductivity or carrier momentum scattering time[109] in a layer. Sheet conductivity is defined[109] as $\sigma_{\mathrm{sheet}} = \sigma_{\mathrm{THz}} \times d_{\mathrm{N-layer}}$ where $d_{\mathrm{N-layer}}$ is the thickness of N-layer (N = 30, 60, or 100) graphene and only sheet conductivity is expected to increase due to increased carrier density with thickness.

In addition to being a preferential host material for flexible photonic devices PVC and PE are also preferred for their very low insertion losses; less than 1 dB at all frequencies, which is much less than the devices. The thinnest device had an average of 3 dB insertion loss and the loss is increased with the layer thickness. The highest loss is observed for the thickest devices as ca. 8 dB for MLG100PE and 11 dB for MLG1000 (Fig. 3.17).

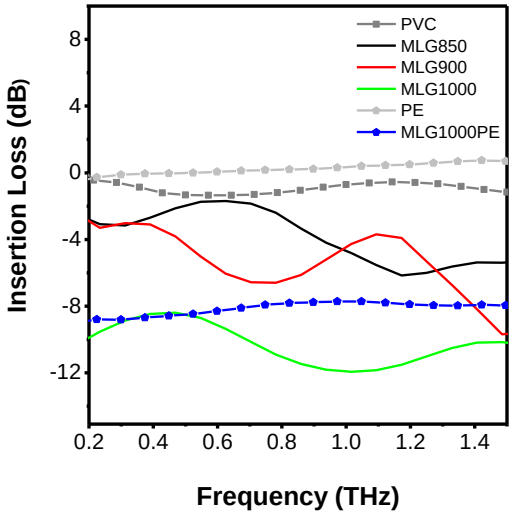

Figure 3.17. Insertion loss of PVC, PE, and the MLG devices grown at 850°C, 900°C and 1000°C.

Figure 3.18 presents modulation of THz amplitude versus the insertion loss at 0.8 THz for selected voltages of 1.5 V, 2.8 V and 3.4 V. Here the insertion loss is the initial loss of the THz power when the device is inserted in the beam path and modulation represents the further change in the transmission of THz wave. Effect of ionic liquid is also included in the insertion losses.

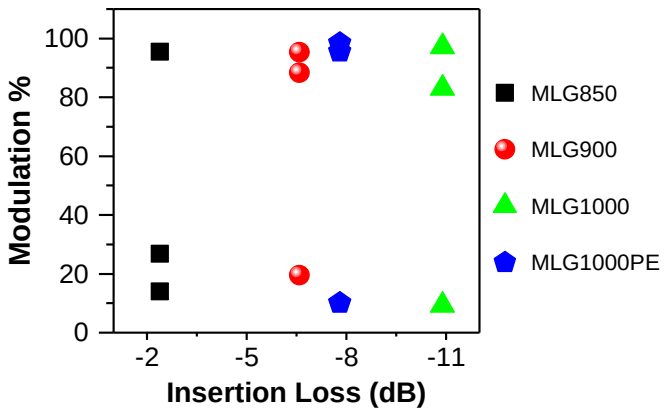

Figure 3.18. Modulation vs insertion loss of MLG devices at 0.8 THz for selected voltages of 1.5 V, 2.8 V, and 3.4 V.

The best performance is achieved with the thinnest MLG device with its much lower insertion loss and almost 100 % modulation depth with an application of 3.4 V. Depending on the application type, devices with optimal numbers of graphene layers can be designed considering the trade-off between modulation and insertion loss at the preferred voltage.

The result of our studies suggest that long recovery times due to slow movement of ions is one of issues that has to be considered. The same limitation has also been observed in the study of Liu at al.[103] Compared to Liu et al.'s 22% modulation depth with SLG device, we achieved 50 % power modulation with our PVC based SLG THz modulator, which is a quite promising result. 93 % power modulation was demonstrated with the utilization of ionic liquid with a three layers graphene THz modulator in the study of Wu et al.[96] Different from our device design, in Wu et al.'s study, ionic liquid was sandwiched between two quartz substrates, which were coated with graphene films. It was suggested that ionic liquid played a significant role for THz modulation since without the interface between ionic liquid and graphene electrodes, almost no change in the amplitude of THz pulse with applied voltage was observed. Similar to that, our modulation mechanisms also depended strongly on ionic liquid, which was intercalated through the graphene layers with applied voltage. Moreover, we achieved full power modulation with our MLG devices easily, which had a wide range of layer numbers. Compared to a three-layer graphene deposited on $SiO_2/Si/SiO_2$ by Chatzakiz et al., which resulted a 15% THz modulation with application of quite high voltage values (20 V), our devices achieved almost complete modulation with application of 3 V only. Chatzakiz et al. pointed out that Si substrate also exhibited considerable THz modulation with applied voltages. Therefore, choosing correct substrates which will not affect the results or will require extra care in the data analysis part is advantageous.

3.4 Conclusion

In this study, broadband modulation behavior of SLG and four different THz devices based on multilayer graphene was investigated by THz time-domain spectroscopy.

SLG device provided approximately 50 % modulation and in order to achieve higher values, MLG based devices were examined. The thinnest device with ca. 30 layers provided almost complete modulation of THz waves at an operation voltage of less than 3.4 V. The effect of increased layer number on THz modulation was also investigated and near complete modulation was demonstrated at all the thicknesses. However, as the layer thickness increased an increase in the insertion loss was also observed. With the strong gating effect of dopant molecules, it was possible to achieve a tunable modulation in THz transmission between 0.2 and 1.5 THz as a broadband response with very low operation voltages from 0 V to 3.4 V. Here, the modulation is frequency independent and bandwidth appears to be limited only by the instrument. Even at such low gate voltages the devices have been doped significantly inducing an enormous improvement in their sheet conductivities. Sheet conductivities of the devices were also improved with increasing thickness of the active layer. Such controlled and targeted behaviors are promising for new THz devices for desired conductivities and modulations. This study along with the previously reported studies have shown that ionic liquid integrated MLG devices are a promising platform to produce THz active filters with controlled modulation and are expected to have a strong impact on THz optoelectronic devices in near future at many application areas.

CHAPTER 4

TERAHERTZ CONDUCTIVITY MEASUREMENTS OF SLG AND MLG

4.1 Introduction

Graphene is an excellent material which has a potential of being used in a diverse range of applications such as, photovoltaics, saturable absorbers, light emitting devices and THz devices.[113] For these applications, large area graphene films that can offer high conductivity values, mechanical strength and optical properties are required. Accordingly, a great progress in fabrication methods for this large area graphene films have been achieved.[117] However, the same progress has not been shown in electrical characterization of graphene thin films. A detailed knowledge and precise measurement results of frequency dependent conductivity is vital for being able to design advanced electronic components. Usually, contact based techniques such as four probe are employed in the characterization of current-voltage response of graphene films.[118] Nevertheless, Ohmic contacts can create artefacts on nanosized materials during fabrication. This kind of damage may lead to false results and prevent reliable multiple measurements of the same sample. Therefore, a noncontact and nondestructive measurement technique is required.

Terahertz time domain spectroscopy appears to be one of ideal tools for noncontact and nondestructive conductivity measurements. Due to the broad bandwidth of THz pulses and their matchable nature to typical carrier scattering rates, it is possible to characterize complex conductivity of semiconductors.[27] THz-TDS has already proved itself to be a powerful technique in the measurement of graphene complex sheet conductivity.[61, 80,119] By employing THz-TDS in graphene conductivity measurements, large scale, position based information is provided. By this way, it is possible to map out conductivity character of the sample and check its uniformity and

quality at discrete points across a graphene film. In contrast to conventional techniques such as Hall bar devices, scanning tunneling microscopy, and employment of conductance atomic force microscopy for measurement of sheet conductivity, THz technique offers much more reliable and repeatable results.[113]

For conductive materials, THz conductivity is calculated from complex permittivity which can be obtained through phase and amplitude data of THz-TDS measurements. However, due to lack of enough THz power at low frequency range, DC conductivity cannot be extracted directly. For this purpose, well established existing conductivity models are employed. Accordingly, by using measured data, DC conductivity is extrapolated.

Understanding frequency dependent sheet conductivity of SLG is important for its utilization. However, its very thin nature leads to some design constraints. Therefore, MLG samples with varying layer numbers can be preferred for different types of applications, which makes it necessary to characterize and explain frequency dependent sheet conductivities of them as well.

This chapter involves THz conductivity measurements of two different SLG samples, (one on quartz and the other on PVC) and MLG samples with 27, 49, 66, 69, 85 and 100 layers on quartz. Conductivity behaviors of SLG samples are completely different and, they can only be explained by different THz conductivity models. On the other hand, MLG samples, required a thickness dependent conductivity examination and the behaviors were modelled with either Drude or with Drude-Smith model.

4.2 Models for THz Conductivity

To understand the mechanisms of charge carrier dynamics, two conductivity models are reviewed in the following sections which are the Drude model and Drude Smith model.

4.2.1 Drude Model

Drude model is a basic conductivity model that treats electrons as free carriers and investigates their transport dynamics under the effect of an electric field.[57] The nature of kinetics of the free carriers are considered to be that of molecules in a gas phase, which leads to ballistic movement between elastic scattering events. Model assumes that collisions lead to complete randomization of the carrier momentum and thermalization with the surroundings. Collisions are described with $\Gamma = \frac{1}{\tau}$ where Γ is scattering rate and τ is the time between collisions.

Classical form of the Drude model includes the notion of a finite carrier mass which does not apply to massless Dirac fermions of graphene. However, quantum theories of electron dynamics in graphene have been shown to be well described with a Drude form given in equation 4.1.[78, 80,119] Equation 4.2 and 4.3 indicate real and imaginary parts of complex conductivity. Here, ω is the frequency and Γ is scattering rate. D is the Drude weight and characterizes the magnitude of the response (equation 4.3). υ_F is the Fermi velocity and it has a value of 1.1×10^6 m/s when electron-electron interaction is neglected, and N is the carrier density.

$$\hat{\sigma}(\omega) = \frac{D}{\pi}\frac{1}{(\Gamma - i\omega)} \qquad \textbf{(4.1)}$$

$$\sigma_{real}(\omega) = \frac{D\Gamma}{\pi}\frac{1}{(\Gamma^2+\omega^2)} \qquad \textbf{(4.2)}$$

$$\sigma_{imaginary}(\omega) = \frac{i\omega D}{\pi}\frac{1}{(\Gamma^2+\omega^2)} \qquad \textbf{(4.3)}$$

$$D = \frac{\upsilon_F e^2}{\hbar}\sqrt{\pi\,|N|} \qquad \textbf{(4.4)}$$

Drude model can also be stated in terms of Fermi energy, E_F, as shown in equation 4.5. Real and imaginarty parts of the complex conductivity are given in equation 4.6 and 4.7.

$$\hat{\sigma}(\omega) = \frac{e^2}{h}\frac{2E_F}{(\hbar\Gamma - i\hbar\omega)} = \frac{G_0 E_F}{(\hbar\Gamma - i\hbar\omega)} \qquad \textbf{(4.5)}$$

$$\sigma_{real}(\omega) = \frac{G_0 E_F \hbar\Gamma}{(\hbar\Gamma)^2 + (\hbar\omega)^2} \qquad \textbf{(4.6)}$$

$$\sigma_{Imaginary}(\omega) = \frac{G_0 E_F i\hbar\omega}{(\hbar\Gamma)^2 + (\hbar\omega)^2} \qquad \textbf{(4.7)}$$

Here, e is the elementary charge and G_0 ($2e^2/h$) is the universal conductivity of graphene.

4.2.2 Drude-Smith Model

Drude-Smith (DS) model follows the generalization of well-known Drude model.[120] DS has become popular during the last decades and it has been intensely used in the interpretation of THz conductivity in a variety of materials with nanoscale inhomogeneity and disorder, such as polymers, nanostructured materials, and percolative systems.[121] These type of materials exhibit strong carrier localization due to defects in their structures. Defects decelerate carrier propagation by causing destructive interference between carrier scattering events. This nature is effectively captured by DS which works well for semimetals near the metal-insulator transition providing a better fit to both real and imaginary parts of conductivity.[122]

Functional form of DS model is given in equation 4.8 where W_D is the Drude weight and c_n coefficient represents the fraction of original electron velocity after nth collision.

$$\hat{\sigma}(\omega) = \frac{W_D}{1-i\omega t}\left[1 + \sum_{n=1}^{\infty} \frac{c_n}{(1-i\omega t)^n}\right] \quad \textbf{(4.8)}$$

Truncation of this infinite series at n=1 is found adequate to explain the behavior of carriers. This means that the carriers preserve fraction of their initial momentum during the first scattering event, but in every subsequent scattering events the velocity is randomized.[123] Therefore, equation can be expressed as in equation 4.9 and 4.10 for real and imaginary parts.

$$\sigma_{real}(\omega) = \frac{W_D}{(1+\omega^2 t^2)^2}[1 + \omega^2 t^2 + c(1 - \omega^2 t^2)] \quad \textbf{(4.9)}$$

$$\sigma_{imaginary}(\omega) = \frac{iW_D}{(1+\omega^2 t^2)^2}[1 + \omega^2 t^2 + 2c] \quad \textbf{(4.10)}$$

In these equations, c determines the shape of the conductivity spectra, and is allowed to be between -1 and 0, reflecting the back-scattering of carriers. When c=0 Drude model is retrieved and carrier momentum is randomized for each scattering event. Negative values of c indicate that carriers are back scattered or localized resulting in a suppression of the real and imaginary parts of the conductivity. The case where c = -1 reflects an insulator like response due to complete localization of carriers and results in a completely suppressed DC conductivity.[124]

4.3 Sample Preparation

One of the most important requirements for sample preparation part is to find substrates which are mainly transparent to THz wave. For this purpose, quartz and PVC substrates were chosen due to their high transmittances with thicknesses of 75 μm and 500 μm. Samples were prepared as explained in section 3.2. SLG samples were transferred to PVC or quartz. MLG samples with 27, 49, 66, 69, 85 and 100, layers were transferred onto quartz. Both sample and substrate size were larger than THz beam size in order to prevent the diffraction effects. Therefore, sample can be considered as irradiated at normal incidence by a plane wave. During the measurements, it was assumed that all the samples were homogeneous thin films.

4.4 THz Measurements of SLG and MLG Samples

THz measurements were done with transmission mode THz-TDS system which is described in section 2.5. After system was optimized, sample holder was arranged as shown in Fig. 4.1 with an aperture of 5 mm. Then, it was placed at the focal point of off axis parabolic mirrors on a XYZ stage where THz spot size was approximately 5 mm. Electric field strength of THz was optimized by aligning the position of sample holder with the micrometers of XYZ stage.

Figure 4.1. Iris sample holder.

After signal and sample holder position were optimized, firstly an air reference measurement was recorded. Secondly, substrate (Quartz or PVC) was placed on the iris sample holder and THz profiles were collected. Thirdly, THz profiles of SLG and MLG samples were recorded (Fig. 4.2 (a), (b) and Fig. 4.3). Each measurement was repeated at least five times to increase the SNR by averaging and to check the experimental reproducibility. System stability was confirmed with a final step of taking air reference spectrum for comparison with the first air measurement. The THz waveforms were recorded over a 10 ps time window with a 10 μm step size. All the measurements were done at temperature and humidity controlled conditions (T =20˚ C and H% =3).

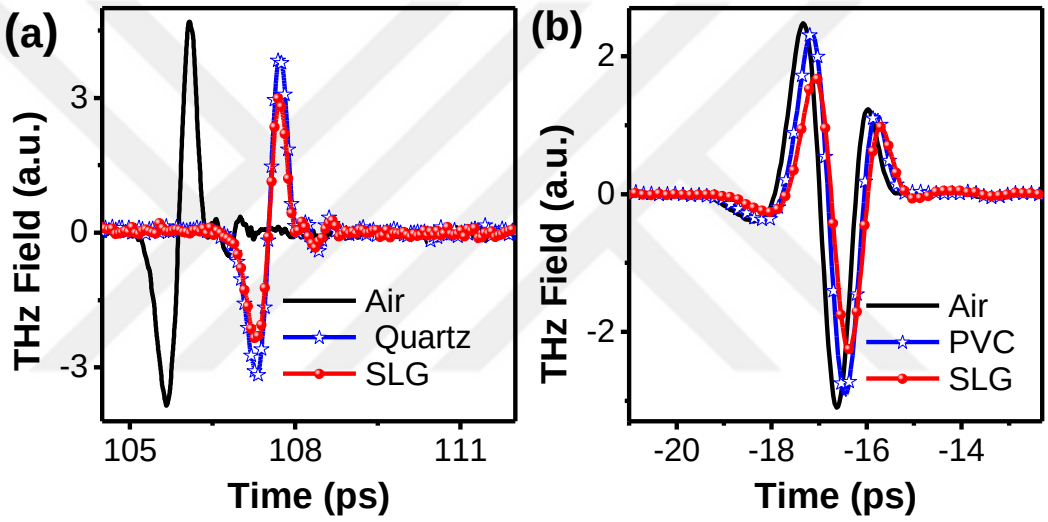

Figure 4.2. Measured THz electric-field waveforms of (a) air, quartz substrate and the substrate with SLG, (b) air, PVC substrate and the substrate with SLG.

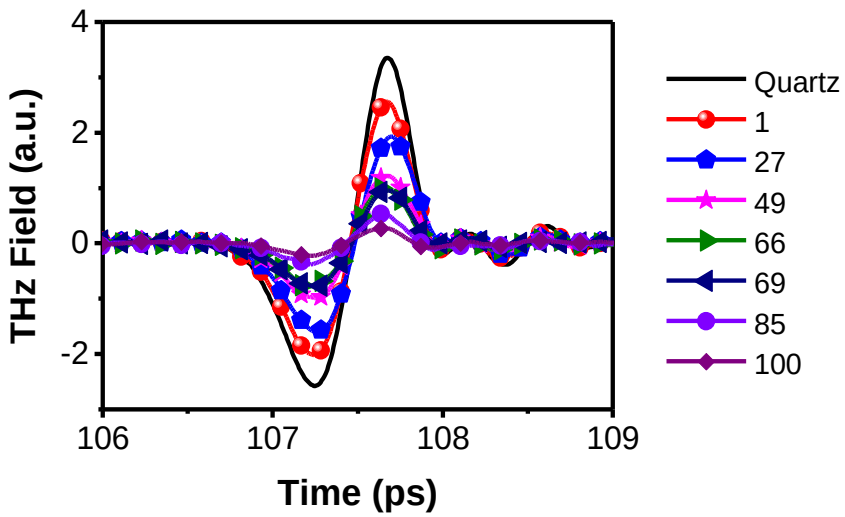

Figure 4.3. Measured THz electric-field waveforms of quartz substrate and the substrate with different MLG samples.

4.5 Complex Refractive Indices of Reference Substrates

After THz time domain profiles of air and substrate were taken, average waveforms were converted into frequency domain data with FFT analyses. In order to extract optical parameters in a correct manner, appropriate FFT window choice is vital. Moreover, data range should not include the echoes stemming from crystal or any optical component in the system. After FFT, phase information of sample and reference was provided and through equations 2.2 and 2.3 frequency dependent complex refractive index of substrates (PVC or quartz) were extracted over a frequency range of 0.1-1.5 THz (Fig. 4.4 (a) and (b)).

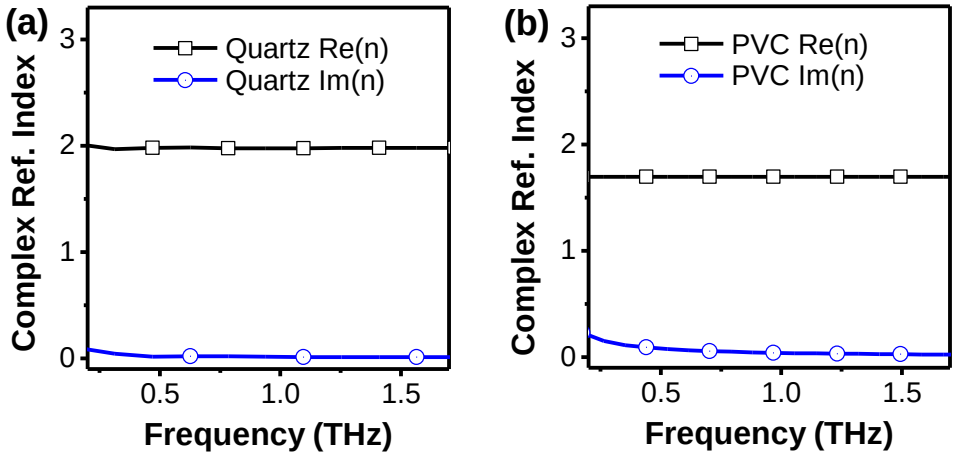

Figure 4.4. Complex refractive index $n_{sub}(\omega)$ of (a) quartz, (b) PVC.

4.6 Complex Conductivity of CVD SLG on Quartz and PVC

Average THz time domain profiles of SLG and quartz (Fig. 4.5 (a)) were transformed into frequency domain data and amplitudes were given in Fig. 4.5 (b).

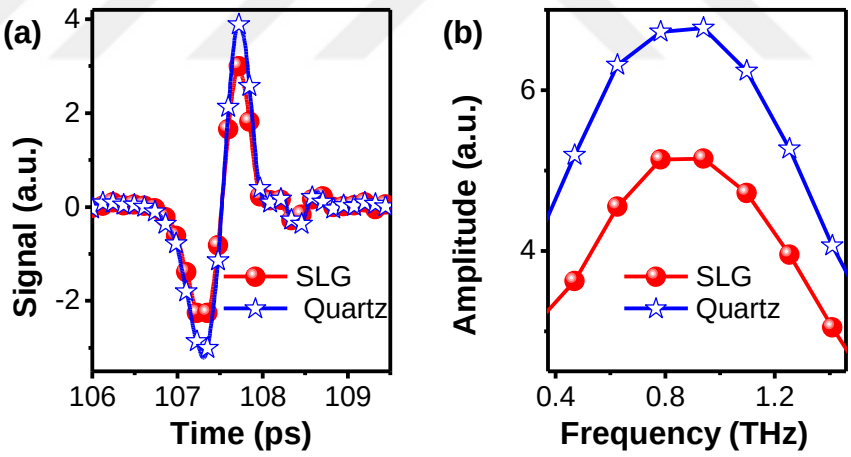

Figure 4.5. (a) Measured average THz electric-field waveforms transmitted through the quartz substrate and the substrate covered with SLG. **(b)** The amplitudes of Fourier transforms of the corresponding time-domain signals.

As Fig. 4. 5 (b) presents, even though SLG has an atomic thickness, it creates a significant decrease in the transmission of THz electric field (approximately 20%). Several other studies have also indicated this distinct behavior of SLG.[108,125] This pronounced response is a reflection of graphene's massless carriers which provide it with unusually high sheet conductivity and very high achievable carrier mobilities.

THz conductivity of SLG was calculated by using thin film approximation as given in equation 4.11 (It is introduced in Chapter 3; here complex form of the approximation is used).

$$\hat{\sigma}_{sh} = (1 + \hat{n}_{sub.})\left(\frac{A_{subsrate}}{A_{Sample}} - 1\right)/Z_0 \qquad \textbf{(4.11)}$$

We accepted the THz refractive index of the quartz substrate as n = 1.96 due to its dispersionless nature in the attainable THz bandwidth (Fig. 4.4 (a)).

Figure 4.6 (a) presents the intraband complex sheet THz conductivity of SLG on quartz with its real and imaginary parts. Behavior of both real and imaginary conductivities can be described as predominantly flat in the 0.2-1.5 THz frequency range. This type of conductivity can be well explained with Drude model. Imaginary part of the conductivity is neglected since it is almost zero and Drude fit of the real part of conductivity is given in Fig. 4.7 (b) (Conductivity values are specified in the unit of G_0, quantum of conductance, which equals to $2e^2/h$ =77.3μS). An almost spectrally flat conductivity suggests large momentum scattering rate for the graphene samples, $\omega \ll \Gamma$, which means that accessible frequency range is much lower than the carrier scattering rate in SLG sample.[126,127]

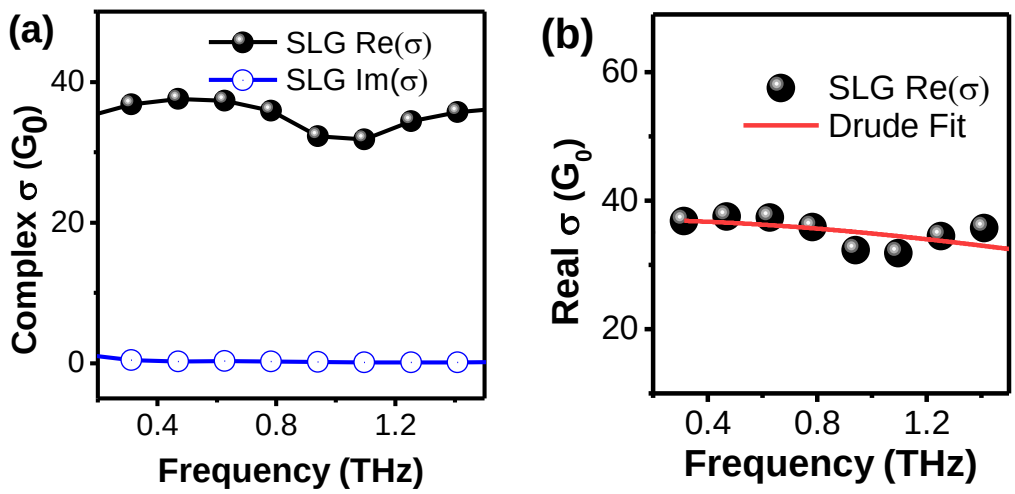

Figure 4.6. (a) Complex sheet conductivity of the graphene layer, extracted from the relative transmission. The conductivity spectra are normalized by the quantum of conductance $G_0=2e^2/h$, (b) A fit of the real conductivity to Drude model.

Derived transport properties from the best fit to the Drude model are given in Table 4.1. The real part of the sheet conductivity of SLG is nearly 35 G_0, which is expected and observed in other studies also due to high carrier mobility of graphene and unintentional carrier doping arising from the sample growth and transfer process.[117]

Table 4. 1. Derived transport properties of SLG on quartz.

	σ (G_0)	D (mS)	E_F (meV)	Γ (THz)	N (cm^{-2})	μ (cm^2/V·s)
SLG	35	100	-610	3.98	$2.7\ 10^{13}$	630

Fermi energy is given with a negative sign which is a result of the known hole doping for CVD-grown graphene films. Mobility of SLG is extracted as approximately 630 cm^2/V·s by using the relation between carrier density, N, optical conductivity, and elementary charge (Equation 4.12).

$$\sigma = N\mu e \qquad \textbf{(4.12)}$$

SLG may have a large variety of mobility values ranging between 297 to 3000 $cm^2/V \cdot s$ depending on the quality of fabricated SLG.[80, 97, 108, 120,126] Especially in a CVD growth process sample is subjected to chemicals that may leave residual chemical impurity or defects affecting the observed optical parameters drastically.[129] Our extracted mobility value is well within the range of the observed mobilities reported in the literature.

Although it is not possible to measure DC conductivity directly with THz-TDS technique, it can be extrapolated with the modified form of Drude model described in equation 4.13. Here, by using fitted scattering rate and Drude weight, DC conductivity of SLG on quartz can be extrapolated.

$$\sigma_{real} = \frac{D}{\pi\Gamma} \qquad \textbf{(4.13)}$$

In our case, since the scattering rate of charges (3.98 THz) is well above the frequency range of the experimental bandwidth, obtained conductivity is directly comparable to the DC value. Therefore, this spectrally resolved conductivity measurement can be replaced by a single real-valued quantity reflecting the DC conductivity of the graphene film. As a result, DC conductivity of our SLG on quartz sample can be accepted as approximately 30 G_0.

Terahertz conductivity of SLG on PVC was also characterized following the same steps. Average THz time domain profiles of SLG and PVC were transformed into frequency domain data as shown in Fig. 4.7 (a) and (b).

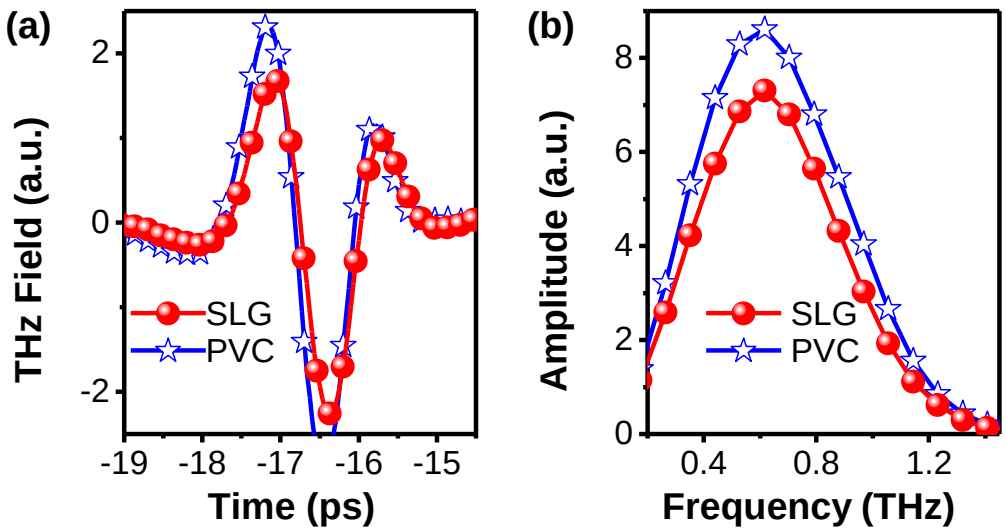

Figure 4.7. (a) Measured average THz electric-field waveforms transmitted through the PVC substrate and the substrate covered with a SLG. (b) The amplitudes of Fourier transforms of the corresponding time-domain signals.

With implementation of thin film approximation, complex sheet conductivity of SLG on PVC was calculated. Considering the flat, frequency independent index of PVC within the attainable frequency range, the index of the substrate was taken as 1.75 in all calculations. (Fig. 4.4 (b)).

Figure 4.8 (a) presents the intraband complex THz sheet conductivity of SLG with its real and imaginary parts. Although imaginary part exhibits a frequency independent behavior and can be assumed as zero, real part has a frequency dependent nature in the 0.2-1.5 THz frequency range. The observed behavior is very different than the one with SLG on quartz. This sample has a real conductivity that increases with increasing frequency. This type of behavior cannot be explained by Drude model ,which can explain conductivity behavior that has maximum value at zero frequency in the real part.[122] The observed frequency dependent behavior is better described by Drude-Smith model. DS fit of the real part of conductivity is given in Fig. 4.8 (b). A frequency dependent conductivity suggests small momentum scattering rate for the

graphene samples, indicating a longer life time of carriers due to charge localization effects.

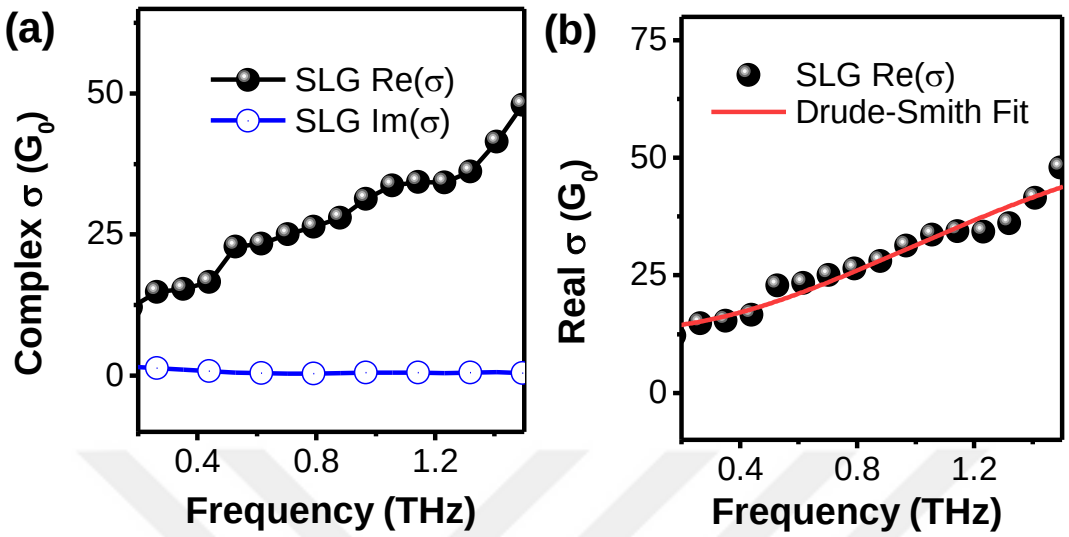

Figure 4.8. (a) Complex sheet conductivity of the graphene layer, extracted from the relative transmission. The conductivity spectra are normalized by the quantum of conductance $G_0=2e^2/h$, (b) A fit of the real conductivity to DS model.

Derived transport properties from the best fit to the DS model are given in table 4.2. The real part of the sheet conductivity of SLG is nearly 34 G_0 at 1THz. This large conductivity stems from high carrier mobility of graphene and unintentional carrier doping arising from the sample growth and transfer process, similar to SLG on quartz.

Table 4. 2. Derived transport properties of SLG on PVC.

	σ (G_0)	D (mS)	E_F (meV)	Γ (THz)	N (cm^{-2})	μ ($cm^2/V\cdot s$)	c
PVC-SLG	34	108	-700	0.36	$3.6\ 10^{13}$	450	-0.87

The obtained DS response of frequency dependent terahertz conductivity from SLG is not common but exists in literature.[112,130] We observe a large negative value of c

(- 0.87), which is an indication of structural disorder and results in back scattering of the carriers.[131] Similarly, a large c parameter of -0.6 was also observed in the study of Dadrasnia et al.[112], which was again based on structural disorder of SLG. Moreover, short scattering rate of 0.36 THz points out the longer life times of carriers due to back scattering and localization effects.

Investigation of THz responses of two different SLG reveals that samples have dissimilar intraband THz conductivity behavior. In one case conductivity behavior can be well described with Drude model while the other case requires employment of Drude-Smith model. Although carrier transport is diffusive in nature in both of the samples (life time of carriers can be measured with experimental SNR), their behaviors completely differ from each other.

Observed difference in transport parameters of SLG samples can be accounted for by taking into consideration the following. First of all, it is known that qualities of produced SLG thin films can be astonishingly different due to growth process, which can produce extended defects such as grain boundaries, cracks and wrinkles. As a result, electronic properties of graphene can be harshly degraded leading to non-continuous conductivity.[130] Also, transfer procedure, which may cause formation of rips and fractures in the structure, can affect quality of sample drastically leading to production of physically separated domains that can lead to nano localization. Therefore, difference in the conductivity behaviors of our SLG samples might have been caused by growth and transfer process.

Furthermore, given the atomic thickness of graphene, its electronic properties are strongly affected by its surrounding dielectric environment reflecting the importance of substrate. Quartz is highly transparent to THz so it is a good substrate choice for our studies. However, due to its surface roughness and surface optical phonons, it can seriously hinder carrier mobility of graphene.[132] Therefore, relatively low mobility of our SLG on quartz sample (630 $cm^2/V \cdot s$) can be stemming from substrate effect. The other substrate, PVC can form good conformal contact with graphene and its flexible nature is a great advantage for exciting applications.[133] Nevertheless, relatively high

carrier density of SLG on PVC may be caused by the stronger doping capability of PVC due its polymeric and thin nature. Therefore, it is important to emphasize the graphene-substrate interactions, which can be affected by interfacial traps, lattice phonons, and charge impurities. [134]

Our results indicate that in terms of conductivity, both SLG samples have similar and very high values at 1 THz. Even though their mobilities are not that different from each other, lower mobility value of SLG on PVC (450 $cm^2/V \cdot s$) reflects the structural disorder. Overall examination of mobility results of both samples reveals that they are far inferior to the estimated intrinsic values of SLG (200000 $cm^2/V \cdot s$) due to the above discussed issues.

4.7 Complex Conductivity of CVD MLG on Quartz

THz conductivities of MLG on quartz were also characterized following the same steps. Average THz time domain profiles of MLG and quartz were transformed into frequency domain data as shown in Fig. 4.9 (a) and (b).

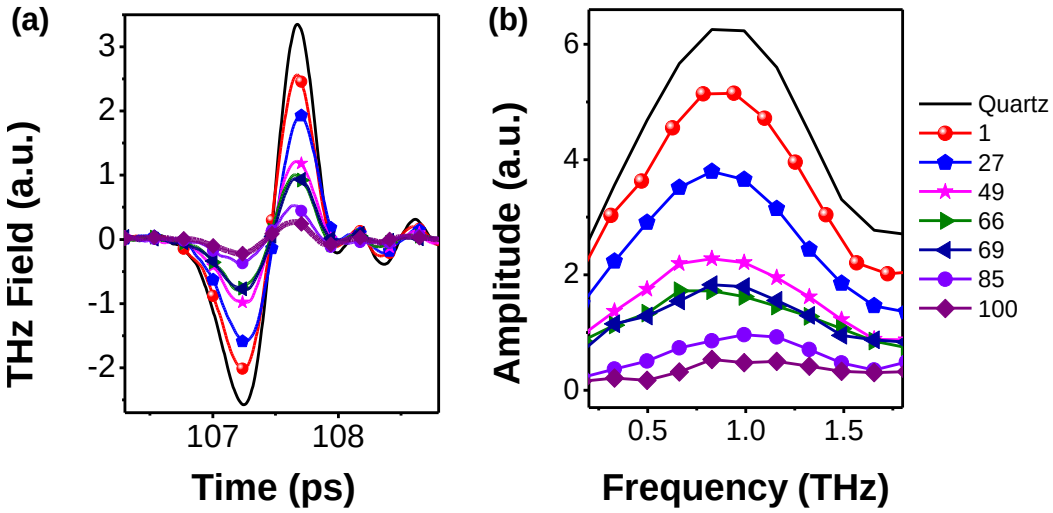

Figure 4.9. (a) Change in average THz profile based on layer thickness, (b) THz electric field amplitude in the frequency domain by FFT.

With the increase in layer number, transmitted THz pulse intensity decreases. Change in the peak values of % transmittance of THz at 1 THz with layer number is given in Fig. 4.10. When peak values are analyzed, it is noticed that each additional layer of graphene alters transmittance in a different amount. This results in a nonlinear behavior with thickness unlike ~2% absorption for each added layer at visible and near IR region.

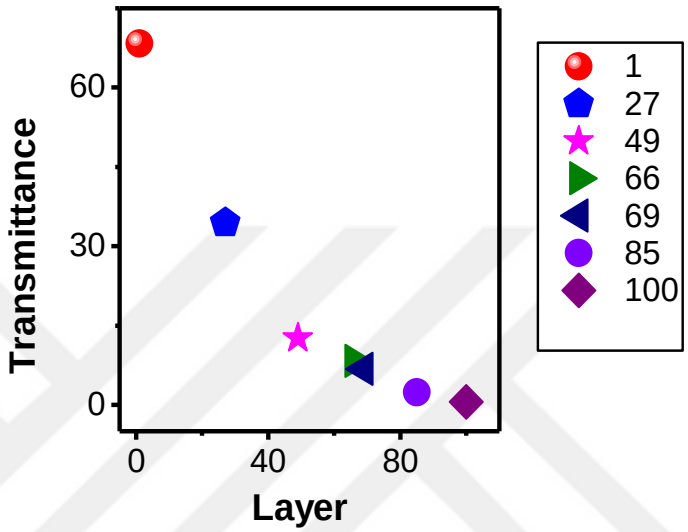

Figure 4.10. %THz transmittance change with layer number at peak point of THz signal at 1THz.

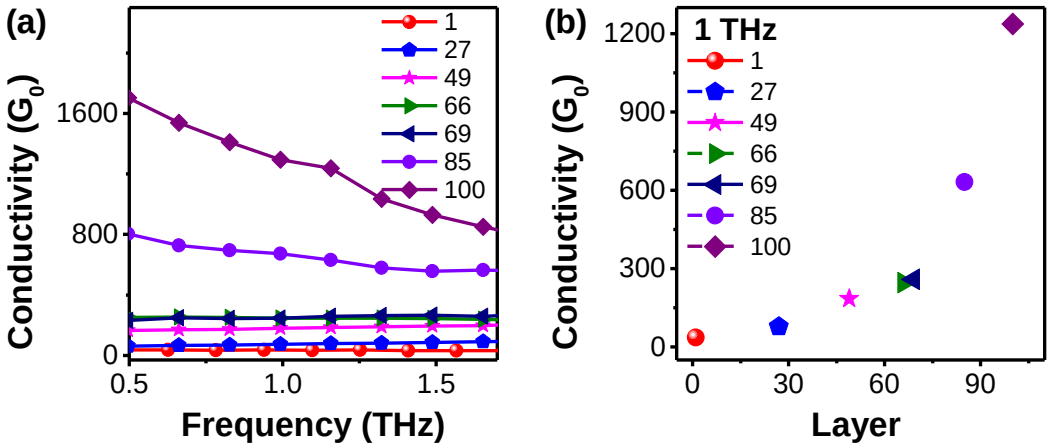

Figure 4.11. (a) Frequency dependent conductivity behavior of SLG and MLG samples, (b) Conductivity values of samples at 1 THz.

By using thin film approximation, complex sheet conductivities of MLG on quartz were calculated. Figure 4.12 (a) presents the intraband THz sheet conductivities of MLG samples. Since imaginary parts are almost zero, they are neglected. Figure 4.11 (b) illustrates the change in sheet conductivity at 1 THz with increasing layer number. While SLG has an approximate sheet conductivity of 35 G_0, conductivities change significantly with increasing layer number as: approximately 80 G_0 for 27 layer, 185 G_0 for 49 layer, 245 G_0 for 66 layer, 260 G_0 for 69 layer, 630 G_0 for 85 layer and 1240 G_0 for 100 layer. Such an increase in THz sheet conductivity is expected since atomic symmetry between adjacent layers are preserved with stacking of additional layers as reported in the study of Baek et al.[97] A similar conductivity increase was observed for our MLG samples as the layer number increases. While their conductivities were increased from 10 G_0 for SLG to 68 G_0 for MLG 12, ours increased from 35 G_0 for SLG to 80 G_0 for MLG 27. When two studies are considered together, the observed increase in conductivity appears to be linear with layer number for thin samples, while it becomes exponential beyond ca. 70 layers.

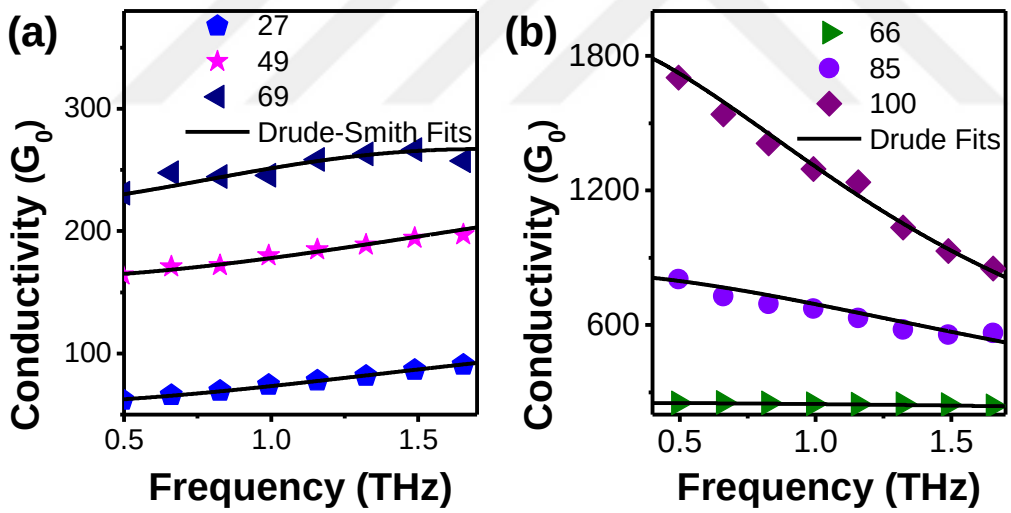

Figure 4.12. (a) Drude-Smith, and (b) Drude Model fits of frequency dependent conductivity.

Behavior of sheet conductivities of samples can be categorized under two groups depending on the layer number of samples. While thinner samples, 27 and 49 layer, indicate a slight increase in conductivity with increasing frequency, thicker samples, 85 and 100 layer, show sheet conductivities that decrease with increasing frequency in 0.2-1.5 THz range. Interestingly, region corresponding to 65-70 layer exhibits a conversion in frequency dependency with almost flat behavior of 66 layer. For fitting process, imaginary parts of the sheet conductivities were neglected. The behavior of 27, 49, and 69 layer can be well explained with DS model. Figure 4.12 (a) presents the best DS fits to the data. Extracted scattering rates for samples are given in Table 4.3 as 4, 4.8 and 2.6 THz for 27, 49 and 69 layer. Table 4.3 also presents the results of back scattering parameter, c as -0.74, -0.66 and -0.55 for 27, 49 and 69 layer. Obvious decrease in the c values is an indication of behavioral transition from DS to Drude. We observe a slight increase in scattering rate with increasing layer number excluding the 69 layer sample. Sheet conductivities of thicker samples can be described well by Drude model. Figure 4.12 (b) presents the best Drude fits to the experimental data.

Table 4. 3. Derived DS and Drude scattering rates ***Γ*** of MLG samples.

MLG	Back scattering parameter, c	DS *Γ* (THz)	MLG	Drude *Γ* (THz)
27	-0.74±0.01	4±0.3	**66**	6.6±0.8
49	-0.66±0.06	4.8±1.3	**85**	2.2±0.2
69	-0.55±0.02	2.6±0.4	**100**	1.45±0.05

Extracted scattering rates; 6.6, 2,2, and 1.45 THz for 66, 85 and 100, layer MLG samples by Drude model are given in Table 4.3. We observe a decrease in scattering rate with increasing layer number.

Observed frequency dependencies of MLG samples are not very strong as pointed out by their scattering rates. In the samples with less layer number, carrier interactions are relatively more intense, and results in shorter life times. On the other hand, MLG samples with higher layer numbers have smaller scattering rates and longer life times

because of distribution of carrier densities into the layers. Besides, it can be inferred that samples are mainly doped by substrate, which is reflected by the differences in their scattering rates depending on the layer number. If the growth process was the main reason of doping, we would observe only slight variations in the scattering rates due to diffusion and distribution of charges into different layers. Therefore, it is thought that substrate and static electric loading during the transfer process affected the static conductivity of MLG samples along with qualities of them.

Compared to SLG samples, MLG samples offer significantly higher sheet conductivity values. Moreover, samples exhibit similar mobilities with increasing thickness as a result of higher charge carrier densities and layered structures, which make them more resistant to charged impurities. Therefore, for charge transport applications, MLG can be preferred in terms of its higher conductivity, which will be affected slightly from the changes in mobility.

4.8 Conclusion

In this chapter, we have presented characterization of THz sheet conductivities of eight different large-area CVD samples with THz-TDS measurements. After THz time domain measurements were completed, FFT analyses were done and data were converted into frequency domain. Then, with the usage of standard thin film approximation, complex sheet conductivities were extracted. With elaborated models that can nicely fit the THz conductivity such as Drude and Drude-Smith model, sheet conductivity behaviors of SLG and MLG samples were described well.

Two different SLG samples displayed different frequency dependent conductivity behaviors. This situation reflects the importance of sample growth and transfer process since the quality of graphene films are strongly affected by both. Extracted mobility values of SLG samples are close to each other with a lower value for the one on PVC, which is explained with DS model. This result can be attributed to relatively more disordered structure of SLG on PVC.

THz sheet conductivities of MLG samples were separated into two categories. Conductivities of thinner samples exhibited slight increase with increasing frequency, and they were explained with DS model. Extracted scattering rates indicated a slight increase with increasing layer number. Thicker samples exhibited a slight decrease in conductivity with increasing frequency, which were well accounted for with Drude model. Decrease in extracted scattering rates with increasing number of layers reflected the longer life times of free carriers due to distribution of them into the layers. Overall, MLG samples exhibited a very pronounced increase in THz sheet conductivities with increasing layer number. This superior sheet conductivity compared to SLG samples suggests that MLG can be a promising platform for novel THz optoelectronic applications.

In this chapter, it is shown that THz-TDS is a noncontact and reliable technique that allows characterization of frequency dependent sheet conductivity for both SLG and MLG samples. Despite the limitations arising from relatively higher noise of THz measurements, especially for thin film samples compared to the substrates, the results are consistent with the literature. This shows the strength of THz technique on conductivity measurements.

CHAPTER 5

TERAHERTZ CHARGE CARRIER DYNAMICS OF CVD GROWN SLG AND MLG

5.1 Introduction

Graphene, which is a model for 2D materials, facilitates energy related phenomena in a wide range of frequencies from optical to THz. Understanding nonequilibrium behavior of electron and hole plasma in graphene, which is created by ultrafast photoexcitation process, will allow its complete employment in high speed photonic applications and electronic devices. Therefore, relaxation of hot carriers in graphene, which has a gapless nature and conical energy momentum space, have been investigated intensely with several different pump probe systems such as IR pump - visible probe[135], visible pump-IR probe[136], degenerate[74] and nondegenerate optical pump – optical probe spectroscopies. These experimental techniques sense the interband conductivity of graphene probing the dynamics of carrier occupation at specific energies in the energy bands.[137] Other than visible and near IR applications of graphene, as its band structure and constant absorption suggests, expansion of the utilization into THz range is crucial. Intraband transitions of graphene can be probed with THz frequencies and graphene has strong nonlinear THz response, which makes it even more desirable in the application of active photonic devices that can operate beyond 100 GHz (0.1 THz).[138]

TRTS is a frequently used technique in the characterization of intraband nonequilibrium charge carrier dynamics in photoexcited graphene. Generally, sufficiently low THz electric fields are preferred so that graphene-THz interaction stays in the linear regime.[61, 125, 127,139,140] Optical pump THz probe studies reveal significant insights about relaxation dynamics. Subsequent to linearly polarized ultrafast optical pump pulse, photoinduced hot carriers distribute themselves in a

quasiequilibrium which can be described as Fermi-Dirac distribution.[141] The following cooling dynamics depend on two main processes which are carrier-carrier scattering and carrier-optical phonon scattering. Through these mechanisms cooling of carriers are achieved with an isotropic thermal distribution and energy is dissipated from carrier population to the lattice.[142] Carrier-carrier scattering, which can occur in tens of femtoseconds,[143] leads to transfer of energy of photo induced carriers and creation of secondary hot electrons that come from conduction band.[140] The cooling via carrier-phonon scattering involves emission of optical phonons, which has an energy of ∼200 meV due to strong carbon-carbon bonds, on a time scale of ∼100 to 500 fs and energy is transferred to the lattice as heat. Branching ratio between these two competing relaxation channels are determined by the speed of each individual pathway.[140] When the carrier temperature is sufficiently below the optical phonon energy, carriers are coupled with low energy acoustic phonons (∼4 meV). This process can continue for tens of picoseconds. However, carrier relaxation time of the carrier-acoustic phonon interaction can be less than ten picoseconds depending on the degree of disorder of graphene sample that can cause large momentum and large energy acoustic phonon emission.[141] Both fast and slow scattering dynamics of photo created charges affect the performance of optoelectronic devices.[144]

Doped graphene can be described as a semimetal with Fermi level moved away from the Dirac point.[140] THz response of photoinduced conductivity strongly depends on Fermi level of the graphene sample. Samples with low doping density (Fermi level is close to the Dirac point) have very slow cooling dynamics which stem from disappearing density of states, energetic incompatibility with the optical phonons, and also weak scattering with acoustic phonons.[145] Also, the large mismatch in Fermi velocity and sound velocity (v/s ≈ 100), constrains the scattering between electrons and acoustic phonons.[144] However, the slowest cooling times observed have been on the order of hundreds of picoseconds [127] contrary to anticipated few nanoseconds from carrier–acoustic–phonon scattering in ideal graphene.[145] This situation reflects the dominance of disorder-assisted electron–phonon (supercollision) scattering in the cooling mechanism of carriers.[146] Degree of disorder in the structure of specific

graphene sample plays a major role in the effectiveness of carrier–acoustic–phonon scattering. [147]

In Chapter 5, time resolved THz response and charge carrier dynamics following ultrafast photoexcitation of several CVD grown graphene samples, on quartz, PVC and PE substrates, are presented. In 5.1.1 literature examples of dynamic THz response of SLG is introduced. In 5.1.2 literature review on THz dynamics on MLG is presented. In section 5.2 sample preparation is described briefly. In section 5.3 experimental details of TRTS measurements are given. Section 5.4 includes experimental results and discussions of SLG THz dynamics. In 5.5 THz dynamics of MLG samples are discussed and 5.5.1 and 5.5.2 include 800 nm and 400 nm pump experimental results and discussion. Also in 5.5.3 comparison of 800 nm and 400 nm pump THz probe dynamics is presented. Section 5.6 presents experimental results and discussions of MLG samples on PE and PVC substrates. Finally, a brief summary of the results is given in section 5.7.

5.1.1 Literature of SLG THz Dynamics

THz dynamics of SLG is especially important since it is a direct probe of intraband transitions of free carriers without the interference of interband transitions. Being able to understand behavior of charges under nonequilibrium conditions with an extensive range of technologically feasible temperatures, thanks to graphene's nature, will carry the generation of photocurrent [148] and operation of photodetectors [149] to the next level. Therefore, THz dynamics of SLG has been examined carefully by many research groups under various experimental conditions. Many studies in literature in the discusses the effects of doping level, quality, substrate type and temperature of SLG sample and also pump color and intensity on observed charge carrier dynamics.

The study by Jnawali et al. pointed out the negative transient response of photo induced THz conductivity of CVD grown SLG.[125] Sample, without the effect of pump, had a THz conductivity which is described well with Drude model. In this work, both nature of observed negative conductivity and effect of pump intensity on

charge carrier dynamics were investigated. Observed initial sharp rise in the differential THz signal was attributed to the heating of charges due to pump effect resulting in enhanced carrier-carrier scattering and negative conductivity. Relaxation mechanism of SLG occurred on a few ps time scale. It was stressed out that excitation conditions and physical properties of sample such as doping level and mobility determined the photoinduced conductivity character of SLG.

Frenzel et al. also investigated photo induced conductivity of CVD grown SLG with applied 800 nm optical pump and THz probe.[108] Following the optical pump pulse, a significant increase in the THz transmission was observed. This observed positive change was attributed to negative differential conductivity or reduced absorption of THz by SLG. Pump induced modulation of THz was described with single exponential fit of the differential signal with a decay time of 1.7 ps. The main relaxation process was indicated as the cooling of the coupled electron-phonon system. In order to verify the observed negative and non Drude behavior of conductivity, pump probe experiments were repeated under different temperatures (4 to 300 K) and CVD samples on different substrates (sapphire, quartz, and borosilicate glass). Results were consistent with each other revealing that this was a general property of doped graphene ($6x10^{12}$ cm^{-2}). The negative sign and non-Drude behavior of THz conductivity was explained with increased scattering rate and carrier distribution as a result of higher nonequilibrium temperatures of transient system created by pump effect. Strong electron–phonon scattering along with increased population of phonons causes suppression of free-carrier conductivity. This work demonstrated strong tunable THz response of conductivity by optical means on a picosecond scale.

Tombet et al. reported charge carrier dynamics of an exfoliated graphene sample under IR pulse excitation.[150] Photo excited carriers indicated a fast relaxation and carrier recombination in a relatively slower manner. In the study, photoconductivity of sample decreased with applied optical pump revealing that graphene sheet amplifies an incoming THz electric field. THz emission of graphene depended on intensity of optical pump light and after a threshold power, the amplification started.

This behavior was attributed to the generation of negative conductivity. Amplification behavior of graphene was also supported with both amplitude and phase data of the measured THz electric field. An increase in the THz amplitude was observed with the presence of sample, while the Lorentzian like dispersion of phase of the THz electric field around the gain peak indicated clear inverted behavior. Furthermore, THz probe time dependent emission was also confirmed. The researchers interpreted that this coherent stimulated emission nature and pump intensity dependent behavior of graphene can be benefited in the application of THz lasers.[151]

Docherty et al. discussed the change in the behavior of THz conductivity of SLG from positive in vacuum to negative under nitrogen, air, and oxygen environment.[152] The study suggested that dynamic negative conductivity stemmed from amplified stimulated THz emission with above a certain threshhold of pump intensity. Gierz et al. have further investigated THz stimulated emission with photoexcitation and experimentally indicated that electron and hole distribution start to differ from each other only within 130 fs after photoexcitation.[153] Therefore, beyond this time interval, population inversion that will provide the stimulated emission is not achievable.

Fu et al. presented ultrafast optical pump THz probe results of a CVD grown SLG on quartz.[154] Due to intrinsic doping level of sample, a strong carrier response and frequency dependent THz conductivity was observed without the effect of optical pump. With 800 nm optical pump, an increase in the differential THz signal was detected, which was also enhanced with increasing pump intensity in a nonlinear manner. Results were again explained with a transient decrease in the observed photo induced conductivity due to increased carrier scattering.

In the study of Kar et al. three CVD grown SLG with different doping levels were compared in terms of the character of photo induced THz conductivity and carrier dynamics.[141] Highly doped samples showed a transient decrease in THz transmission with applied optical pump which has a central wavelength of 785 nm. Decrease in the THz conductivity was explained with the generation of secondary hot electrons due to interaction of hot carriers with already existing ones. The SLG sample, with a Fermi

energy closer to the Dirac point, indicated positive THz conductivity due to dominating effect of intraband scattering which was attributed to the decreased momentum relaxation time stemming from disorder in the structure. The cooling mechanisms of both cases were based on the disorder- mediated electron-acoustic phonon interaction.

5.1.2 Literature of MLG THz Dynamics

Compared to 3D bulk materials, 2D structure of graphene indicates a weak phonon-mediated interlayer thermal coupling due to decoupled electronic states stemming from rotational stacking arrangements in different 2D layers.[155] Therefore, MLG samples, with consistent chemical and electronic properties of each individual layer due to nonexistent atomic bonds between layers [131], are particularly preferred in the design of practical devices since they offer balanced optical transmission along with mechanical strength, conductivity and device efficiency. As a result, understanding the structure of multi-layer stacks, mechanisms that can contribute to thermal equilibration between different layers, and charge carrier dynamics of MLG become a significant issue for designing more efficient optoelectronic devices. In the following part, several studies from literature are presented.

George et al. examined ultrafast carrier dynamics of two different epitaxial MLG samples with 12 and 20 layers using optical pump terahertz probe spectroscopy.[137] The study pointed out that the intraband THz conductivity of MLG samples depended on both carrier density and distribution. Time evolution of THz differential change explained as exhibition of two distinctive character which were an initial rapid decrease until 0.75-1 ps and then a slow recovery from 1 to 15 ps. The initial part corresponded to an increase in photo induced conductivity due to creation of electrons and holes. Following the optical pump excitation, a large population of carriers distributed themselves nonthermally which turned into termalization of them within 10-150 fs. After that carriers cooled down to a hot Fermi-Dirac distribution. Between 150 fs and 1 ps, intraband phonon scattering was observed which further provided cooling of thermalized carriers. Beyond ∼1 ps, slow increase in the transmission

reflected that dominant process was recombination of electron and holes determining the change in the THz conductivity. This process did not exhibit a simple exponential behavior indicating density dependency of carrier recombination times. The study stressed out that material disorder deeply affected momentum relaxation in epitaxial graphene samples. 20-layer MLG sample, which had a more disordered structure than the 12-layer sample, indicated approximately twice as fast recombination rate for the same carrier density. The measurements presented that cooling dynamics took place on subpicosecond time scales and carrier density and disorder in the structure affected recombination times strongly.

In the study of Choi et al. nonequilibrium THz dynamics of a few layer graphene sample was investigated via optical-pump THz-probe technique.[139] As a result of 800 nm optical pump pulse, increase in photo induced conductivity was observed. Immediately after photoexcitation, excess carriers thermalized with already existing plasma on a femtosecond time interval, achieving a Fermi Dirac distribution with an increased electron temperature. In this study, the MLG sample was highly n doped and change in the differential THz signal reflected population dynamics of excess holes. Therefore, recombination was dominated by interaction of excess holes with existing electron plasma. Recombination time was consistent with results of Auger and phonon-mediated recombination.

Strait et al. investigated the relaxation dynamics of epitaxial MLG with 14-layer at different substrate temperatures.[127] The study focused on the nature of carrier relaxation mechanisms of long lived carriers and how relaxation dynamics were affected by the function of carrier generation and recombination processes. Differential THz transmission decreased with the effect of pump at each specific substrate temperature reflecting the positive nature of photo induced THz conductivity. Room temperature relaxation dynamics, in a time scale of 1-10 ps, was attributed to the recombination of charges. Results indicated that immediately after interaction of THz with optical pump $\Delta T/T$ decreased on a time scale of$\sim$1 ps. After that time, recovery of signal started on time scales which strongly depended on the temperature of substrate. Lower substrate temperatures showed an increase in the

recovery time from tens of picoseconds at room temperature to hundreds of picoseconds at low temperatures. Two distinctive time interval were observed at low temperatures, a fast response of 50 ps and a slower behavior that lasted hundreds of picoseconds. The fast response, cooling of the charge carrier distribution, was affected both intraband and interband optical phonon emission. The slower cooling mechanism was not affected by the emission of optical phonons due to closeness of electron and hole distributions to the Dirac point. It was dominated by the recombination of charges.

Mihnev et al. discussed the interlayer thermal effects within the MLG samples.[156] In MLG samples, each layer protects its 2D nature due to tight confinement of electronic states. Therefore, interlayer conductivities are low mainly restricted by the occurrence of electron–phonon interactions within layers. Furthermore, observed weak phonon-mediated thermal coupling between the layers is a result of weak van der Waals interactions between layers and also existence of strong in-plane intralayer covalent bonds. However, the study pointed out that there was Coulombic interactions between charges of different layers in MLG, which provided a significant mechanism for thermal transport between layers. This interaction between layers also affected the hot carrier dynamics of charges, which were investigated by optical pump – THz probe spectroscopy. Three different MLG samples with 63, 35 and 3 layers were investigated at different substrate temperatures. For the sample with 63 layer, an increase in photo induced THz conductivity was observed with the effect of optical pump. This was attributed to the increase in electron occupation in conduction band with increased electron temperature. Within 1 ps, differential THz transmission reached its maximum value and then recovery of thermalized charges started with cooling of hot carriers to the substrate temperature. Relaxation times varied from a few picoseconds at room temperature to hundreds of picoseconds at cryogenic temperatures. Decay dynamics evolved from a single exponential character to a double exponential decay as substrate temperature decreased to cryogenic temperatures. Except high substrate temperatures, observed relaxation times did not depend on applied pump intensities. Slow cooling dynamics at low substrate temperatures reflected the presence of interlayer interactions. In MLG with 35 layer,

similar results were observed. Further investigation showed that with decreasing layer number, relaxation times also decreased which was an indication of interlayer interaction. Sample with 3 layers were also investigated to better emphasize the effect of interlayer interaction in MLG samples. This sample indicated much faster and completely substrate temperature independent carrier relaxation dynamics. This was attributed to very little or nonexistent nature of interlayer interactions.

Another study of Mihnev et al. investigated hot carrier dynamics of a wide variety of MLG samples systematically to observe main relaxation mechanisms.[147] The study showed that samples with high doping levels indicated an enhanced THz transmission with the effect of optical pump meaning negative photo induced THz conductivity. Extracted relaxation times of highly doped MLG samples indicated a single exponential behavior with a weak dependency on pump intensity and no dependency on substrate temperature even though they had varying degree of disorder in their structures. When lightly and highly doped graphene samples were compared, it was observed that lightly doped samples indicated longer relaxation times. This was attributed to decrease in efficiency of carrier-carrier scattering due to increased number of carriers in highly doped samples. Also, short relaxation times of lightly doped samples showed a strong dependency on substrate temperature. In the initial cooling of hot carriers, carrier-carrier and carrier-optical phonon scattering played a significant role within a time scale of tens of picoseconds. Moreover, relaxation dynamics of high doping case also involved carrier carrier and carrier optical phonon scattering. it was stressed out that carrier acoustic phonon scattering was insignificant on picosecond timescales.

5.2 Sample Preparation

A wide range of samples with different layer numbers, ranging between single to 100 layers, were prepared on quartz (500 micron) substrate. Also, PVC (75 micron) and PE (20 micron) substrates were chosen to examine the effect of substrate on charge carrier dynamics. All samples were grown by using CVD technique and layer numbers were characterized by optical measurements. Results of SLG, MLG samples

with 27, 49, 66, 69, 85 and 100 layers on quartz, PE MLG 32 layer and PVC MLG 30 layer were given in the chapter. The layer numbers were identified with both temperature and duration of growth with CVD process. Both sample and substrate size were larger than THz wave in order to prevent the diffraction effects. During the measurements, it was assumed that all the samples were homogeneous thin films.

5.3 Time Resolved THz Spectroscopy Measurements

Optical pump excitations of samples were performed with a center wavelength of 800 nm (1.55 eV) or 400 nm (3.1 eV). 400 nm light was produced with frequency doubling of 800 nm 1 kHz light, which is the output of Ti: Sapphire amplifier laser. For this purpose, Beta-Barium Borate Barium nonlinear crystal was used. UV spectroscopy measurements indicated that linear absorption of our samples were constant in the range of photoexcitation intensities used in the pump probe experiments. The CVD graphene samples were placed onto a stage for maximization of observed signal at the focus of 90° off-axis parabolic mirrors. The size of the THz beam was 7 mm. Pump beam was sent to the sample at an angle 5° from surface normal due to the design of the system. Size of the pump beam was arranged as 5 mm to ensure homogeneous photo excitation of sample. TRTS experiments were restricted to 1D measurements in which pump stage is scanned in order to change the relative arrival of optical pump pulse with respect to THz pulse. By this way, time dependent change in the transmission of peak THz field through photo excited sample can be recorded. The THz probe signal were mechanically chopped at 500 Hz and the change in the transmission was detected with a lock-in amplifier referenced to this frequency. In order to increase the SNR of the collected pump probe signal, each measurement was repeated 10-15 times. Between pump probe measurements, SNR of the system was checked by scanning the pump stage while THz electric field was fixed at the peak point without the existence of the sample to ensure stability of THz probe signal. All of the measurements were performed under temperature and humidity controlled environment. (T: 20-22˚C and H: 3-5%).

5.4 THz Dynamics of SLG

In pump-probe experiments, choosing the correct pump color is significant in order to be able to explore the inter and intraband transitions of SLG. Therefore, THz dynamics of SLG sample was investigated using an optical pump pulse of center wavelength of 800 nm which exceeds twice the Fermi level energy and provides linear interband transitions.[139] Firstly, the effect of pump pulse on the shape of the THz time domain signal was examined in order to figure out if 2D measurements were necessary. Figure 5.1 presents the results of time domain THz pulse profiles of SLG with and without the effect of optical pump pulse preceding the peak of the THz pulse by 3.5 ps. This probe delay time was selected in order to eliminate the effect of photo induction on the initial transient response of THz pulse. Measurements were repeated several times to ensure observed behavior was not affected by probable contaminants or defects in the SLG sample. The optical excitation caused an increase in the amplitude of observed THz pulse while shape of it was not altered nor was it shifted in time. This is an indication of flat dispersionless and almost entirely real conductivity with a negligible imaginary part due to high scattering rate of free charges of this specific SLG sample (3.98 THz) in THz region. Therefore, all pump probe measurements were based on 1D technique in which only the peak point of THz pulse was tracked as a function of pump-probe delay time, rather than examining the full waveform.

This observed increase in the transmission with photoexcitation is the result of decrease in THz conductivity. The origin of observed decrease in THz conductivity can be explained with modification of Drude model for the low frequency limit. In DC limit, real conductivity is expressed as $\sigma = D/\pi\Gamma$ (Equation 4.13) indicating that photoinduced conductivity will be determined by both scattering rate Γ and Drude weight D.

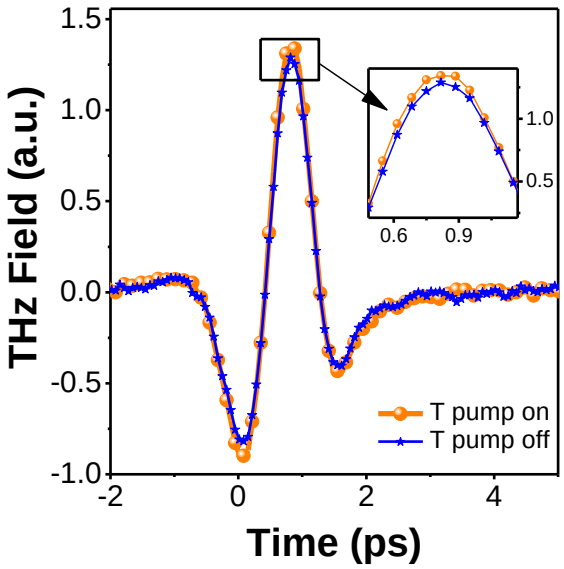

Figure 5.1. Measured THz time domain pulses transmitted through the SLG sample without (blue, stars) and with (orange, circles) the presence of optical pump pulse preceding the peak of the terahertz pulse by ~3.5 ps.

Therefore, the ratio of D/Γ, the conductivity, can increase or decrease depending on the effect of photoexcitation on SLG sample. D may increase with increased carrier density, while Γ may rise with increased effective temperature. For a conventional semiconductor, main effect will be increased carrier density with applied pump providing increase in observed THz conductivity. However, when a conventional metal is photoexcited, increased carrier density will not be significant compared to already existing large plasma of charge carriers but a significant enhancement in the scattering rate could be observed. This leads to decease in photoinduced conductivity as a result of the dominance of increase in observed scattering rate Γ. Electronic structure of graphene allows for either type of photoinduced THz conductivity depending on the initial doping level and scattering rate of SLG sample. Both high initial doping level and scattering rate of SLG reflect a metal like character and results in decreased transient conductivity, which is the case in our study. Our SLG sample has a quite high Fermi energy E_F of - 610 meV with corresponding carrier density of 2.7×10^{13}. Effect of Fermi energy on sign of photoinduced conductivity was clearly

demonstrated in the study by Kar et al.[141] where increased transmission was observed for samples with Fermi energies of -180 meV, -200 meV and decreased transmission for sample with -10 meV. Similar to our results, increased transmission with optical pump was also observed for SLG samples[125] having a Fermi energy of −275 meV with a carrier density of 4.6×10^{12}, and for SLG sample[108] that have a Fermi energy of -300 meV with a carrier density of 6×10^{12}. Compared to all these SLG samples, our sample had a very high Fermi energy supporting its strong negative THz conductivity. From these results, it can be concluded that SLG samples can have a wide variety of Fermi energies which can affect the observed optical pump THz probe results.

After time domain characterizations, pump probe measurements were performed at selected fluencies of 50, 100, 150, 400, 550, 950 and 1400 μJ/cm^2. Each measurement, which took approximately 15 minutes, was repeated for 10-15 times.

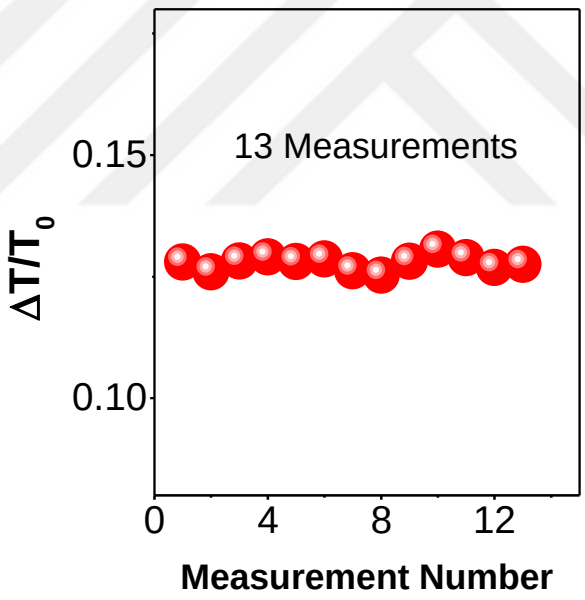

Figure 5.2. Variation in the differential THz signal at pump arrival time.

Figure 5.2 presents an example of consistency between measurements. Very low variation in the value of differential change in the THz amplitude at the pump arrival

reflects the quite high stability and reliability of measurements. Repeated measurements also improve the SNR of the results.

Figure 5.3. (a) indicates the positive nature of differential change in the amplitude ΔT/T of the transmitted terahertz probe pulse, as a function of the relative pump probe delay time at 7 different fluencies for the same SLG. This positive nature corresponds to an increase in the THz transmission. Immediately after photoexcitation, the differential signal shows an increase on a time scale of ~0.5 ps, which is the rise time, limited by the resolution of our TRTS set up. The initial rise of the signal mainly corresponds to creation of initial electrons and holes.

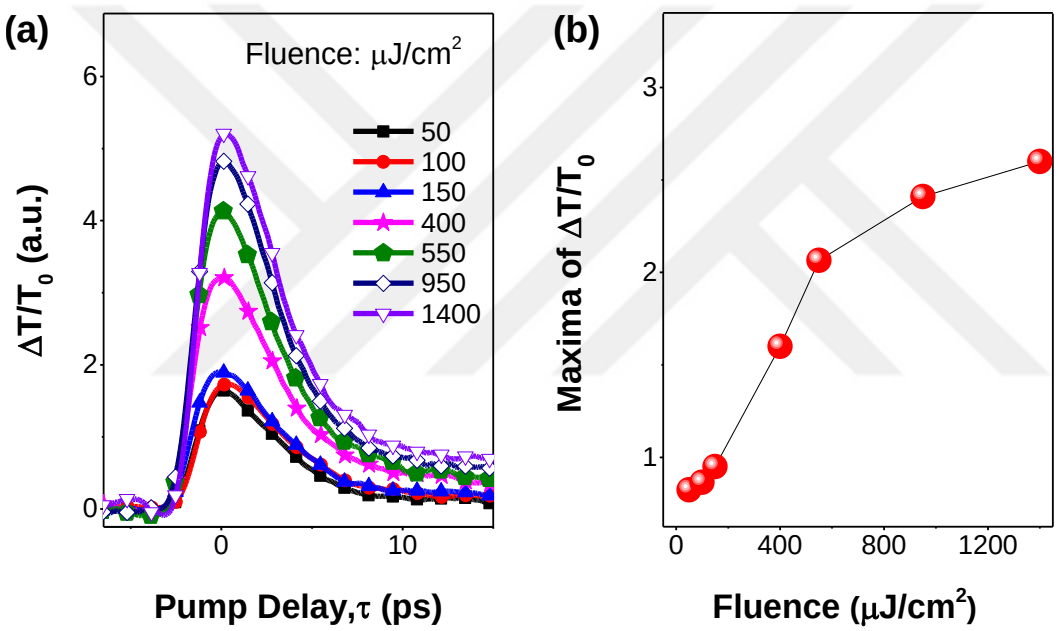

Figure 5.3. (a) Measured differential THz probe transmission ΔT/T as a function of the probe delay for SLG is given at seven different applied fluencies of optical pump pulse. (b) Maxima of the $\Delta T/T_0$ from part (a) as a function of applied fluence.

The peak part of the ΔT/T signal is the region where hot electrons can be found due to elevated carrier temperatures that leads to enhanced carrier-carrier scattering rate. Increase in transmission is provided with this metal like nature of SLG sample. For all investigated pump fluencies, recovery to the initial state was observed on a time

scale of a few picoseconds. Other SLG samples, with similar Fermi energies and carrier densities, were also measured under the same experimental conditions to make sure the same fluence dependent behavior was obtained.

Figure 5.3. (b) is drawn to better reveal the applied pump fluence effect on the differential THz signal thus the conductivity since the differential transmission $\Delta T/T_0$ is directly related to the dynamic photo induced THz conductivity, $\Delta\sigma$, by the equation 2.8 $\left[{}^{\Delta T}/_{T_0} \approx -\frac{Z_0}{n_s+1}\Delta\sigma\right]$. Strong sublinear nature of increase at peak points of signals suggest that pump induced increase in transmission is balanced and somehow saturated due to increased number of carriers with increased fluencies. Drude weight, which depends on carrier density and electronic temperature[157], becomes more dominant at relatively high optical pump fluence. This provides an increase in conductivity and balances the negative conductivity which stems from enhanced intraband carrier-carrier scattering.

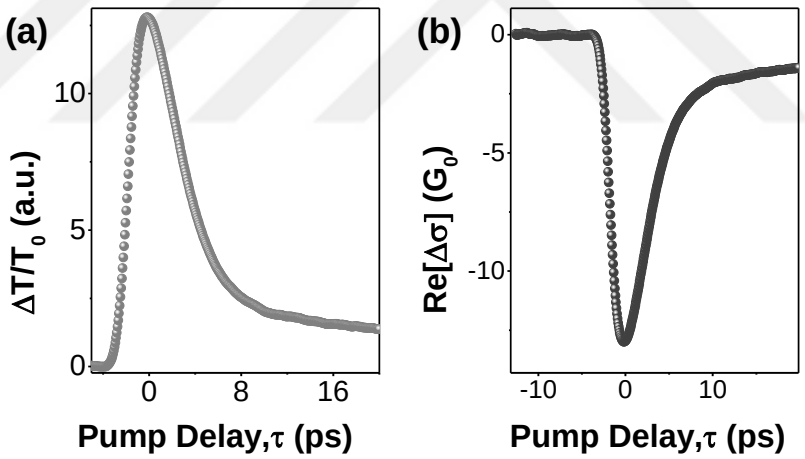

Figure 5.4. (a) Experimental differential THz transmission, $\Delta T/T_0$, as a function of pump – probe delay recorded at a fluence of 400 $\mu J/cm^2$. (b) Evolution of the real part of photo induced THz conductivity as function of delay time between the 800 nm pump and the THz probe.

The differential THz transmission, $\Delta T/T_0$, as a function of pump–probe delay recorded at a fluence of 400 μJ/cm^2 (optimum fluence that stay in linear region) is given in Fig. 5.4 (a). Extracted time evolution of dynamic conductivity of corresponding fluence with the above mentioned relation between differential change and photoconductivity is presented in Fig. 5.4 (b) in units of universal conductivity, G_0. The sharp decrease in the conductivity immediately after arrival of pump pulse is related to the heating of carriers which is then followed by quasiequilibrium carrier distribution with electron temperature. Very early relaxation mechanism can be explained via rapid thermalization of generated hot carriers and transfer of their energies to strongly coupled optical phonons in a few hundred femtoseconds. Within a few picoseconds, anharmonic decay of optical phonons take place providing further cooling of electrons and optical phonons. So, the main relaxation process is based on the cooling of the coupled electron-phonon system.

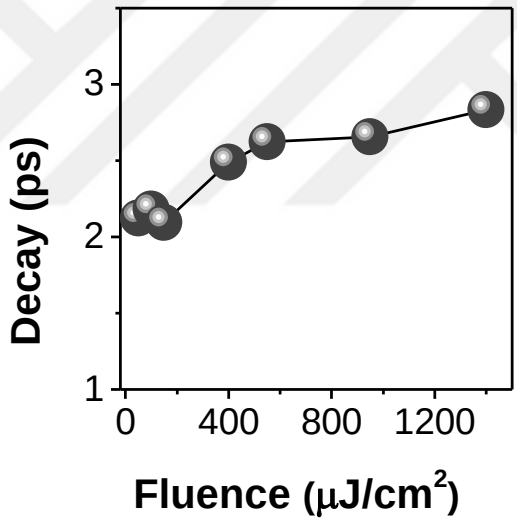

Figure 5.5. Decay times of the pump-induced THz response, extracted from Figure 5.3. (a) by fitting with single exponential function.

After photoexcitation, recovery of the signal was obtained in a few picoseconds. Figure 5.5 presents the fluence dependent change in decay times of differential signals, which were extracted by fitting to a single exponential decay function. Decay times change between 2-3 ps showing a very slight increase with pump fluence due

to increased carrier density and carrier heating, which result in enhanced carrier-carrier scattering resulting in reduction of carrier mobility and longer life times of free carriers. Sight increase in the decay times with fluence can also be a reflection of slower recombination of charges due to increased carrier density. Similar to our results, fast decay times were also reported in literature. However, our decay times changed between 2 to 3 ps rather than 1 to 2 ps[108,126] due to our high optical pump fluence compared to these studies. Our results indicate that the fluence is one of the important factor that affects the observed decay times of the samples.

5.5 THz Dynamics of MLG

In this part, carrier relaxation dynamics of MLG samples with varying layer numbers of 27, 49, 66, 69, 85, 100 on quartz, 32 layers on PE and 30 layers on PVC substrate were investigated with optical pump- THz probe experiments. For experiments, two different pump colors were chosen, which had center wavelengths of 800 nm and 400 nm. Firstly, the effect of pump pulses on the shape of the THz time domain signals were examined in order to figure out if 2D measurements were necessary. Figure 5.6 presents the results of time domain THz pulse profiles of 27-MLG with and without the effect of optical pump pulse preceding the peak of the THz pulse by 3.5 ps at 800 nm optical pump pulse. This time was chosen in order to eliminate the effect of photo induction on the initial transient response of THz pulse. Measurements were repeated for all MLG samples several times to ensure observed behavior was not affected by probable contaminants or defects in the MLG samples. The optical excitation caused decrease in the transmission of observed THz pulse while shape of it was not altered nor was it shifted in time for all MLG samples. This is an indication of flat dispersionless and almost entirely real conductivity with a negligible imaginary part due to high scattering rate of free charges of our MLG samples in the THz region.[137] Therefore, all pump probe measurements were based on 1D technique in which only the peak point of THz pulse was tracked as a function of pump-probe delay time rather than examining the full waveform.

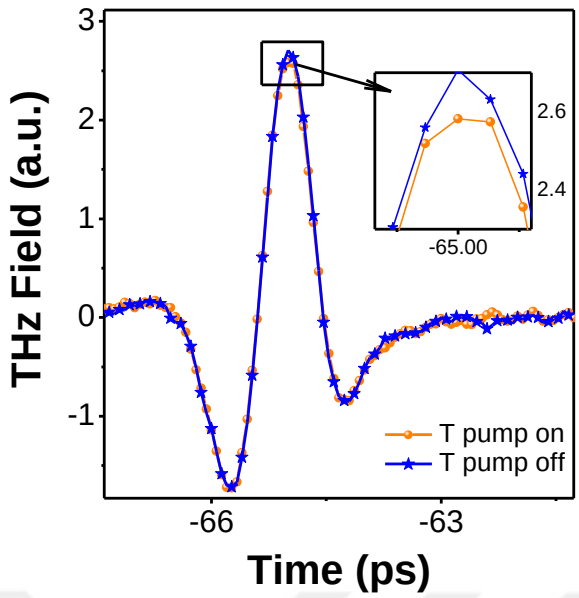

Figure 5.6. Measured THz time domain pulses transmitted through the 27-MLG sample without (blue, stars) and with (orange, circles) the presence of optical pump pulse preceding the peak of the terahertz pulse by ~3.5 ps.

5.5.1 THz Dynamics of MLG with 800 nm Optical Pump

After time domain characterizations, pump probe measurements were performed at selected fluencies of 50, 100, 150, 410, 520, 935, and 1430 μJ/cm^2 for MLG sample with 27 layers and 410 μJ/cm^2 (Explained in the following part) for other samples. Each measurement, which took approximately 15 minutes, was repeated for 10-15 times to increase the SNR of the results. Consistency between measurements were checked and stability and reliability of experimental conditions were assured.

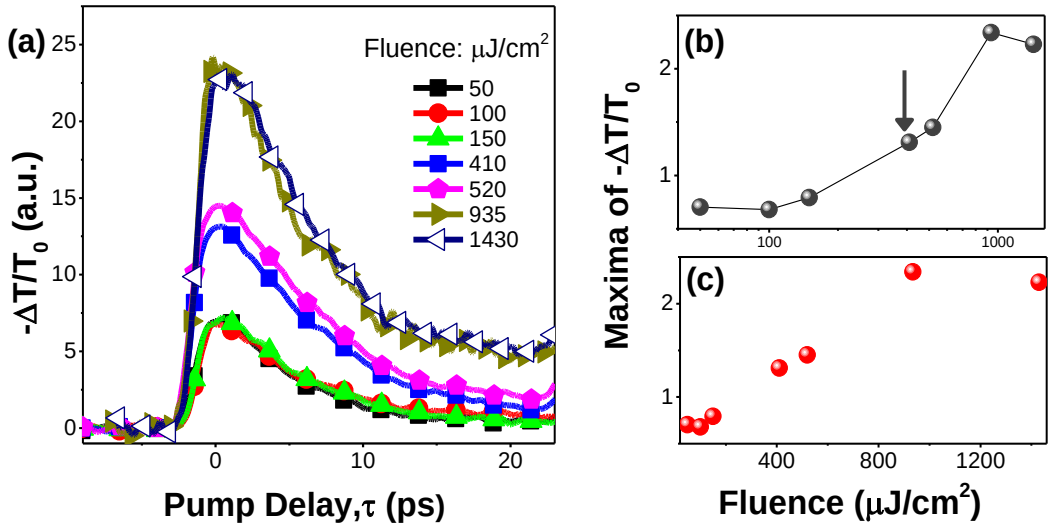

Figure 5.7. (a) Measured differential THz probe transmission -ΔT/T as a function of the pump probe delay time for 27-MLG is given at seven different applied fluencies of 800 nm optical pump pulse, (b) Maxima of the $\Delta T/T_0$ from part (a) as a function of applied fluence shown on log scale (c) The same data as in (b) shown on a linear scale.

Figure 5.7 (a) indicates the negative nature of differential transmission change in the amplitude ΔT/T of the transmitted THz probe pulse as a function of the relative pump probe delay time at 7 different fluencies for the same 27-MLG sample, which was chosen as representative for all the other MLG samples. This negative nature corresponds to a decrease in the THz transmission. Figure 5.7 (b) and (c) presents maxima of the time traces of $-\Delta T/T_0$ from part (a) as a function of applied fluence, which saturates at higher fluencies, shown on log and linear scale. Log scale reveals that 410 $\mu J/cm^2$ is the optimum fluence to stay in the linear region and observe maximum change in the differential signal. Therefore, the other MLG samples were pumped using this fluence to investigate the thickness dependent carrier relaxation dynamics.

Following the photoexcitation, the differential signal shows an increase on a time scale of ~0.5 ps, which is the rise time, limited by the resolution of our TRTS set up. The initial response of the signal corresponds to the creation of initial hot electron

hole pairs. The peak point of the signal, referring to a hot state with charges at elevated electron temperatures, leads to enhanced carrier-carrier scattering rate. Following this part, relaxation of signal takes place with a decay time of 5-9 ps (Fig.5.8) slightly increasing with increased fluence. Upon increasing the fluence, due to increased carrier density of charges, carrier-carrier scattering became less efficient which is reflected by saturation of signal at higher fluencies both indicated by Fig. 5.7 (b)-(c) and Fig. 5.8. Also faster decay times of low fluencies indicate that charges cool down quickly since a large amount of absorbed pump energy causes efficient and fast carrier carrier scattering.

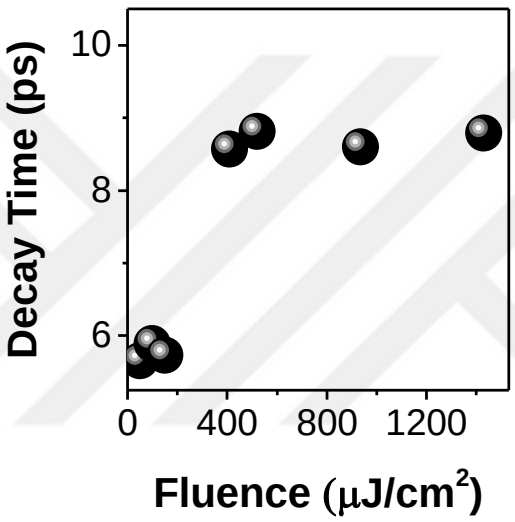

Figure 5.8. Decay times of the pump-induced THz response, extracted from Figure 5.7. (a) by fitting with single exponential function.

Figure 5.9. (a) shows the differential transmission $-\Delta T/T_0$ of the peak THz field as a function of the pump/probe delay time for all MLG samples with a pump fluence of 410 $\mu J/cm^2$. The effect of layer number on the charge carrier relaxation mechanisms of MLG samples is also presented with normalized version of differential transmission signal in Fig 5.9. (b) in order to emphasize the differences in the decay dynamics of samples clearly.

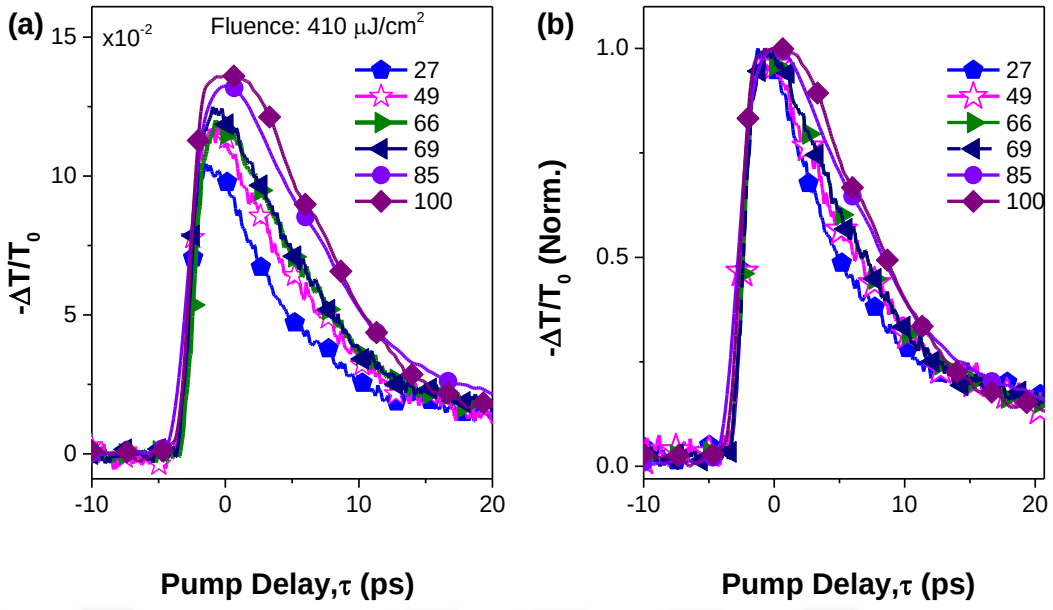

Figure 5.9. (a) The differential transmission $-\Delta T/T_0$ of the peak THz field as a function of the pump/probe delay time for various thicknesses at a fluence of 410 $\mu J/cm^2$ (b) Normalized version of part (a).

With increasing layer number, maxima of $-\Delta T/T_0$ signals also increase showing a roughly linear behavior (Fig. 5.10 (a)). This behavior can reflect that observed THz carrier dynamics is dominated by the top lightly doped layers at room temperature.

Following the optical pump excitation, at very initial times, a large population of carriers distribute themselves nonthermally which turn into termalization of them within 10-150 fs. After that, carriers cool down to a hot Fermi-Dirac distribution.[158] With the intraband carrier-phonon scattering, further cooling of thermalized carriers is provided. Time evolution of THz differential change exhibits two distinctive characters for all the MLG samples. Firstly, a relatively rapid recovery in transmission between 6 to 18 ps is observed depending on the layer number of MLG samples as shown in Fig. 5.10 (b). Beyond that time interval, slow recovery of the transmission reflects that dominant process is recombination of electron and holes determining the change in the THz conductivity. This process continues until almost 100 ps.

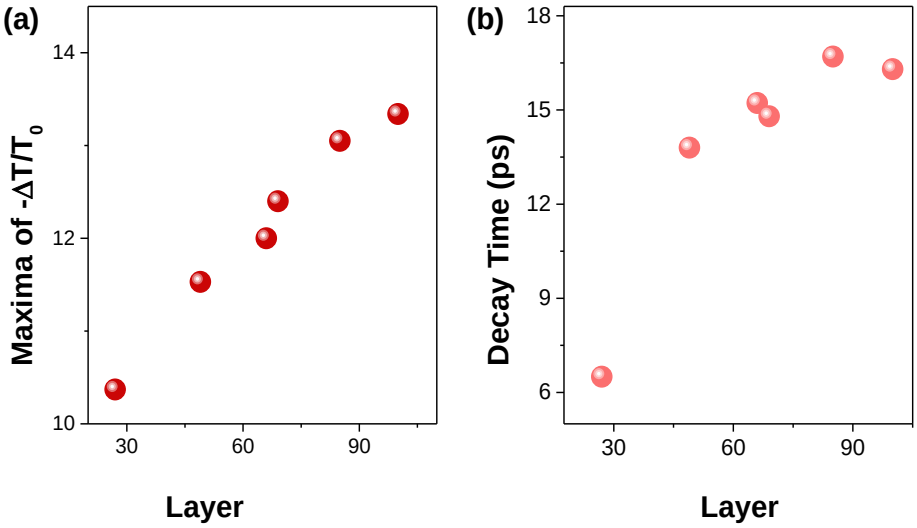

Figure 5.10. (a) Maxima of the time traces of $\Delta T/T_0$ from Fig. 5.9. (a) as a function of layer thickness, (d) Decay times of the pump-induced THz response, extracted from Fig. 5.9. (a) by fitting with single exponential function.

Long lived carrier behavior is shown for the thinnest (27 layer) and the thickest (100 layer) MLG samples (Fig.5.11 (a)). As normalized data (Fig. 5.11 (b)) presents more clearly, long lived carrier amount is slightly higher in MLG-100 than MLG-27 sample. Slower recombination of charges can be the reason of longer decay times. Slow recombination time stems from both increased number of charges, which causes inefficient carrier carrier scattering, and presence of inter layer transfers.

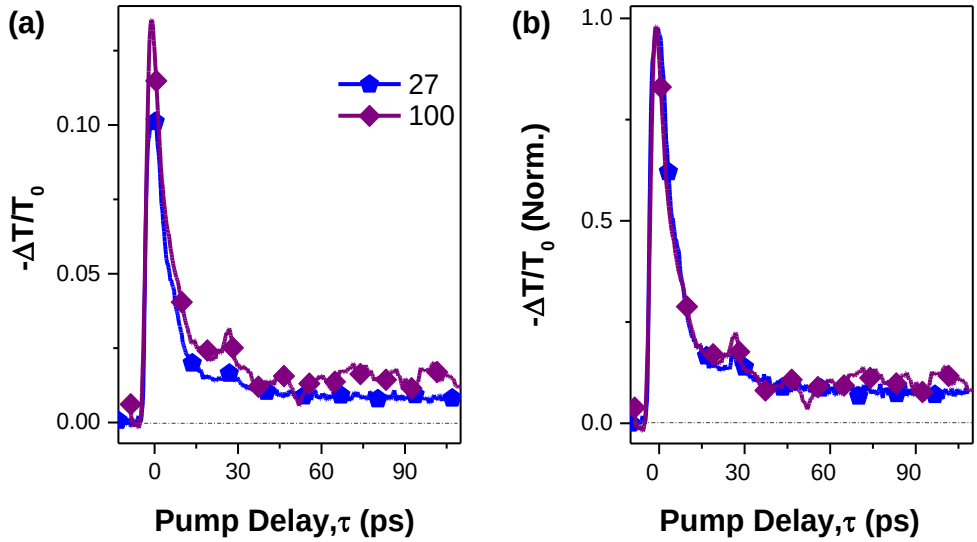

Figure 5.11. (a) Long scan results for MLG-27 and MLG -100 (b) Normalized version of part (a).

With increased number of layers, increase in diffusion of charges into different layers is expected. Therefore, it takes longer time for charges to recombine, which is also supported by faster relaxation dynamics of SLG due to nonexistent nature of interlayer interactions. The study by Mihnev et al.[147] reported higher decay times of approximately 4 ps compared to SLG, for two different graphene samples with 35 and 63 layers. Yet, it was suggested that decay times did not depend on the layer number at room temperature. However, our MLG samples showed a strong dependence of decay times to number of layers, which increases very sharply from 6 to 18 ps. Similar to SLG case, Mihnev et al.[147] reported an increase in decay times from 4-to-7 ps with increasing fluence (1-90 μJ/cm^2). Similarly, we have also observed an increase with fluence for our test MLG sample with 27 layers.

Extracted time evolution of dynamic conductivity, by using the relation between differential change and photoconductivity, for corresponding MLG samples is presented in Fig. 5.12 (a) in units of universal conductivity, G_0. Magnitude of the dynamic conductivity depends on intraband scattering of charges, which in return is determined by Fermi energy level and momentum relaxation times of MLG samples.

Layer dependent increase in photoinduced conductivity reflects the existence of a higher amount of free charge carriers in thick samples. This stems from slower recombination times of charges due to increased inter layer transfers.

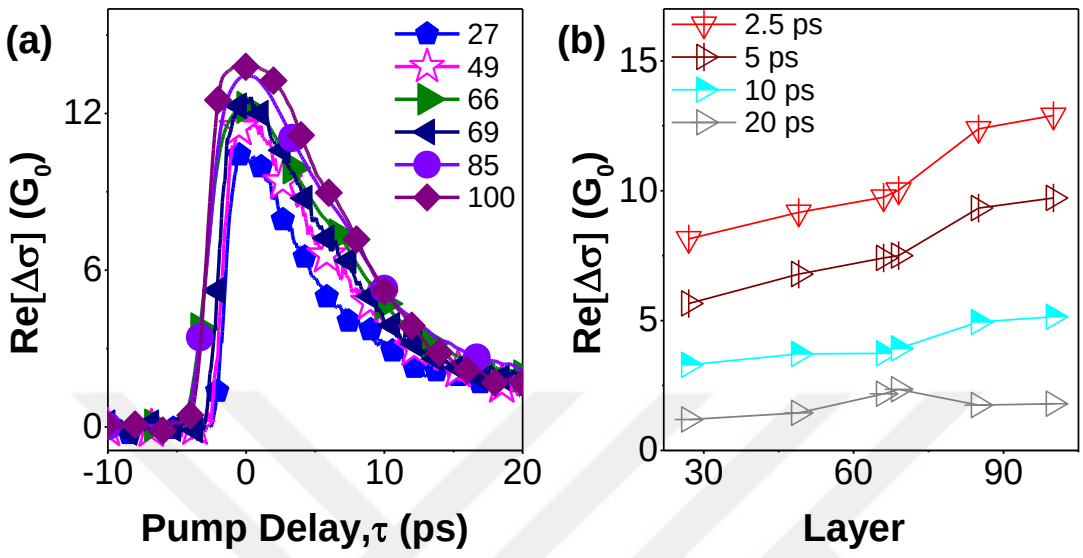

Figure 5.12. (a) Evolution of the real part of photoinduced THz conductivity as a function of delay time between the 800 nm pump and the THz probe, (b) Time dependent change in Δσ with layer number.

Figure 5.12 (b) shows the change in photo induced conductivity with layer number at specific probe delay times of 2.5, 5, 10 and 20 ps. At delay times of 2.5 and 5 ps, change in Δσ with increasing layer number is obvious calculated as 36.8 and 41.8 %. However, at later times it seems like there is little or almost no change in conductivity with increasing layer number. To clearly present differences in the photoinduced conductivity, % conductivity difference between 27 and 100 layers of graphene at specific delay times is compared as shown in Table 5.1.

Table 5. 1. % Conductivity difference between 27 and 100 layers of graphene at specific delay times.

Decay Time (ps)	$[(\Delta\sigma_{100}-\Delta\sigma_{27})/\Delta\sigma_{100}]$ %
2.5	36.8
5	41.8
10	35.9
20	61

Even after 20 ps, there is a large difference in conductivities of MLG-27 and MLG-100 reflecting the nature of layer dependency of photoinduced conductivity at room temperature.

5.5.2 THz Dynamics of MLG with 400 nm Optical Pump

THz relaxation dynamics of MLG samples were also investigated with 400 nm optical pump. Figure 5.13 (a) indicates the differential transmission $-\Delta T/T_0$ of the peak THz field as a function of the pump/probe delay time for all samples. Negative change in the differential transmission of THz signal corresponds to a positive photoinduced conductivity. Normalized version of $-\Delta T/T_0$ as a function of pump probe delay time is given in Fig. 5.13 (b) showing relaxation dynamics of samples are quite similar at room temperature. Relaxation mechanism can be explained via rapid thermalization of generated hot carriers and transfer of their energies to strongly coupled optical phonons in a few hundred femtoseconds.[159] Within a few picoseconds, anharmonic decay of optical phonons take place providing further cooling of electrons and optical phonons. So, the main relaxation process depends on the cooling of the coupled electron-phonon system.[108] Figure 5.13 (c) presents peak points of the $-\Delta T/T_0$ signal as a function of layer thickness. On the contrary to 800 nm pump responses (Fig.5.10 (a)), we observe a decrease at the peak points of differential signals with applied 400 nm pump depending on the layer number. Although pump creates a corresponding positive photoinduced conductivity in all the MLG samples, thicker samples

experience a suppressed increase in contrast to 800 pump case where the thickest sample has the highest conductivity change.

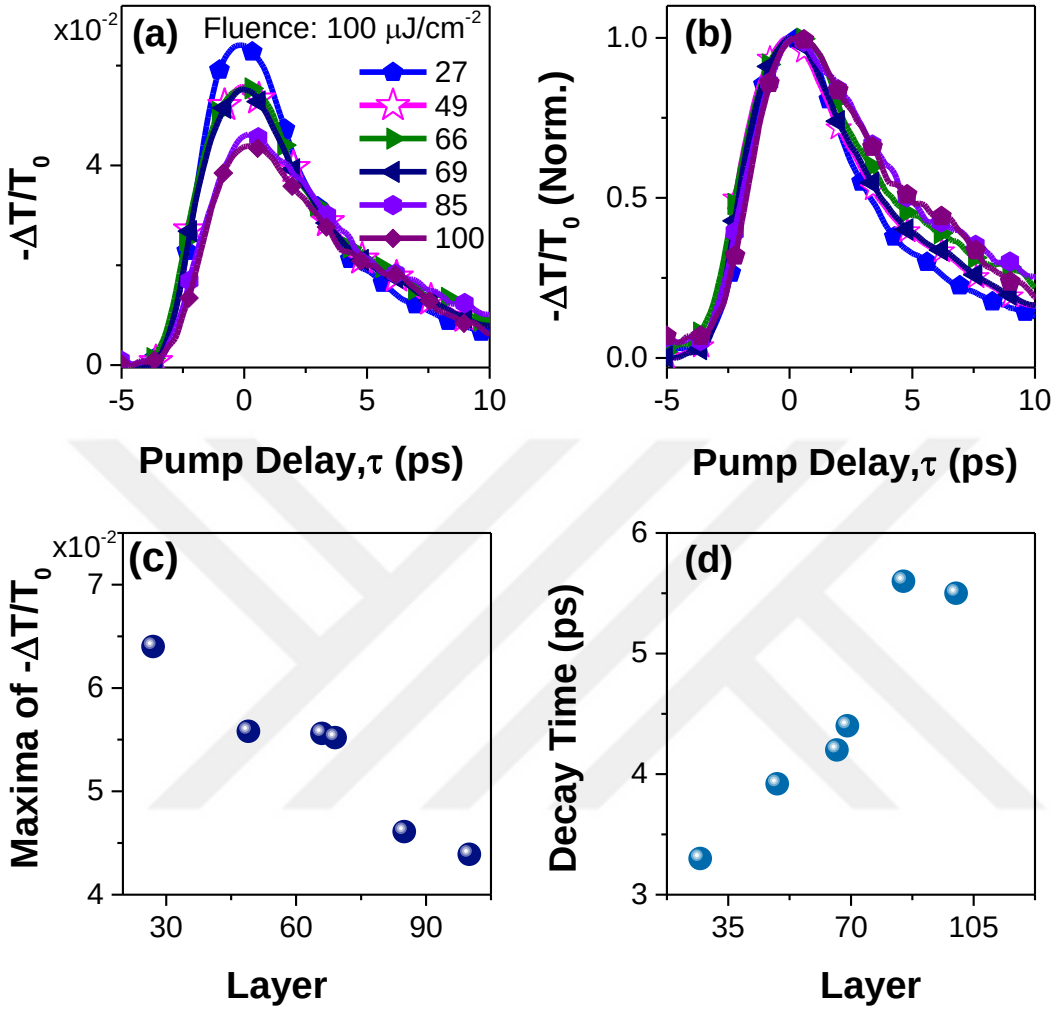

Figure 5.13. (a) The differential transmission $-\Delta T/T_0$ of the peak THz field as a function of the pump/probe delay time, for various thicknesses, (b) Normalized version of part (a), (c) Maxima of the time traces of $\Delta T/T_0$ from part (a) as a function of layer thickness, (d) Decay times of the pump-induced THz response, extracted from part (a) by fitting with single exponential function.

Excitation conditions and physical properties of graphene sample such as doping level and mobility determine its photoinduced conductivity character. 400 nm pump

provides highly energetic excitation condition with its 3.1 eV photons. The study of Tielrooij shows theoretically, in 400 nm excitation case, one photon causes creation of nine additional hot carriers with the promotion from below to above of Fermi energy level in the conduction band.[160] Carrier population is much more higher in thick samples and such an increased free carrier population can cause less absorption of THz resulting in a relatively small photoinduced conductivity change. As explained before, highly doped samples, with Fermi energy levels away from the Dirac point, can show transient decrease in the THz conductivity. This can be explained with the generation of secondary hot electrons due to interaction of hot carriers with already existing ones because of enhanced carrier-carrier scattering. This situation, which is also observed in our highly doped SLG sample, may explain the less increase in photoinduced conductivity with increased layer number.

Figure 5.13 (d) presents the extracted decay times of MLG samples by fitting with single exponential function. Decay times change slightly between 3 to 6 ps. Although a slight increase in decay time is observed at first, then a saturation behavior is detected with increasing layer number. Increase in decay time with layer number can be explained with slower recombination due to inter layer transfers.

Furthermore, quite short nature of decay times, compared to 800 nm pump dynamics which vary between 6-18 ps, indicate that samples are highly doped in 400 nm case. Shorter decay times stem from the reduced efficiency of carrier–carrier scattering due to increased carrier density.

5.5.3 Comparison of 800 nm and 400 nm Pump-THz Probe Dynamics

We further analyze the THz carrier relaxation dynamics proceeding with the examination of the effect of increasing the photon energy at a fixed absorbed photon density for the MLG-27 sample, chosen as a representative sample for all the other MLG samples.

As Figure 5.14 (a) presents 400 nm pump causes a larger differential transmission signal at the peak even though photon densities are normalized. The origin of this larger transmission change can be stemming from separate or combined effects of multiple free charge creation effect of 400 nm pump or high mobilities of created charges that provide larger conductivity change. Figure 5.14 (b) shows the normalized version of differential transmission signals in order to emphasize the differences in the carrier relaxation dynamics. Similar behavioral difference with 400 nm and 800 nm pump was also observed in the study of Tielrooij et al.[140]

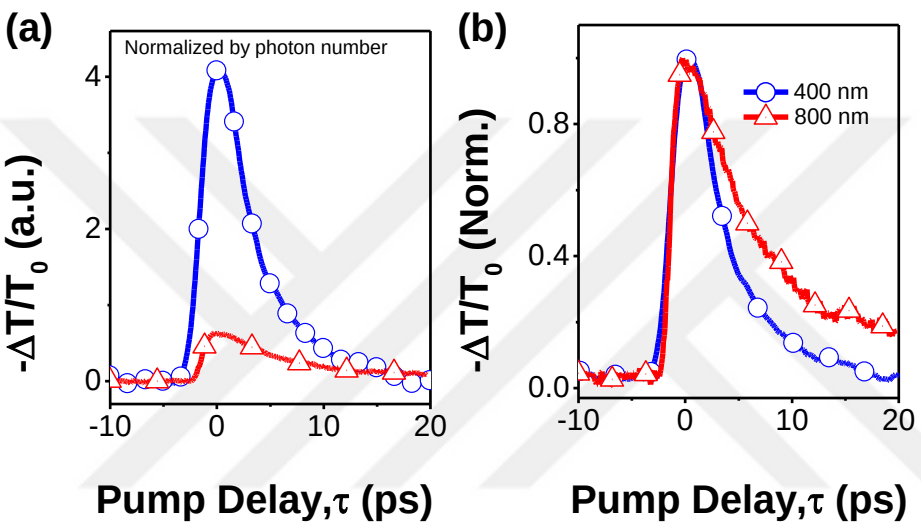

Figure 5.14. (a) Comparison of the differential transmission $-\Delta T/T_0$ of the peak THz field as a function of the 400 nm and 800 nm pump/probe delay time, for 27 layer MLG, (b) Normalized version of part (a).

Immediately after pump effect, thermalization of carriers take place and cooling can occur through carrier carrier scattering as the main relaxation mechanism for both optical pump cases. Measurable initial time interval reveals that carrier phonon interactions are inefficient in the observed cooling dynamics since they would cause a photon energy independent normalized signal [140] . Decay times of responses were extracted with fitting to a single exponential decay function and results are presented in Table 5.2.

Table 5. 2. Extracted decay times of the pump-induced THz response by fitting with single exponential function.

Quartz MLG-27 Pump (nm)	Decay Time (ps)
800	6.5±0.009
400	3.3±0.05

Compared to SLG dynamics, hot carrier cooling lasts for longer time intervals, few picoseconds, for both cases due to density and distribution of carriers since sample has 27 layers. Decay time of 800 nm pump signal is almost 2 times higher than the 400 nm pump case. Faster initial decay of 400 nm pump THz probe dynamics is expected due to hotter distribution of carriers with high kinetic energy, mobility and conductivity leading to enhanced carrier-carrier scattering. Moreover, these highly energetic carriers can easily overcome interlayer potential barriers, even they may behave like they are in a 3D environment. This situation leads to increase in recombination rate of charges supporting the initial fast decay behavior compared to 800 nm case. Slower recombination times of charges, created by 800 nm pump, is observed more clearly at longer times because of the decreased probability of effective carrier carrier scattering caused by inter layer transfers.

5.6 THz dynamics of MLG samples on PE and PVC Substrates

Graphene's electrical conductivity and mobility is strongly affected by the chemical nature and properties of substrate material. In order to also see the effect of substrate on the THz charge carrier dynamics, two different substrates, PE and PVC are chosen.

PE MLG sample had 32 layers. Static conductivity characterization of sample with THz-TDS revealed the frequency dependent behavior of charges with a scattering rate of 0.82 THz. Conductivity behavior was explained with Drude Smith model which

accounts for the long life times of charges stemming from decreased mobilities due to disordered nature of the PE MLG 32 sample.

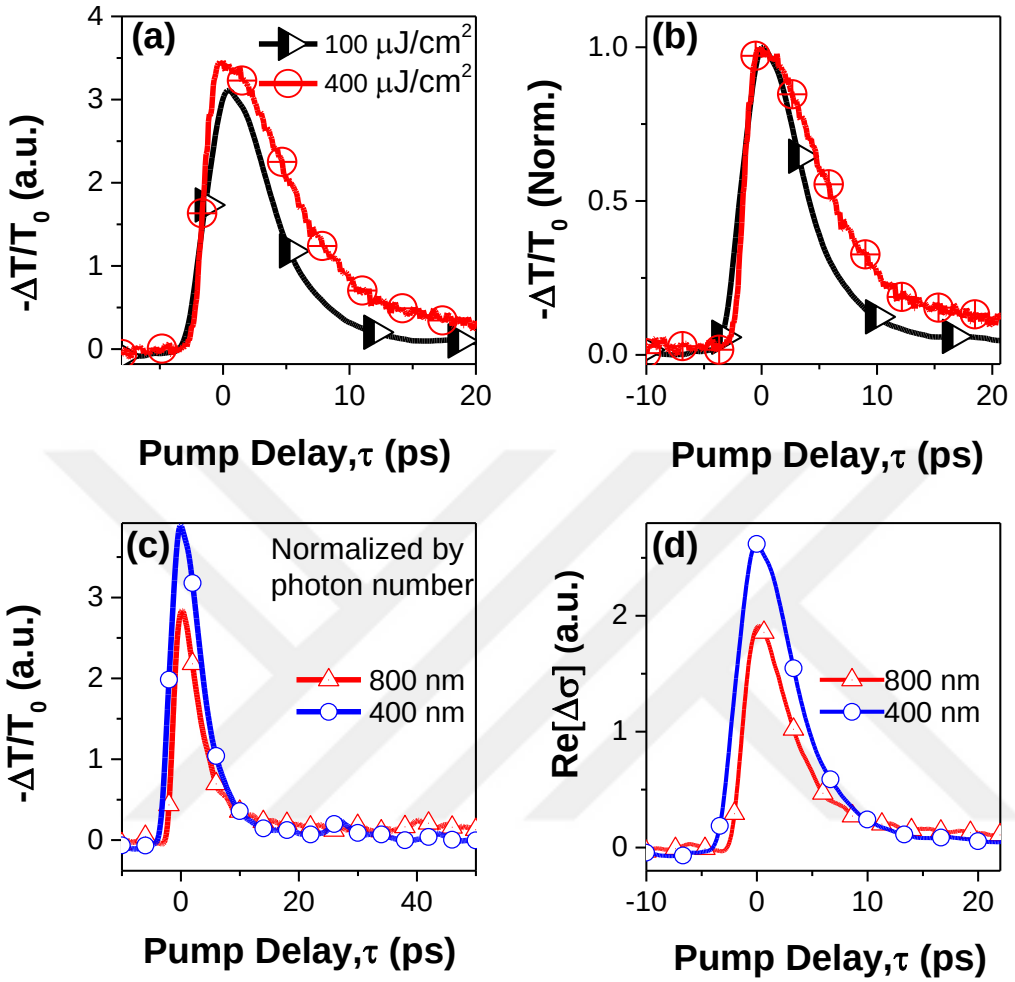

Figure 5.15. (a) The differential transmission $-\Delta T/T_0$ of the peak THz field as a function of the 800 nm optical pump/probe delay time, for 100 and 400 μJ/cm^2, (b) Normalized version of part (a), (c) Comparison of the photon number normalized differential transmission $-\Delta T/T_0$ of the peak THz field as a function of the 400 nm and 800 nm pump/probe delay time for PE MLG-32, (d) Evolution of the real part of photo induced THz conductivities as function of delay time between 800 nm pump -THz probe and 400 nm pump -THz probe.

Pump probe experiments were done at two different pump colors which were 800 and 400 nm. 800 nm pump studies included two different fluencies which were 100 and 400 μJ/cm^2. Figure 5.15 (a) indicates the negative nature of differential transmission $\Delta T/T_0$ of the peak THz field as a function of the 800 nm optical pump/probe delay time, for 100 and 400 μJ/cm^2 pump fluencies. The negative differential change, corresponding to positive photo induced conductivity, increases with increased pump fluence. This scaling with increased pump fluence is a strong signature of the dominance of carrier-carrier scattering as initial cooling mechanism. Normalized form of the signals illustrate the difference in their decay times (Fig. 5.15 (b)). Extracted decay times by fitting with single exponential decay function are given in Table 5.3. Decay time is higher for 400 μJ/cm^2 pump fluence, as it is expected. With increased pump fluence, inter layer transfers increase and efficient carrier-carrier scattering is hindered leading to slower recombination times.

Table 5. 3. Extracted decay times of the pump-induced THz response by fitting with single exponential decay function.

PE MLG 32 800 nm Pump Fluence	**Decay Time (ps)**
100 μJ/cm^2	4.35±0.10
400 μJ/cm^2	6.94±0.07

Effect of increasing photon energy, at a fixed absorbed photon density, on THz carrier relaxation dynamics for the PE MLG-32 sample is given in Fig. 5.15 (c). 400 nm pump causes a larger differential transmission signal due to both hotter carrier distribution and higher number of created charge carriers. Faster initial decay of 400 nm pump THz probe dynamics is expected due to hotter distribution of carriers with high kinetic energy, mobility and conductivity leading to enhanced carrier-carrier scattering. Moreover, these highly energetic carriers can easily overcome interlayer potential barriers, and behave like they are in a 3D environment. This leads to increase in recombination rate of charges supporting the initial fast decay behavior compared

to 800 nm case. Also effect of slower recombination on decay dynamics of 800 nm pump case can be seen at longer times due to inter layer transfer of charges.

Figure 5.15 (d) shows the evolution of the real part of photo induced THz conductivities as function of delay time for both 800 nm and 400 nm optical pump case. In order to better compare the conductivity behavior, results are given at specific times of 2.5, 5, 10, 20 ps as illustrated in Table 5.4.

Table 5. 4. Time dependent conductivity comparison of 800 and 400 nm optical pump studies for PE MLG 32.

Δσ				
PE MLG 32 Pump	**Delay Time τ (ps)**			
	2.5	5	10	20
800 nm	1.26	0.64	0.25	**0.125**
400 nm	1.91	0.91	0.29	**0.053**

At initial times, change in the photo induced conductivity caused by 400 nm pump is higher. Observed high conductivity can be attributed to presence of highly energetic carriers with elevated kinetic energy and mobilities. As the time proceeds, due to fast cooling and higher recombination rates of hot carriers compared to 800 nm pump, conductivity change becomes lower. Therefore, change in the photo induced conductivity caused by 800 nm pump gets closer to 400 nm pump case. Finally, at 20 ps, 800 nm pumped case gives higher conductivity value due to existence of higher number of long lived carriers.

In order to get some idea about the effect of substrate on charge carrier dynamics, results of PE MLG 32 sample was compared with quartz MLG 27 sample. 800 nm optical pump with approximately 400 $\mu J/cm^2$ fluence created similar relaxation dynamics on both samples. Decay times, extracted from fitting by single exponential function, also supported the similarity (as 6.94 and 6.5 ps for PE and quartz MLG

samples). However, when 400-800 nm pump comparison is analyzed separately, it is seen that in quartz MLG 27 sample, 400 nm pump created a more pronounced change at the peak of the differential transmission signal (Fig. 5.14 (a)). As it is explained before, 400 nm pump, due to its high energy photons, can create multiple charges which is the main reason of observed difference at the peak point. On the other hand, less pronounced response of PE MLG 32 sample (Fig. 5.15 (c)) could be stemming from more doped nature of PE substrate compared to quartz.

The other sample, PVC MLG had 30 layers. Static conductivity characterization of sample with THz-TDS revealed the frequency dependent behavior of charges with a scattering rate of 0.64 THz. Conductivity behavior was explained with Drude Smith model which accounts for the long life times of charges caused by decreased mobilities due to disordered nature of the PVC MLG 30 sample.

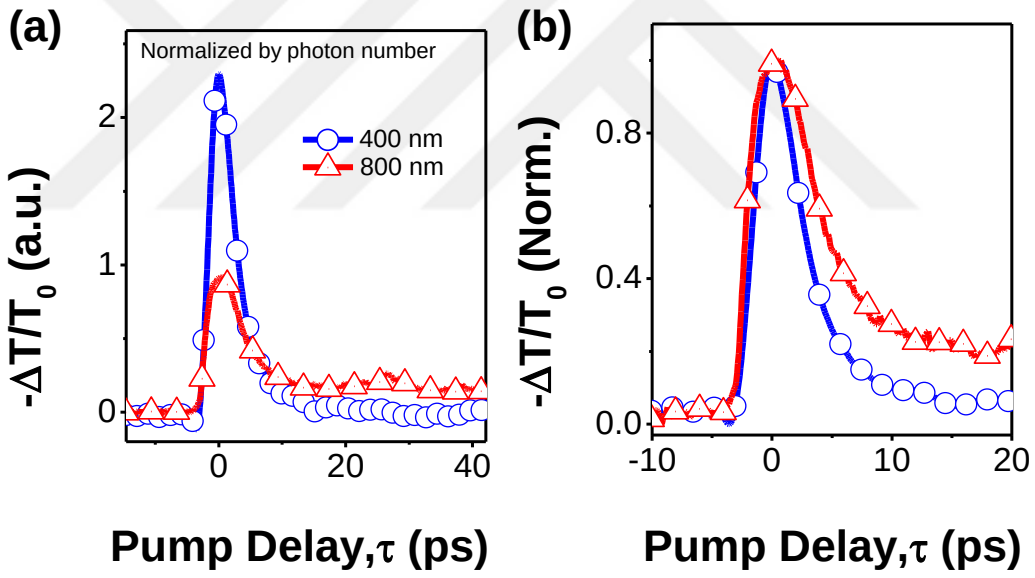

Figure 5.16. (a) Comparison of the photon number normalized differential transmission $-\Delta T/T_0$ of the peak THz field as a function of the 400 nm and 800 nm pump/probe delay time for PVC MLG-30, (b) Normalized version of part (a).

Comparison of 800 nm and 400 nm optical pump effect, at a fixed photon number, on THz relaxation dynamics of the PVC MLG-30 sample is given in Fig. 5.16 (a). Both pump color causes an increase in photo induced conductivity reflected by negative nature of differential transmission signal. As it is clearly seen, 400 nm pump causes a larger differential transmission signal at the peak as it is expected. Figure 5.16 (b) presents the normalized form of the differential transmission signals to better emphasize the observed relaxation dynamics difference. Extracted decay times by fitting with single exponential decay function (Table. 5.5) shows that 800 nm pumped case has a decay time of approximately 5.3 ps which is almost twice the 400 nm case.

Table 5. 5. Extracted decay times of the pump-induced THz response by fitting with single exponential decay function.

PVC MLG 30 Pump	Decay Time (ps)
800	5.3±0.046
400	2.8±0.007

Faster initial decay of charges in 400 nm pumped case stems from enhanced carrier carrier scattering which is a result of hot carriers with high kinetic energy, mobility and conductivity. Moreover, hot carriers can easily overcome energy barriers between layers leading to increased interlayer transfers and also faster recombination rates compared to 800 nm pump case.

Figure 5.17 shows the evolution of the real part of photo induced THz conductivities as function of delay time for both 800 nm and 400 nm optical pump case.

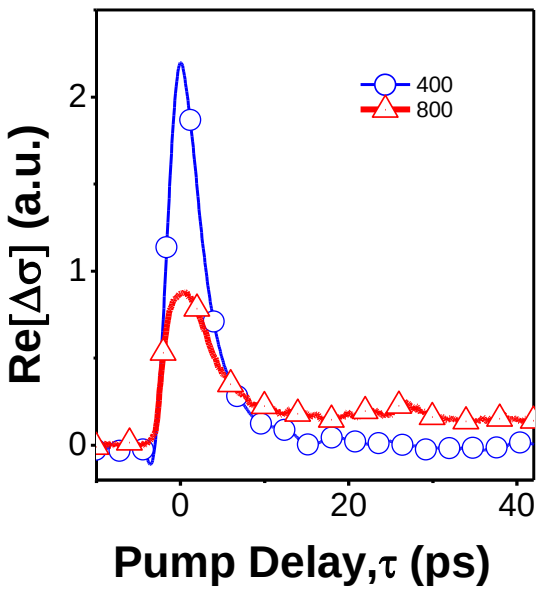

Figure 5.17. Evolution of the real part of photo induced THz conductivities as function of delay time between 800 nm pump -THz probe and 400 nm pump -THz probe.

For better comparison of the conductivity behavior, results are given at specific times of 2.5, 5, 10 and 20 ps as indicated in Table 5.6. At initial times change in the conductivity of 400 nm pump case is higher. However, difference gets lower and finally at 10 ps, 800 nm pumped dynamics results in higher conductivity.

Table 5. 6. Time dependent conductivity comparison of 800 and 400 nm optical pump studies for PVC MLG 30.

Δσ				
PVC MLG 30 Pump	**Delay Time τ (ps)**			
	2.5	5	10	20
800 nm	0.71	0.41	**0.22**	**0.18**
400 nm	1.22	0.49	**0.12**	**0.03**

Observed high conductivity of 400 nm pump case at initial times can be attributed to presence of highly energetic carriers with elevated kinetic energy and mobilities. As the time proceeds, due to faster recombination of hot carriers compared to 800 nm pumped case, conductivity change becomes lower.

Effect of substrate on charge carrier dynamics were examined with the comparison of PVC MLG 30 to quartz MLG 27 sample. 800 nm optical pump with approximately 400 $\mu J/cm^2$ fluence created similar relaxation dynamics on both samples. Decay times, extracted from fitting by single exponential function, also supported the similarity (as 5.3 and 6.5 ps for PVC and quartz MLG samples). When 400-800 nm pump results are analyzed separately, it is seen that in quartz MLG 27 sample, 400 nm pump created a more pronounced change at the peak of the differential transmission signal (Fig. 5.14 (a)). In this case also, smaller change observed in the transmission peak (Fig. 5.16 (a)) can be attributed to more doped nature of PVC substrate compared to quartz similar to PE MLG 32 sample.

5.7 Conclusion

In Chapter 5, we have presented the THz relaxation dynamics of SLG and MLG samples on quartz, PE and PVC. SLG sample indicated increase in THz transmission following the application of 800 nm optical pump pulse which corresponded to a negative photo induced conductivity. This behavior is explained with metallic character of this specific SLG sample due to its high carrier density. Fluence dependent pump THz probe dynamics showed that peak point of observed transmission change increased with increasing fluence proving the dominance of carrier-carrier scattering as initial cooling mechanism.

MLG samples with 27, 49, 66, 69, 85 and 100 layers on quartz substrate were excited both with 800 and 400 nm pump colors. Firstly, the most efficient pump intensity for 800 nm was determined by examining the fluence dependent behavior of MLG-27. Relaxation dynamics of all samples were investigated with a fluence of 410 $\mu J/cm^2$

in order to stay in linear regime and see the maximum change in differential transmission signal. All the samples showed similar initial responses which can be explained as hot carrier cooling via carrier-carrier scattering and carrier-phonon scattering. Thickness dependent THz dynamics revealed the existence of interlayer charge transfers suggested by slower decay times of thick samples due to slower recombination effects. 400 nm pump studies of samples exhibited different optical pump induced behavior, in terms of decrease of peak points of differential signals with increasing layer number, on the contrary to 800 nm case. This situation is explained with high carrier densities of thick samples which leads to enhanced carrier-carrier scattering and faster recombination at initial times. Decay times of samples changed between 3-6 ps depending on the thickness which were quite short compared to 800 nm case due to initial hot carrier cooling and fast recombination rates of charges stemming from existence of considerable interlayer transfer of charges.

Further analysis of pump color and intensity dependent relaxation dynamics of MLG samples revealed that a hotter distribution of carriers can be achieved either by increasing the absorbed photon density or photon energy. As a result, 400 nm pump created a larger change in the observed differential transmission signal corresponding to faster initial decay times and higher values of initial dynamic conductivity compared to 800 nm pump dynamics.

PE MLG with 32 layers and PVC MLG with 30 layers were also both examined with 800 and 400 nm optical pump. Similar pump intensity and color dependent THz relaxation dynamics were observed with less pronounced effect of 400 nm pump on the peak point of differential change. This was attributed to more doped structures of PE and PVC compared to quartz. Substrate choice is significant since it can drastically affect the observed mobility and conductivity of graphene samples by creating additional parallel channels for carrier cooling. PE and PVC can also be good choices for graphene based flexible optoelectronic devices due to their experimental performance.

Experimental measurement of photoinduced conductivity is valuable since it gives us a macroscopic quantity, which is useful in terms of design and development of graphene based electronics.

CHAPTER 6

CONCLUSION

Improvements in technology have also led to enhanced THz spectroscopy systems due to more stable ultrafast lasers, effective THz generation and detection techniques. These systems have high potential in terms of their versatility in a wide array of applications and material characterization. Therefore, construction of THz spectrometers are significant to be able to investigate topics that will benefit improvements in technology and contribute to research regarding fundamental topics.

The main aim of this study has been the design, construction and characterization of THz-TDS and TRTS systems which are described in detail in Chapter 2. Firstly, THz-TDS was completed after working on it quite some time, learning the precise alignment procedures, and getting experienced on ultrafast laser systems. After that, TRTS, which is a first in Turkey to our knowledge, was built. Our experiments were followed by optimization studies to improve the performance of the built systems, and achieve better SNR ratios. Our THz spectroscopy systems are quite sophisticated in terms of the employed amount of optical components and utilization of 5 different ultrafast lasers. Since spectroscopy systems depend on the stability of lasers, collecting data becomes quite challenging given the inherent laser stability issue. Therefore, working with such sophisticated optical systems require not only achieving the system performance that will provide collection of data, but also careful examination of them to be able to extract meaningful results. Additionally, developing data processing methods that will provide accurate analysis of data has been a significant part of this study. After systems were completed, studies were carried out with applications of graphene.

Chapter 3 involves characterization of the SLG and four different MLG THz modulators by THz-TDS. Although SLG device almost gave 50 % modulation within the voltage durability of device, MLG based devices with 30, 60, 100 layers on PVC and PE substrate demonstrated almost complete and broadband modulation in THz transmission between 0.2 and 1.5 THz. Study offered a simple device design, which benefited from the relatively new usage of ionic dopant molecules, and very low operation voltages from 0 V to 3.4 V. Extraordinary performance of these devices make them promising candidates in the applications of THz active filters, which are urgently needed for the improvement of THz optoelectronic devices.

Chapter 4 have presented characterization of THz sheet conductivities of eight different large-area CVD samples with THz-TDS measurements. After THz-TDS measurements, conductivities were calculated with the usage of thin film approximation. In order to explain calculated conductivities of SLG and MLG samples, either Drude or Drude-Smith model were employed, and behaviors were described well. Observed differences in the SLG samples, one on quartz and the other on PVC, may have stemmed from growth and transfer process since the quality of graphene films are strongly affected by both. Furthermore, quartz and PVC substrates has different natures, and this might have affected the observed difference in the conductivity behavior of our SLG samples. THz sheet conductivities of MLG samples were separated into two categories. Conductivities of thinner samples exhibited slight increase with increasing frequency, and they were explained with DS model. Thicker samples exhibited a slight decrease in conductivity with increasing frequency, which were well accounted for with Drude model. MLG samples exhibited a very pronounced increase in THz sheet conductivities with increasing layer number. This superior sheet conductivity compared to SLG samples suggests that MLG can be a promising platform for novel THz optoelectronic applications. Overall, our THz-TDS system has proved itself to be a noncontact and reliable technique that allows characterization of frequency dependent sheet conductivity for both SLG and MLG samples.

In Chapter 5, we have presented the THz relaxation dynamics of SLG and MLG samples on quartz, PE and PVC. Experiments were done with TRTS system with the usage of 800 and 400 nm optical pump colors. Following the pump pulse, absorption of photons led to creation of hot carriers resulting in a non-equilibrium condition, which was effectively probed by THz pulses. Non-thermal (out of equilibrium) distribution of carriers were followed by relaxation of hot carriers with realization of thermal equilibrium with the lattice. At initial times, main relaxation mechanisms were carrier carrier scattering and carrier phonon scattering. SLG sample indicated a negative photo induced conductivity with 800 nm pump due to its high carrier density. Fluence dependent pump THz probe dynamics pointed out the dominance of carrier-carrier scattering as initial cooling mechanism. 800 nm pump results of MLG samples, with 27, 49, 66, 69, 85 and 100 layers on quartz substrate, revealed the existence of interlayer charge transfers suggested by slower decay times of thick samples due to slower recombination effects. 400 nm pump studies of samples showed shorter decay times compared to 800 nm case due to initial hot carrier cooling and fast recombination rates of charges stemming from existence of considerable interlayer transfer of charges. PE MLG with 32 layers and PVC MLG with 30 layers were also both examined with 800 and 400 nm optical pump. Similar pump intensity and color dependent THz relaxation dynamics were observed. Difference in the responses of 400 nm pump of PE 32, PVC 30 compared to quartz 27 MLG could be stemming from more doping nature of PE and PVC substrates.

REFERENCES

1. Fattinger, Ch., Grischkowsky, D. Point source terahertz optics. *Appl. Phys. Lett.* **53,** 1480–1482 (1988).
2. Ho, L. & Pepper, M. Signatures and fingerprints. **2,** 541–543 (2008).
3. Davies, A. G., Linfield, E. H., & Johnston, M. B. The development of terahertz sources and their applications. *Phys. Med. Biol.* **47,** 3679–3689 (2002).
4. Hafez, H. A., Chai, X., Ibrahim, A., Mondal, S., Férachou, D., Ropagnol, X., & Ozaki, T. Intense terahertz radiation and their applications. *J. Opt.* **18,** 93004 (2016).
5. Ugawa, A., Ishii, H., Yakushi, K., Okamoto, H., Mitani, T., Watanabe, M., Sakai, K., Suzui, K., & Kato, S. Design of an instrument for far-infrared microspectroscopy using a synchrotron radiation source. *Rev. Sci. Instrum.* **63,** 1551–1554 (1992).
6. Auston, D. H., Cheung, K. P., & Smith, P. R. Picosecond photoconducting Hertzian dipoles. *Appl. Phys. Lett.* **45,** 284–286 (1984).
7. Reklaitis, A. Comparison of Efficiency of GaAs-based pulsed terahertz emitters. *J. Appl. Phys.* **101,** 116104 (2007).
8. Reimann, K. Table-top sources of ultrashort THz pulses. *Reports Prog. Phys.* **70,** 1597–1632 (2007).
9. Kitaeva, G. K. Terahertz generation by means of optical lasers. *Laser Phys. Lett.* **5,** 559–576 (2008).
10. Jepsen, P. U., Cooke, D. G., & Koch, M. Terahertz spectroscopy and imaging - Modern techniques and applications. *Laser Photonics Rev.* **5,** 124–166 (2011).

11. Miyamaru, F., Saito, Y., Yamamoto, K., Furuya, T., Nishizawa, S., & Tani, M. Dependence of emission of terahertz radiation on geometrical parameters of dipole photoconductive antennas. *Appl. Phys. Lett.* **96,** 1–4 (2010).

12. Vicario, C., Ovchinnikov, A. V., Ashitkov, S. I., Agranat, M. B., Fortov, V. E., & Hauri, C. P. Generation of 09-mJ THz pulses in DSTMS pumped by a Cr:Mg2SiO4 laser. *Opt. Lett.* **39,** 6632–6635 (2014).

13. Tomasino, A., Parisi, A., Stivala, S., Livreri, P., Cino, A. C., Busacca, A. C., Peccianti, M., & Morandotti, R. Wideband THz Time Domain Spectroscopy based on Optical Rectification and Electro-Optic Sampling. *Sci. Rep.* **3,** 3116 (2013).

14. Han, P. Y., Tani, M. , Usami, M., Kono, S., Kersting, R., Zhang, X. C. A direct comparison between terahertz time-domain spectroscopy and far-infrared Fourier transform spectroscopy. *J. Appl. Phys.* **89,** 2357–2359 (2001).

15. Sharma, G., Singh, K., Ibrahim, A., Al-Naib, I., Morandotti, R., Vidal, F., & Ozaki, T. Self-referenced spectral domain interferometry for improved signal-to-noise measurement of terahertz radiation. *Opt. Lett.* **38,** 2705–2707 (2013).

16. Gallot, G. & Grischkowsky, D. Electro-optic detection of terahertz radiation. *J. Opt. Soc. Am. B* **16,** 1204 (1999).

17. Lee, Y. S. Principles of Terahertz Science and Technology. *Springer* (2009).

18. Ferguson, B. & Zhang, X. Materials for terahertz science and technology. *Nat. Mater.* **1,** 26–33 (2002).

19. Musienko, T., Rudakov, V., Solovev, L. On the application of Kramers-Kronig relations to media with spatial dispersion. *J. Phys. Condens. Matter* **1,** 6745–6753 (1989).

20. Auston, D. H., Cheung, K. P., Valdmanis, J. A., & Kleinman, D. A. Cherenkov Radiation from Femtosecond Optical Pulses in Electro-Optic Media. *Phys. Rev. Lett.* **53,** 1555–1558 (1984).

21. Grischkowsky, D., Keiding, S., van Exter, M., & Fattinger, C. Far-infrared time-domain spectroscopy with terahertz beams of dielectrics and semiconductors. *J. Opt. Soc. Am. B* **7,** 2006 (1990).

22. Scheller, M. Data Extraction from Terahertz Time Domain Spectroscopy Measurements. *J. Infrared, Millimeter, Terahertz Waves* **35,** 638–648 (2014).

23. Bernier, M., Garet, F., & Coutaz, J. L. Precise determination of the refractive index of samples showing low transmission bands by THz time-domain spectroscopy. *IEEE Trans. Terahertz Sci. Technol.* **3,** 295–301 (2013).

24. Jeon, T. & Grischkowsky, D. Nature of Conduction in Doped Silicon. *Phys. Rev. Lett.* **78,** 1106–1109 (1997).

25. Jeon, T. & Grischkowsky, D. Observation of a Cole–Davidson type complex conductivity in the limit of very low carrier densities in doped silicon. *Appl. Phys. Lett.* **72,** 2259 (1998).

26. Jeon, T., Grischkowsky, D., Jeon, T., & Grischkowsky, D. Characterization of optically dense, doped semiconductors by reflection THz time domain spectroscopy. *Appl. Phys. Lett.* **72,** 3032 (1998).

27. Jeon, T., Mukherjee, D. G. K., & Menon, R. Electrical characterization of conducting polypyrrole by THz time-domain spectroscopy. *Appl. Phys. Lett.* **77,** 2452 (2000).

28. Kaindl, R. A., Carnahan, M. A., Orenstein, J., Chemla, D. S., Christen, H. M., Zhai, H., Paranthaman, M., & Lowndes, D. H. Far-Infrared Optical Conductivity Gap in Superconducting MgB 2 Films. **1,** 1–4 (2002).

29. Dexheimer, S. L. Terahertz Spectroscopy. *Taylor Fr. Gr.* (2008).

30. Ulbricht, R. & Heinz, T. F. Carrier dynamics in semiconductors studied with time-resolved terahertz spectroscopy. *Rev. Mod. Phys.* **83,** 543 (2011).

31. Schmuttenmaer, C. A. Exploring Dynamics in the Far-Infrared with Terahertz Spectroscopy. *Chem. Rev* **104,** 1759 (2004).

32. Němec, H., Kužel, P., & Sundström, V. Charge transport in nanostructured materials for solar energy conversion studied by time-resolved terahertz spectroscopy. *J. Photochem. Photobiol. A Chem.* **215,** 123–139 (2010).

33. Savenije, T. J., Kroeze, J. E., Wienk, M. M., Kroon, J. M., & Warman, J. M. Mobility and decay kinetics of charge carriers in photoexcited PCBM/PPV blends. *Phys. Rev. B* **69,** 155205–155216 (2004).

34. Italiano, I. Photoinduced Transient Stark Spectroscopy in Organic Semiconductors : A Method for Charge Mobility Determination in the Picosecond Regime. *Phys. Rev. Lett.* **96,** 106601 (2006).

35. Parkinson, P., Lloyd-hughes, J., Gao, Q., Tan, H. H., Jagadish, C., Johnston, M. B., & Herz, L. M. Transient Terahertz Conductivity of GaAs Nanowires. 15–18 (2007).

36. Tsokkou, D., Othonos, A., Zervos, M., Tsokkou, D., Othonos, A., & Zervos, M. Carrier dynamics and conductivity of SnO2 nanowires investigated by time-resolved terahertz spectroscopy. *Appl. Phys. Lett.* **100,** 133101 (2012).

37. Cooke, D. G., Macdonald, A. N., Hryciw, A., Wang, J., Li, Q., Meldrum, A., & Hegmann, F. A. Transient terahertz conductivity in photoexcited silicon nanocrystal films. *Phys. Rev. B* **73,** 193311 (2006).

38. Baxter, J. B. & Guglietta, G. W. Terahertz Spectroscopy. | *Anal. Chem* **83,** 4342–4368 (2011).

39. Němec, H., Kadlec, F., Kužel, P., Kadlec, F., & Kuz, P. Methodology of an optical pump-terahertz probe experiment : An analytical frequency- domain approach. *J. Chem. Phys.* **117,** 8454 (2002).

40. Koenig, S., Lopez-Diaz, D., Antes, J., Boes, F., Henneberger, R., Leuther, A., Tessmann, A., Schmogrow, R., Hillerkuss, D., & Palmer, R. Wireless sub-THz communi cation system with high data rate. *Nat. Photonics* **7,** 977–981 (2013).

41. Tonouchi, M. Cutting-edge terahertz technology. *Nat. Photonics* **1,** 97–105 (2007).

42. The Terahertz Wave eBook Fundamentals of Terahertz Wave. *Zomega terahertz Corp.* (2012).

43. Federici, J. F., Schulkin, B., Huang, F., Gary, D., Barat, R., Oliveira, F., & Zimdars, D. THz imaging and sensing for security applications—explosives, weapons and drugs. *Semicond. Sci. Technol.* **20,** S266–S280 (2005).

44. Panwar, A. K., Singh, A., Kumar, A., & Kim, H. Terahertz Imaging System for Biomedical Applications: Current Status. *Int. J. Eng. Technol. IJET-IJENS* **13,** 33–39 (2013).

45. Leahy-Hoppa, M. R., Fitch, M. J., & Osiander, R. Terahertz spectroscopy techniques for explosives detection. *Anal. Bioanal. Chem.* **395,** 247–257 (2009).

46. Markelz, A. G. Terahertz dielectric sensitivity to biomolecular structure and function. *IEEE J. Sel. Top. Quantum Electron.* **14,** 180–190 (2008).

47. Wietzke, S., Jansen, C., Krumbholz, N., Peters, O., Vieweg, N., Jördens, C., Scheller, M., Romeike, D., & Kunststoff-zentrum, S. Terahertz Spectroscopy A Powerful Tool for the Characterization of Plastic Materials. *2010 Int. Conf. Solid Dielectr.* 4–7 (2010).

48. Lane, P. A., Cunningham, P. D., Melinger, J. S., Esenturk, O., & Heilweil, E. J. Hot photocarrier dynamics in organic solar cells. *Nat. Commun.* **6,** 7558 (2015).

49. Esenturk, O., Melinger, J. S., & Heilweil, E. J. Terahertz mobility measurements on poly-3-hexylthiophene films: Device comparison, molecular weight, and film processing effects. *J. Appl. Phys.* **103,** 1–8 (2008).

50. Sorokin, E. Solid-State Materials for Few- Cycle Pulse Generation and Amplification. *Top. Appl. Phys.* **95,** 3–73 (2004).

51. Diels, J. C., Rudolph, W. Ultrashort Laser Pulse Phenomena. *Elseiver* (2006).

52. Jepsen, P. U., Møller, U., & Merbold, H. Investigation of aqueous alcohol and sugar solutions with reflection terahertz time-domain spectroscopy. *Opt. Express* **15,** 14717–14737 (2007).

53. Coutaz, J. & Duvillaret, L. Influence of noise on the characterization of materials by terahertz time-domain spectroscopy. *J. Opt. Soc. Am. B* **17,** 452–461 (2000).

54. Withayachumnankul, W. & Naftaly, M. Fundamentals of measurement in terahertz time-domain spectroscopy. *J. Infrared, Millimeter, Terahertz Waves* **35,** 610–637 (2014).

55. Naftaly, M. & Miles, R. E. Terahertz Time-Domain Spectroscopy for Material Characterization. *Proc. IEEE* **95,** 1658–1665 (2007).

56. Kuehn, W., Gaal, P., Reimann, K., Woerner, M., Elsaesser, T., & Hey, R. Terahertz-induced interband tunneling of electrons in GaAs. *Phys. Rev. B* **82,** 075204–075212 (2010).

57. Beard, M. C., Turner, G. M., & Schmuttenmaer, C. A. Transient photoconductivity in GaAs as measured by time-resolved terahertz spectroscopy. *Phys. Rev. B* **62,** 764–777 (2000).

58. Xin, X., Altan, H., Saint, A., Matten, D., Alfano, R. R., Xin, X., Altan, H., Saint, A., Matten, D., & Alfano, R. R. Terahertz absorption spectrum of para and ortho water vapors at different humidities at room temperature. *J. Appl. Phys.* **100,** 94905 (2006).

59. Theuer, M. Terahertz Time-Domain Spectroscopy Systems for Fundamental and Industrial Applications. *Cuvillier Verlag* (2009).

60. Geim, A.K., K. S. N. The rise of graphene. *Prog. Artic.* **6,** 183–191 (2007).

61. Docherty, C. J. & Johnston, M. B. Terahertz Properties of Graphene. *J Infrared Milli Terahz Waves* **33,** 797–815 (2012).

62. Novoselov, K. S., Geim, A. K., Morozov, S. V., Jiang, D., Zhang, Y., Dubonos, S. V., Grigorieva, I. V., & Firsov, A. A. Electric field effect in atomically thin carbon films. *Science (80-.).* **306,** 666–669 (2004).

63. Geim, A. K. Nobel Lecture : Random walk to graphene. **83,** 851–862 (2011).

64. Neto, A. H. C. The electronic properties of graphene. *Rev. Mod. Phys.* **81,** 109–162 (2009).

65. Evans, J. W., Thiel, P. A., & Bartelt, M. C. Morphological evolution during epitaxial thin film growth : Formation of 2D islands and 3D mounds. *Surf. Sci. Rep.* **61,** 1–128 (2006).

66. Abergel, D. S. L. & Russell, A. Visibility of graphene flakes on a dielectric substrate. *Appl. Phys. Lett.* **91,** 63125 (2007).

67. Wang, J., Deng, S., Liu, Z., & Liu, Z. The rare two-dimensional materials with Dirac cones. *Natl. Sci. Rev.* **2,** 22–39 (2015).

68. Katsnelson, M. I. Zitterbewegung, chirality, and minimal conductivity in graphene. *Eur. Phys. J. B* **51,** 157–160 (2006).

69. Zhang, Y. B., Tan, Y. W., Stormer, H. L., & Kim, P. Experimental observation of the quantum Hall effect and Berry's phase in graphene. *Nature* **438,** 201–204 (2005).

70. Novoselov, K. S., Jiang, Z., Zhang, Y., Morozov, S. V, Stormer, H. L., Zeitler, U., Maan, J. C., Boebinger, G. S., Kim, P., & Geim, A. K. Room-Temperature Quantum Hall Effect in Graphene. *Science (80-.).* **315,** 1379 (2007).

71. Han, S. J., Jenkins, K. A., Valdes Garcia, A., Franklin, A. D., Bol, A. A., & Haensch, W. High-frequency graphene voltage amplifier. *Nano Lett.* **11,** 3690–3693 (2011).

72. Li, Q., Tian, Z., Zhang, X., Singh, R., Du, L., Gu, J., Han, J., & Zhang, W. Active graphene-silicon hybrid diode for terahertz waves. *Nat. Commun.* **6,** 7082 (2015).

73. Schwierz, B. F. Graphene Transistors : Status , Prospects , and Problems. *IEEE* **101,** 1567–1584 (2013).

74. Dawlaty, J. M., Shivaraman, S., Chandrashekhar, M., Rana, F., & Spencer, M. G. Measurement of ultrafast carrier dynamics in epitaxial graphene. *Appl. Phys. Lett.* **92,** 42116 (2008).

75. Sensale-Rodriguez, B., Yan, R., Rafique, S., Zhu, M., Li, W., Liang, X., Gundlach, D., Protasenko, V., Kelly, M. M., Jena, D., Liu, L., & Xing, H. G. Extraordinary control of terahertz beam reflectance in graphene electro-absorption modulators. *Nano Lett.* **12,** 4518–4522 (2012).

76. Hecht, D. S., Hu, L., & Irvin, G. Emerging Transparent Electrodes Based on Thin Films of Carbon Nanotubes, Graphene, and Metallic Nanostructures. *Adv. Mater.* **23,** 1482–1513 (2011).

77. Yu, B. Graphene Nanoelectronics : Overview from Post-Silicon Perspective. *IEEE* 0–1 (2012).

78. Maeng, I., Lim, S., Chae, S. J., Lee, Y. H., Choi, H., & Son, J. H. Gate-controlled nonlinear conductivity of Dirac fermion in graphene field-effect transistors measured by terahertz time-domain spectroscopy. *Nano Lett.* **12,** 551–555 (2012).

79. Lee, S. H., Choi, M., Kim, T. T., Lee, S., Liu, M., Yin, X., Choi, H. K., Lee, S. S., Choi, C. G., Choi, S. Y., Zhang, X., & Min, B. Gate-controlled active graphene metamaterials at terahertz frequencies. *Nat. Mater.* **11,** 936–941 (2012).

80. Ren, L., Zhang, Q., Yao, J., Sun, Z., Kaneko, R., Yan, Z., Nanot, S., Jin, Z., Kawayama, I., Tonouchi, M., Tour, J. M., & Kono, J. Terahertz and infrared spectroscopy of gated large-area graphene. *Nano Lett.* **12,** 3711–3715 (2012).

81. Liang, G., Hu, X., Yu, X., Shen, Y., Li, L. H., Davies, A. G., Linfield, E. H., Liang, H. K., Zhang, Y., Yu, S. F., & Wang, Q. J. Integrated Terahertz Graphene Modulator with 100% Modulation Depth. *ACS Photonics* **2,** 1559–1566 (2015).

82. Kim, S. M., Hatami, F., Harris, J. S., Kurian, A. W., Ford, J., King, D., Scalari, G., Giovannini, M., Hoyler, N., Faist, J., & Harris, G. Biomedical terahertz imaging with a quantum cascade laser. *Appl. Phys. Lett.* **88,** 153903 (2006).

83. Wen, Q. Y., Zhang, H. W., Yang, Q. H., Xie, Y. S., Chen, K., & Liu, Y. L. Terahertz metamaterials with VO2 cut-wires for thermal tunability. *Appl. Phys. Lett.* **97,** 21111 (2010).

84. Wallace, V. P., Taday, P. F., Fitzgerald, A. J., Woodward, R. M., Cluff, J., Pye, R. J., & Arnone, D. D. Terahertz pulsed imaging and spectroscopy for biomedical and pharmaceutical applications. *Faraday Discuss.* **126,** 255-263-311 (2004).

85. Chen, H.-T., Padilla, W. J., Zide, J. M. O., Gossard, A. C., Taylor, A. J., & Averitt, R. D. Active terahertz metamaterial devices. *Nature* **444,** 597–600 (2006).

86. Kleine-Ostmann, T., Pierz, K., Hein, G., Dawson, P., Marso, M., & Koch, M. Spatially resolved measurements of depletion properties of large gate two-dimensional electron gas semiconductor terahertz modulators. *J. Appl. Phys.* **105,** 0–6 (2009).

87. Locatelli, A., Town, G. E., & De Angelis, C. Graphene-based terahertz waveguide modulators. *IEEE Trans. Terahertz Sci. Technol.* **5,** 351–357 (2015).

88. Sensale-Rodriguez, B., Fang, T., Yan, R., Kelly, M. M., Jena, D., Liu, L., & Xing, H. Unique prospects for graphene-based terahertz modulators. *Appl. Phys. Lett.* **99,** 2009–2012 (2011).

89. Sensale-Rodriguez, B., Yan, R., Rafique, S., Zhu, M., Li, W., Liang, X., Gundlach, D., Protasenko, V., Kelly, M. M., Jena, D., Liu, L., & Xing, H. G. Extraordinary control of terahertz beam reflectance in graphene electro-absorption modulators. *Nano Lett.* **12,** 4518–4522 (2012).

90. Sensale- Rodriguez, B., Yan, R., Kelly, M. M., Fang, T., Tahy, K., Hwang, W. S., Jena, D., Liu, L., & Xing, H. G. Broadband graphene terahertz modulators enabled by intraband transitions. *Nat. Commun.* **3,** 780 (2012).

91. Kakenov, N., Balci, O., Takan, T., Ozkan, V. A., Altan, H., & Kocabas, C. Observation of Gate-Tunable Coherent Perfect Absorption of Terahertz Radiation in Graphene. *ACS Photonics* **3,** 1531–1535 (2016).

92. Gao, W., Shu, J., Reichel, K., Nickel, D. V., He, X., Shi, G., Vajtai, R., Ajayan, P. M., Kono, J., Mittleman, D. M., & Xu, Q. High-contrast terahertz wave modulation by gated graphene enhanced by extraordinary transmission through ring apertures. *Nano Lett.* **14,** 1242–1248 (2014).

93. Shen, N. H., Tassin, P., Koschny, T., & Soukoulis, C. M. Comparison of gold- and graphene-based resonant nanostructures for terahertz metamaterials and an ultrathin graphene-based modulator. *Phys. Rev. B - Condens. Matter Mater. Phys.* **90,** 1–8 (2014).

94. Gao, W., Shu, J., Reichel, K., Nickel, D. V., He, X., Shi, G., Vajtai, R., Ajayan, P. M., Kono, J., Mittleman, D. M., & Xu, Q. High-contrast terahertz wave modulation by gated graphene enhanced by extraordinary transmission through ring apertures. *Nano Lett.* **14,** 1242–1248 (2014).

95. Shi, F., Chen, Y., Han, P., & Tassin, P. Broadband, Spectrally Flat, Graphene-based Terahertz Modulators. *Small* **11,** 6044–6050 (2015).

96. Wu, Y., La-O-Vorakiat, C., Qiu, X., Liu, J., Deorani, P., Banerjee, K., Son, J., Chen, Y., Chia, E. E. M., & Yang, H. Graphene Terahertz Modulators by Ionic Liquid Gating. *Adv. Mater.* **27,** 1874–1879 (2015).

97. Baek, I. H., Ahn, K. J., Kang, B. J., Bae, S., Hong, B. H., Yeom, D. I., Lee, K., Jeong, Y. U., & Rotermund, F. Terahertz transmission and sheet conductivity of randomly stacked multi-layer graphene. *Appl. Phys. Lett.* **102,** 191109 (2013).

98. Kakenov, N., Takan, T., Ozkan, V. A., Balcı, O., Polat, E. O., Altan, H., & Kocabas, C. Graphene-enabled electrically controlled terahertz spatial light modulators. *Opt. Lett.* **40,** 1984 (2015).

99. Wu, Y., Ruan, X., Chen, C.-H., Shin, Y. J., Lee, Y., Niu, J., Liu, J., Chen, Y., Yang, K.-L., Zhang, X., Ahn, J.-H., & Yang, H. Graphene/liquid crystal based terahertz phase shifters. *Opt. Express* **21,** 21395–402 (2013).

100. Unlu, M., Hashemi, M. R., Berry, C. W., Li, S., Yang, S.-H., & Jarrahi, M. Switchable scattering meta-surfaces for broadband terahertz modulation. *Sci. Rep.* **4,** 5708 (2014).

101. Kim, J. Y., Lee, C., Bae, S., Kim, K. S., Hong, B. H., & Choi, E. J. Far-infrared study of substrate-effect on large scale graphene. *Appl. Phys. Lett.* **98,** 201907 (2011).

102. Kakenov, N., Balci, O., Polat, E. O., Altan, H., & Kocabas, C. Broadband terahertz modulators using self-gated graphene capacitors. *J. Opt. Soc. Am. B* **32,** 1861–1866 (2015).

103. Liu, J., Li, P., Chen, Y., Song, X., Qi, M., Yang, W., Fei, Q., Zheng, B., Jiarui, H., Yang, H., Wen, Q., & Zhang, W. Flexible terahertz modulator based on coplanar- gate graphene field-effect transistor structure. *Opt. Lett.* **41,** 816–819 (2016).

104. Van Der Valk, N. C. J. & Planken, P. C. M. Electro-optic detection of subwavelength terahertz spot sizes in the near field of a metal tip. *Appl. Phys. Lett.* **81,** 1558–1560 (2002).

105. Li, X., Cai, W., Colombo, L., & Ruoff, R. S. Evolution of Graphene Growth on Ni and Cu by Carbon Isotope Labeling. *Nano Lett.* **9,** 4268–4272 (2009).

106. Polat, E. O., Balcı, O., & Kocabas, C. Graphene based flexible electrochromic devices. *Sci. Rep.* **4,** 6484 (2014).

107. Polat, E. O., Uzlu, H. B., Balci, O., Kakenov, N., Kovalska, E., & Kocabas, C. Graphene-Enabled Optoelectronics on Paper. *ACS Photonics* **3,** 964–971 (2016).

108. Frenzel, A. J., Lui, C. H., Fang, W., Nair, N. L., Herring, P. K., Jarillo-Herrero, P., Kong, J., & Gedik, N. Observation of suppressed terahertz absorption in photoexcited graphene. *Appl. Phys. Lett.* **102,** 113111 (2013).

109. Qi, M., Zhou, Y., Hu, F., Xu, X., Li, W., Li, A., Bai, J., & Ren, Z. Improving Terahertz Sheet Conductivity of Graphene Films Synthesized by Atmospheric Pressure Chemical Vapor Deposition with Acetylene. *J. Phys. Chem. C* **118,** 15054–15060 (2014).

110. Zhou, Y., Xu, X., Hu, F., Zheng, X., Li, W., Zhao, P., Bai, J., & Ren, Z. Graphene as broadband terahertz antireflection coating. *Appl. Phys. Lett.* **104,** 51106 (2014).

111. Sensale-Rodriguez, B., Fang, T., Yan, R., Kelly, M. M., Jena, D., Liu, L., & Xing, H. Unique prospects for graphene-based terahertz modulators. *Appl. Phys. Lett.* **99,** 2009–2012 (2011).

112. Dadrasnia, E., Lamela, H., Kuppam, M. B., Garet, F., & Coutaz, J.-L. Determination of the DC Electrical Conductivity of Multiwalled Carbon Nanotube Films and Graphene Layers from Noncontact Time-Domain Terahertz Measurements. *Adv. Condens. Matter Phys.* **2014,** 1–6 (2014).

113. Buron, J. D., Petersen, D. H., Bøggild, P., Cooke, D. G., Hilke, M., Sun, J., Whiteway, E., Nielsen, P. F., Hansen, O., Yurgens, A., & Jepsen, P. U. Graphene Conductance Uniformity Mapping. *Nano Lett.* **12,** 5074–5081 (2012).

114. Orlita, M., Faugeras, C., Plochocka, P., Neugebauer, P., Martinez, G., Maude, D. K., Barra, A.-L., Sprinkle, M., Berger, C., de Heer, W. A., & Potemski, M. Approaching the Dirac Point in High-Mobility Multilayer Epitaxial Graphene. *Phys. Rev. Lett.* **101,** 267601 (2008).

115. Nagel, M., Safiei, A., Sawallich, S., Matheisen, C., Pletzer, T. M., Mewe, A. A., van der Borg, N., Cesar, I., & Kurz, H. THz microprobe system for contact-free high-resolution sheet resistance imaging. *Proc. 28th Eur. Photovolt. Sol. Energy Conf. Exhib.* 856–860 (2013).

116. Wu, Y., Ruan, X., Chen, C.-H., Shin, Y. J., Lee, Y., Niu, J., Liu, J., Chen, Y., Yang, K.-L., Zhang, X., Ahn, J.-H., & Yang, H. Graphene/liquid crystal based terahertz phase shifters. *Opt. Express* **21,** 21395–402 (2013).

117. Chatzakis, I., Li, Z., Benderskii, A. V, & Cronin, S. B. Broadband terahertz modulation in electrostatically-doped artificial trilayer graphene. *Nanoscale* **9,** 1721 (2017).

118. Bae, S., Kim, H., Lee, Y., Xu, X., Park, J.-S., Zheng, Y., Balakrishnan, J., Lei, T., Ri Kim, H., Song, Y. Il, Kim, Y.-J., Kim, K. S., Özyilmaz, B., Ahn, J.-H., Hong, B. H., & Iijima, S. Roll-to-roll production of 30-inch graphene films for transparent electrodes. *Nat. Nanotechnol.* **5,** 574–578 (2010).

119. McEuen, P. L. & Park, J. Y. Electron Transport in Single-Walled Carbon Nanotubes. *Mrs Bull.* 272 (2004).

120. Horng, J., Chen, C. F., Geng, B., Girit, C., Zhang, Y., Hao, Z., Bechtel, H. A., Martin, M., Zettl, A., Crommie, M. F., Shen, Y. R., & Wang, F. Drude conductivity of Dirac fermions in graphene. *Phys. Rev. B - Condens. Matter Mater. Phys.* **83,** 1–5 (2011).

121. Smith, N. V. Classical generalization of the Drude formula for the optical conductivity. *Phys. Rev. B* **64,** 155106 (2001).

122. Kuzel, P. & Nemec, H. Terahertz conductivity in nanoscaled systems : effective medium theory aspects. *J. Phys. D. Appl. Phys.* **47,** 374005 (2014).

123. Li, G., Li, D., Jin, Z., & Ma, G. Photocarriers dynamics in silicon wafer studied with optical-pump terahertz-probe spectroscopy. *Opt. Commun.* **285,** 4102–4106 (2012).

124. Lloyd-Hughes, J. & Jeon, T.-I. A review of the terahertz conductivity of bulk and nano-materials. *J. Infrared, Millimetre Terahertz Waves* **33,** 871–925 (2012).

125. Ai, X., Beard, M. C., Knutsen, K. P., Shaheen, S. E., Rumbles, G., & Ellingson, R. J. Photoinduced Charge Carrier Generation in a Poly (3-hexylthiophene) and Methanofullerene Bulk Heterojunction Investigated by Time-Resolved Terahertz Spectroscopy. *J. Phys. Chem. B* **110,** 25462–25471 (2006).

126. Jnawali, G., Rao, Y., Yan, H., & Heinz, T. F. Observation of a transient decrease in terahertz conductivity of single-layer graphene induced by ultrafast optical excitation. *Nano Lett.* **13,** 524–530 (2013).

127. Liu, W., Valdés Aguilar, R., Hao, Y., Ruoff, R. S., & Armitage, N. P. Broadband microwave and time-domain terahertz spectroscopy of chemical vapor deposition grown graphene. *J. Appl. Phys.* **110,** 83510 (2011).

128. Strait, J. H., Wang, H., Shivaraman, S., Shields, V., Spencer, M., & Rana, F. Very Slow Cooling Dynamics of Photoexcited Carriers in Graphene Observed by Optical-Pump Terahertz-Probe Spectroscopy. *Nano Lett.* **11,** 4902–4906 (2011).

129. Lee, C., Kim, J. Y., Bae, S., Kim, K. S., Hong, B. H., & Choi, E. J. Optical response of large scale single layer graphene. *Appl. Phys. Lett.* **98,** 2009–2012 (2011).

130. Buron, J. D., Pizzocchero, F., Jessen, B. S., Booth, T. J., Nielsen, P. F., Hansen, O., Hilke, M., Whiteway, E., Jepsen, P. U., Boggild, P., & Petersen, D. H. Electrically continuous graphene from single crystal copper verified by terahertz conductance spectroscopy and micro four-point probe. *Nano Lett.* **14,** 6348–6355 (2014).

131. Zou, X., Shang, J., Leaw, J., Luo, Z., Luo, L., La-o-vorakiat, C., Cheng, L., Cheong, S. A., Su, H., Zhu, J.-X., Liu, Y., Loh, K. P., Castro Neto, A. H., Yu, T., & Chia, E. E. M. Terahertz Conductivity of Twisted Bilayer Graphene. *Phys. Rev. Lett.* **110,** 67401 (2013).

132. Chen, J. H., Jang, C., Xiao, S., Ishigami, M., & Fuhrer, M. S. Intrinsic and extrinsic performance limits of graphene devices on SiO2. *Nat. Nanotechnol.* **3,** 206–209 (2008).

133. Núñez, C. G., Navaraj, W. T., Polat, E. O., & Dahiya, R. Energy-Autonomous, Flexible, and Transparent Tactile Skin. *Adv. Funct. Mater.* **27,** 1606287 (2017).

134. Dean, C. R., Young, a F., Meric, I., Lee, C., Wang, L., Sorgenfrei, S., Watanabe, K., Taniguchi, T., Kim, P., Shepard, K. L., & Hone, J. Boron nitride substrates for high-quality graphene electronics. *Nat. Nanotechnol.* **5,** 722–726 (2010).

135. Dani, K. M., Lee, J., Sharma, R., Mohite, A. D., Galande, C. M., Ajayan, P. M., Dattelbaum, A. M., Htoon, H., Taylor, A. J., & Prasankumar, R. P. Intraband conductivity response in graphene observed using ultrafast infrared-pump visible-probe spectroscopy. *Phys. Rev. B - Condens. Matter Mater. Phys.* **86,** 1–7 (2012).

136. Newson, R. W., Dean, J., Schmidt, B., & van Driel, H. M. Ultrafast carrier kinetics in exfoliated graphene and thin graphite films. *Opt. Express* **17,** 2326–2333 (2009).

137. George, P. a, Strait, J., Dawlaty, J., Shivaraman, S., Chandrashekhar, M., Rana, F., & Spencer, M. G. Ultrafast Optical-Pump Terahertz-Probe Spectroscopy of the Carrier Relaxation and Recombination Dynamics in Epitaxial Graphene. *Nano Lett.* **8,** 4248–4251 (2008).

138. Paul, M. J., Lee, B., Wardini, J. L., Thompson, Z. J., Stickel, A. D., Mousavian, A., Choi, H., Minot, E. D., & Lee, Y.-S. Terahertz induced transparency in single-layer graphene. *Appl. Phys. Lett.* **105,** 221107–5 (2014).

139. Choi, H., Borondics, F., Siegel, D. A., Zhou, S. Y., Martin, M. C., Lanzara, A., & Kaindl, R. A. Broadband electromagnetic response and ultrafast dynamics of few-layer epitaxial graphene. *Appl. Phys. Lett.* **94,** 172102 (2009).

140. Tielrooij, K. J., Song, J. C. W., Jensen, S. A., Centeno, A., Pesquera, A., Elorza, A. Z., Bonn, M., Levitov, L. S., & Koppens, F. H. L. Photoexcitation cascade and multiple hot-carrier generation in graphene. *Nat. Phys.* **9,** 248–252 (2013).

141. Kar, S., Mohapatra, D. R., Freysz, E., & Sood, A. K. Tuning photoinduced terahertz conductivity in monolayer graphene: Optical-pump terahertz-probe spectroscopy. *Phys. Rev. B - Condens. Matter Mater. Phys.* **90,** 165420 (2014).

142. Winnerl, S., Orlita, M., Plochocka, P., Kossacki, P., Potemski, M., Winzer, T., Malic, E., Knorr, A., Sprinkle, M., Berger, C., de Heer, W. A., Schneider, H., & Helm, M. Carrier Relaxation in Epitaxial Graphene Photoexcited Near the Dirac Point. *Phys. Rev. Lett.* **107,** 237401 (2011).

143. Johannsen, J. C., Ulstrup, S., Cilento, F., Crepaldi, A., Zacchigna, M., Cacho, C., Turcu, I. C. E., Springate, E., Fromm, F., Raidel, C., Seyller, T., Parmigiani, F., Grioni, M., & Hofmann, P. Direct view of hot carrier dynamics in graphene. *Phys. Rev. Lett.* **111,** 1–5 (2013).

144. Song, J. C. W. & Levitov, L. S. Energy flows in graphene: hot carrier dynamics and cooling. *J. Phys. Condens. Matter* **27,** 164201 (2015).

145. Tse, W. K. & Das Sarma, S. Energy relaxation of hot Dirac fermions in graphene. *Phys. Rev. B - Condens. Matter Mater. Phys.* **79,** 2–6 (2009).

146. Song, J. C. W., Reizer, M. Y., & Levitov, L. S. Disorder-assisted electron-phonon scattering and cooling pathways in graphene. *Phys. Rev. Lett.* **109,** 1–5 (2012).

147. Mihnev, M. T., Kadi, F., Divin, C. J., Winzer, T., Lee, S., Liu, C.-H., Zhong, Z., Berger, C., de Heer, W. A., Malic, E., Knorr, A., & Norris, T. B. Microscopic origins of the terahertz carrier relaxation and cooling dynamics in graphene. *Nat. Commun.* **7,** 11617 (2016).

148. Prechtel, L., Song, L., Schuh, D., Ajayan, P., Wegscheider, W., & Holleitner, A. W. Time-resolved ultrafast photocurrents and terahertz generation in freely suspended graphene. *Nat. Commun.* **3,** 646 (2012).

149. Mueller, T., Xia, F., & Avouris, P. Graphene photodetectors for high-speed optical communications. *Nat. Photonics* **4,** 297–301 (2010).

150. Otsuji, T., Boubanga-Tombet, S., Satou, A., Suemitsu, M., & Ryzhii, V. Spectroscopic Study on Ultrafast Carrier Dynamics and Terahertz Amplified Stimulated Emission in Optically Pumped Graphene. *J. Infrared, Millimeter, Terahertz Waves* **33,** 825–838 (2012).

151. Boubanga-Tombet, S., Chan, S., Watanabe, T., Satou, A., Ryzhii, V., & Otsuji, T. Ultrafast carrier dynamics and terahertz emission in optically pumped graphene at room temperature. *Phys. Rev. B - Condens. Matter Mater. Phys.* **85,** 3–8 (2012).

152. Docherty, C. J., Lin, C.-T., Joyce, H. J., Nicholas, R. J., Herz, L. M., Li, L.-J., & Johnston, M. B. Extreme sensitivity of graphene photoconductivity to environmental gases. *Nat. Commun.* **3,** 1228 (2012).

153. Gierz, I., Petersen, J. C., Mitrano, M., Cacho, C., Turcu, I. C. E., Springate, E., Stöhr, A., Köhler, A., Starke, U., & Cavalleri, A. Snapshots of non-equilibrium Dirac carrier distributions in graphene. *Nat. Mater*. **12,** 1119–24 (2013).

154. Fu, M., Wang, X., Ye, J., Feng, S., Sun, W., Han, P., & Zhang, Y. Strong negative terahertz photoconductivity in photoexcited graphene. *Opt. Commun.* 1–0 (2017). doi:10.1016/j.optcom.2017.01.045

155. Sprinkle, M., Siegel, D., Hu, Y., Hicks, J., Tejeda, A., Taleb-Ibrahimi, A., Le Fevre, P., Bertran, F., Vizzini, S., Enriquez, H., Chiang, S., Soukiassian, P., Berger, C., De Heer, W. A., Lanzara, A., & Conrad, E. H. First direct observation of a nearly ideal graphene band structure. *Phys. Rev. Lett.* **103,** 226803 (2009).

156. Mihnev, M. T., Tolsma. J. R., Divin, C. J., Sun, D., Asgari, R., Polini, M. Electronic cooling via interlayer Coulomb coupling in multilayer epitaxial graphene. *Nat. Commun.* **6,** 8105 (2015).

157. Gusynin, V. P., Sharapov, S. G., Carbotte, J. P. On the universal ac optical background in graphene. *New J. Phys.* **11,** 95013 (2009).

158. Brida, D., Tomadin, A., Manzoni, C., Kim, Y. J., Lombardo, A., Milana, S., Nair, R. R., Novoselov, K. S., Ferrari, A. C., Cerullo, G., & Polini, M. Ultrafast collinear scattering and carrier multiplication in graphene. *Nat. Commun.* **4,** 1–9 (2013).

159. Wu, S., Liu, W. T., Liang, X., Schuck, P. J., Wang, F., Shen, Y. R., & Salmeron, M. Hot phonon dynamics in graphene. *Nano Lett.* **12,** 5495–5499 (2012).

160. Justin, C. W., Tielrooij, K. J., Koppens, F. H. L., & Levitov, L. S. Photoexcited carrier dynamics and impact-excitation cascade in graphene. *Phys. Rev. B* **87,** 155429–6 (2013).

VITA

CONTACT INFORMATION

Name: Emine Kaya

Email: eminekaya@gmail.com

PERSONAL INFORMATION

Date of Birth: 25.01.1986

Place of Birth: Artvin

Citizenship: TC

EMPLOYMENT HISTORY

Research Assistant: 2009-2017

Summer Internship: Türkiye Petrolleri Anonim Ortaklığı 2008 July

EDUCATION

High School

1999-2003 Fahrettin Kerim Gökay Anatolian High School

GPA: 5.00/5.00

Under graduate

2003-2009 METU/ Chemistry Education Department

GPA: 3.42/4.00

Graduate

2009-2011 METU/ Chemistry Department

GPA: 3.64/4.00

Ms Thesis: Solution Processable Benzotriazole and Fluorene Containing Copolymers for Photovoltaic Applications

Doctoral Studies

2011- 2017 METU/ Chemistry Department

GPA: 3.50/4.00

PhD Thesis: Construction of Terahertz Spectrometers and Their Use in Characterization of Conductivities and Modulation Behaviors of Graphene Layers

PROFESSIONAL QUALIFICATIONS

Computer Skills: MS Office, Origin Lab

Language: English (Advanced), German (Beginner)

CONFERENCES

1) Terahertz Spektroskopi Sistemleri ile Tek ve Çok Tabakalı Grafen Örneklerinin iletkenlik Ölçümleri ve Yük Dinamiğinin Araştırılması, E. Kaya, N. Kakenov, C. Kocabaş, H. Altan, O. Esentürk, 29. Ulusal Kimya Kongresi, ODTÜ, Ankara, Türkiye. (Poster)

2) Broadband Terahertz Modulators Based on Multilayer Graphene on PVC, E. Kaya, N. Kakenov, C. Kocabaş, H. Altan, O. Esentürk, Fotonik 2016, Bilkent University, Ankara, Turkey. (Poster)

3) Time Resolved Terahertz Spectroscopy for Investigation of Charge Carrier Dynamics in Semiconductors, E. Kaya, E. Arık**,** Z. Özer, B. Ortaç, H. Altan, O. Esentürk, International Workshop on Terahertz Technology and Applications 2014, Kaiserslautern, Germany. (Poster)

4) Building a Time Resolved Terahertz Spectroscopy for Investigation of Charge Carrier Dynamics in Semiconductors, E. Kaya, E. Arık, Z. Özer, B. Aslan, B. Ortaç, H. Altan, O. Esentürk, Semiconductor Science and Technology Conference 2014, Istanbul, Turkey (Oral Presentation)

5) Visible Pump-Far-Infrared (FIR) Probe Measurements of Epitaxially Grown undoped GaAs, H. Altan, D. Akbar, E. Kaya, O. Esentürk, S. Winnerl, TAC LSUM 2013 (Turkish Accelerator Center Light Sources User Meeting), Ankara University, Ankara, Turkey.

6) Time Resolved Terahertz Spectroscopy for the Investigation of Charge Carrier Dynamics in Organic Solar Cell Thin Films, E. Kaya, Okan Esentürk, Nano Tr 2012, Ankara, Turkey. (Poster)

7) E. Kaya, A. Balan, D. Baran, L. Toppare, A. Cirpan "Electrochemical And Optical Studies Of Solution Processable Benzotriazole And Fluorene Containing Copolymers" 9th International Electrochemistry Meeting, Cesme-Izmir, Turkey, 25-29 September 2011. (Poster)

8) E. Kaya, A. Balan, D. Baran, L. Toppare, A. Cirpan "Solution Processable Benzotriazole and Fluorene Containing Copolymers for Organic Photovoltaic Applications" 26th European Photovoltaic Solar Energy Conference and Exhibition, Hamburg, Germany, 5 - 9 September 2011. (Poster)

PUBLICATIONS

1) Electrochromic and optical studies of solution processable benzotriazole and fluorene containing copolymers, E. Kaya, A. Balan, D. Baran, A. Cirpan, L. Toppare, Organic Electronics 12 (2011) 202–209.

2) Solution processable benzotriazole and fluorene containing copolymers for photovoltaic applications, E. Kaya, D. H. Apaydın,, D. E. Yıldız, L. Toppare, A. Cirpan, Solar Energy Materials & Solar Cells 99 (2012) 321–326.

3) The main electrical and interfacial properties of benzotriazole and fluorene based organic devices, D.E. Yildiz, D.H. Apaydin, E. Kaya, A. Cirpan, Journal of Macromolecular Science, Part A: Pure and Applied Chemistry, 253, (2013) 45-51.

4) Broadband THz Modulators Based on Multilayer Graphene, E. Kaya, N. Kakenov, C. Kocabaş, H. Altan, O. Esenturk, Manuscript in preparation.